Flame Stabilization and Unsteady Dynamics in Complex Hydrogen-Fueled Combustion Systems: Role of Finite-Rate Chemistry

by

Shuzhi Zhang

A dissertation submitted in partial fulfillment
of the requirements for the degree of
Doctor of Philosophy
(Aerospace Engineering)
in The University of Michigan
2026

Doctoral Committee:

Professor Venkat Raman, Chair
Professor Andre Boehman
Professor Mirko Gamba
Professor Margaret Wooldridge

Shuzhi Zhang
szzhang@umich.edu
ORCID iD: 0009-0004-9165-695X

© Shuzhi Zhang 2026

To my parents and my dear friend River

ACKNOWLEDGEMENTS

I would like to express my deepest gratitude to my advisor, Professor Venkat Raman, for his guidance, support, and patience throughout my Ph.D. I am especially grateful for the freedom he gave me, both intellectually and personally, to explore difficult questions while always providing the perspective needed to move forward. I feel very fortunate to have completed this work under his mentorship.

I would also like to sincerely thank my dissertation committee members, Professor Margaret Wooldridge, Professor Andre Boehman, and Professor Mirko Gamba, for their time, thoughtful feedback, and encouragement. Their questions and suggestions helped strengthen this dissertation and broadened the way I think about combustion science and engineering. I am grateful for their willingness to engage with my work and for the support they have shown throughout this process.

I am thankful to my colleagues and collaborators during my Ph.D. for making graduate school both intellectually rewarding and personally enjoyable. I have benefited greatly from technical discussions, shared frustrations, and the everyday support of the people around me. I am especially grateful to the members of our research group and to the friends and lab mates who made the long days of simulations, debugging, writing, and revising much more manageable. The sense of friendship I found during my Ph.D. made a meaningful difference in this journey.

I want to thank my parents for their unconditional love, sacrifice, and belief in me. Their support has been the foundation for everything I have been able to do. I am also deeply grateful to my friends for their encouragement, understanding, and companionship throughout this process. They reminded me to keep perspective, helped me through difficult moments, and celebrated the milestones along the way. This dissertation would not have been possible without the support of all of these people.

I would especially like to thank my beloved River, who was far more than a pet. He was my companion, my comfort, and a source of unwavering emotional support throughout my Ph.D. journey. During the most difficult times, his presence brought a kind of peace that words cannot fully capture. Although he is no longer here, his memory remains deeply woven into this journey. I believe he stayed with me until his mission was complete, and I will forever be thankful for the love and strength he gave me.

TABLE OF CONTENTS

DEDICATION ii

ACKNOWLEDGEMENTS iii

LIST OF FIGURES vi

LIST OF TABLES xi

LIST OF APPENDICES xii

LIST OF ACRONYMS xiii

ABSTRACT xiv

CHAPTER

1 Gas Turbine Engines and Coupled Flame Characteristics 1

1.1 Future of Gas Turbines 1
1.2 Axial Fuel Staging in Gas Turbines 5
1.3 Flame Stabilization in Reactive Flows 9
1.4 Transition to Combustion Instability 10
1.5 Unsteady Flame Dynamics in Hydrogen Combustors 12
1.6 Role of Chemistry and Kinetic Uncertainty in Hydrogen Combustion and Simulation 13
1.7 Chapter Summary 14
1.8 Scope of the Dissertation 15

2 Numerical Methods for High-Subsonic Hydrogen Combustion 18

2.1 Conservation equations 20
2.2 Complex Geometry and Embedded boundaries 24
2.3 Characteristic boundary conditions for reacting flows 26
2.4 GPU-Oriented Implementation 34

3 Fluid-Chemistry Interactions and Modeling Challenges in Hydrogen Jets in Crossflow 37

3.1 Introduction 37
3.2 Configuration and Modeling Approach 40
3.3 Results and Discussion 48

3.3.1 Flame Morphology . . . 49
3.3.2 Cross-stream Flow Field . . . 51
3.3.3 Flame Branch Analysis . . . 52
3.3.4 Flame Edge Characteristics . . . 53
3.3.5 Hydrogen enrichment . . . 57
3.3.6 Implications for stability-map construction . . . 59
3.4 Summary and Conclusions . . . 59

4 Flame Stabilization and Characteristics in a Multi-Tube Micromixer . . . 62

4.1 Introduction . . . 62
4.2 Experimental Configurations and Simulation Setup . . . 63
4.3 Results . . . 65
4.3.1 Flame structure validation . . . 65
4.3.2 Global flame dynamics . . . 67
4.3.3 Local flame dynamics . . . 71
4.3.4 Flow field dynamics . . . 74
4.4 Summary . . . 76

5 Kinetic Uncertainty in Complex Reacting Systems . . . 79

5.1 Introduction . . . 79
5.2 State-reconstruction UQ method . . . 82
5.3 Covariance-transfer UQ method . . . 84
5.4 State-reconstruction UQ for Multi-tube Combustor . . . 88
5.4.1 Trajectories with FFCM-2 for H_2 fuel . . . 89
5.4.2 Local Chemical Timescales and Reaction Pathways . . . 90
5.5 Flame Stabilization and Dynamics for Hydrogen Enriched Jet Flames . . . 94
5.5.1 Global Flame Structure . . . 95
5.5.2 Strained Flame Front . . . 95
5.5.3 Flame Edge Analysis . . . 97
5.6 Covariance-transfer UQ for Hydrogen Jet Flames . . . 99
5.6.1 Eulerian Chemical State Dynamics . . . 99
5.6.2 Lagrangian Particles . . . 100
5.6.3 Lagrangian Chemical State Dynamics . . . 102
5.7 Summary . . . 106

6 Summary, Conclusions, and Future Directions . . . 108

6.1 Summary . . . 108
6.2 Scientific conclusions . . . 110
6.3 Future directions . . . 114

APPENDICES . . . 116

BIBLIOGRAPHY . . . 125

LIST OF FIGURES

FIGURE

1.1 Illustration of the mismatch between electricity generation and demand in renewable-rich power systems. The left panel shows the California net-load "duck curve," including midday overgeneration risk and steep evening ramping demand, adapted from CAISO materials [1]. The right panel shows a daily California generation profile highlighting periods of excess renewable generation and later dispatch requirements, adapted from IEA analysis graphics [2]. 2

1.2 Projected growth in AI-related electricity demand, illustrating the increasing power requirements associated with large-scale training and inference infrastructure. Adapted from Wells Fargo analysis [3] of AI-driven electricity demand. . . 3

1.3 Conceptual pathway linking renewable electricity, hydrogen production, compression, storage, and subsequent gas-turbine power generation through hydrogen or hydrogen/natural-gas blended fueling. Adapted from Siemens Energy and HYFLEXPOWER project materials [4; 5]. 4

1.4 Representative axial fuel staging (Axial Fuel Staging (AFS)) combustor architecture integrating a multi-tube mixer, a premixing head-end assembly, and downstream axial-fuel injectors. The configuration illustrates how upstream premixing and downstream staging can be combined to distribute heat release across multiple combustor zones. Adapted from advanced gas-turbine combustor development materials in Hughes et al. [6] and National Energy Technology Laboratory and GE Power [7]. 5

2.1 Example of block-structured adaptive mesh refinement used to concentrate resolution near localized reacting-flow structures in an AMReX-based solver [8]. . . 20

2.2 Computational domain showing the waves entering and leaving through inlet and outlet. 31

2.3 Illustration of GPU-oriented execution strategies for AMReX-based reacting-flow solvers, highlighting how mesh, physics, and chemistry kernels are organized for accelerator performance [9]. 34

2.4 Roofline analysis comparing baseline and optimized convection and chemistry kernels, showing improved performance and hardware utilization in the GPU-oriented solver implementation [9]. 35

3.1 Computational domain with major dimensions and injector-region mesh view. The hydrogen jet issues normally from a 2 mm injector into a hot crossflow, while mesh refinement is concentrated near the flame front and other localized reacting structures. 41

3.2 Source terms plotted in progress variable–mixture fraction space for FPVA, unstrained-FGM, and strained-FGM (S-FGM) tabulations from left to right, adapted from Sharma et al. [10]. 43
3.3 3-D view of the S-FGM tabulation with vertical slices of reaction source visualized at different Z levels. 44
3.4 Mass fraction evolution showing diffusion of different species into a pure OH region. 45
3.5 Instantaneous snapshot of U_x iso-lines for three outflow treatments: zero-gradient extrapolation (left), NSCBC without transverse terms (middle), and NSCBC with transverse terms (right). 47
3.6 Contour of O_2 mass fraction for Case B. 48
3.7 Temporal evolution of (a) temperature at the injector inlet, (b) temperature at the channel inlet, and (c) pressure at the channel outlet. 49
3.8 Contour plots (at the z centered planes) of temporally averaged velocity of DNS overlaid with Y_{OH} iso-lines from both DNS and LES compared to experimental findings (black dots). 49
3.9 standard deviation of flow velocity (superimposed with streamlines and quivers) profiles along the flow direction from both LES and Direct Numerical Simulation (DNS) for case C. Planes taken at $x/d = 2.25$ and 4.00 downstream of the injector. 52
3.10 Flame Branch configurations (at the z centered planes) of Case C at different time instances. Top row: LES results. Bottom row: DNS results. Background is velocity magnitude contour overlaid with Y_{OH} iso-lines(black solid lines) representing the flame front dynamic. The inset images show the zoomed-in view of the key features for each time instance. 53
3.11 Plots for temporal average data (at the z centered planes) from DNS and LES at different points on the flame front. Points A, B and C are assumed close to the edge of the flame and corresponding Y_{OH} vs. Z data is presented with low strain and high strain solutions. 54
3.12 Point trajectories in Flamelet phase space for Case C. Path 1 and 2 are from DNS. 56
3.13 DNS mixture fraction data fit with β distribution at Point A. 57
3.14 Scatter plot of temperature versus mixture fraction at flame front location of different cases 58

4.1 Plot shows the computational domain with major dimensions. Front view presents the mid-section Y and Z planes. The inset at the injection plane highlights the jets and the approximate fuel trajectory, while the second inset depicts the various AMR levels surrounding the flame front. All dimensions are in millimeters (mm). 64
4.2 Time-averaged Y_{OH} for both Cases. Top row shows the mid-section Y planes for the combustion chamber, while bottom row presents one-to-one comparison for the topmost tube element flame structures. 66

4.3 Time-averaged heat release rate (HRR) and standard deviation of Y_{OH} fields illustrating the global flame structure for Case B; The left three columns show HRR on the mid-section Y plane, mid-section Z plane and transverse plane at X = 5 mm downstream of the tube exit, respectively; The rightmost column displays the standard deviation of Y_{OH} on the transverse plane at X = 15 mm downstream of the tube exit; White solid line on mid-section planes are the isoline of OH mass fraction $Y_{OH} = 0.00125$ as 30% of the maximum value; Green and black solid lines on transverse planes are the isoline of mixture fraction $Z_{Bilger} = 0.0811$ corresponding to $\phi = 0.53$. 67
4.4 Visual definition of R_W and R_L on the top row; Reaction zone length and thickness for mid-section Y and Z planes on middle and bottom row respectively; Element number are shown for each plane separately in Fig. 4.3. 68
4.5 The local equivalence ratio profiles along the white dashed line indicated in Fig.4.3, located at X=15 mm downstream of the jet exits. 70
4.6 Time series images of HRR and fuel concentration representing reaction pocket and fuel filament advancement in Case B. The top row images show instantaneous HRR, while bottom row images depict fuel concentration rescaled to highlight reaction pocket and fuel filament. 72
4.7 KDE plots for joint PDFs of $\dot{\varepsilon}$ and $\log_{10}(HRR)$ at location A measured along outer tube at Y-axis (marked 1 in Fig 4.3), B measured along outer tube at Z-axis and C for center tube for Case B; Four probe locations are used along the flame edge, downstream of the tube exit. 73
4.8 Instantaneous three-dimensional analysis of streamlines and recirculation zones for Case B. The left image shows the streamlines around flame structure for tube 2, and the right image depicts for tube 1; Image in the middle shows time-averaged quiver plot for X slice at 5 mm indicating recirculation and reaction zones. 75

5.1 Conceptual sketch of the proposed trajectory mapping in composition space. The composition space is spanned by Z, c, and an unconstrained species μ (not frozen during reaction evolution). The blue-shaded surface $\mathcal{M}_R^+(\xi)$: Reduced-mechanism reaction manifold. Red-shaded plane $\mathcal{M}_c(\xi^S)$: iso-c manifold at state S for ξ. Green trajectory $R(\xi, t \to t_0)$: reconstruction from a given state S of ξ. Yellow trajectories $R(\Psi, t_0 \to t^*)$: forward integration of Ψ from Z_0 with perturbed reaction rate coefficients k_i towards $\mathcal{M}_c(\Psi^E)$, and reach the target composition $\phi^{\Psi^c}(k_i)$. Dashed black lines: relaxation of different reaction trajectories toward equilibrium (E). 83
5.2 Instantaneous snapshot on the combustor mid-plane showing temperature. Blue arrows indicate the flow direction of the oxidizer stream. Red arrows depict fuel stream issuing perpendicular into the oxidizer stream (inset). 89
5.3 Ensemble of one-cell reaction trajectories in C, Z, μ space, and two different un-constrained coordinate definition. Gray curves span different sample of reaction kinetics; one typical trajectory is emphasized with a thick black dashed line. The blue plane marks $C^\xi = 0.8$ constraint. 90
5.4 Instantaneous snapshot on the combustor mid-plane B showing time scale $\widetilde{\tau_C}$ in log-scale computed from Ψ. Blue arrows indicate the flow direction of the partially premixed stream. Region A represents the flame front, while region B represents the recirculation zone. 92
5.5 Scatter plot of T versus Z colored by $\widehat{\tau}_E$ on the flame front (Region A in Fig. 5.4). 93

5.6 Scatter plot of T versus Z colored by $\widehat{\tau}_E$ inside recirculation zone (Region B in Fig. 5.4). . . 94
5.7 Temporally averaged velocity magnitude for the different cases, with the isoline of Y_{OH} for the 70% and 95% H_2 by volume cases indicating the flame shape. . . 95
5.8 Instantaneous fields of normalized scalar dissipation rate $\hat{\chi} = \chi/\chi_{\mathrm{st}}^{\mathrm{ext}}$ (log scale) for different cases. The flame front is marked by an iso-contour of Y_{OH} at 10% of its peak value (white line), and the black line indicates the stoichiometric mixture-fraction contour $Z = Z_{\mathrm{st}}$ (black line). 97
5.9 Scatter plot of YOH versus mixture fraction at flame front location of different cases 98
5.10 Lifted-branch diffusion-flame-front state space: scatter of temperature T versus scalar dissipation rate χ for four cases (one per panel), extracted from a time-averaged mid-plane slice and filtered by location and $|Z - Z_{\mathrm{st}}| < \Delta Z$. Marker color indicates the OH production-rate variability $\beta_{\dot{\omega}_{\mathrm{OH}}} = \sigma(\dot{\omega}_{\mathrm{OH}})/|\mu(\dot{\omega}_{\mathrm{OH}})|$ from UQ. 101
5.11 Representative lifted-branch tracer-particle trajectories for CASE C7, shown in multiple views and colored by temperature. 103
5.12 Lifted-branch diffusion-flame-front PDFs of OH production-rate variability, $\beta_{\dot{\omega}_{\mathrm{OH}}} = \sigma(\dot{\omega}_{\mathrm{OH}})/|\mu(\dot{\omega}_{\mathrm{OH}})|$. Red curve: estimated PDF $\hat{f}_{\beta_{\dot{\omega}_{\mathrm{OH}}}}(x)$ (left axis). Blue bars: sample counts N_i in each histogram bin $H(\beta_{\dot{\omega}_{\mathrm{OH}}})$ (right axis). 104
5.13 Lifted-branch diffusion-flame-front PDFs of scalar dissipation rate χ (s^{-1}). Red curve: estimated PDF $\hat{f}_{\chi}(x)$ (left axis). Blue bars: sample counts N_i in each histogram bin $H(\chi)$ (right axis). 105

A.1 Plot of temporally averaged density values with standard deviation along three lines shown in the mid-section contour plot of the simulation for three independent grid levels (shown in inset). Level 3 results are shown in blue, level 4 results in green, and level 5 results in gray. 116

B.1 Ignition delay time (log-scale) comparison for H_2 at P = 10 atm and $\phi = 0.5$ as a function of inverse temperature (1000/T), Predictions from the FFCM-2 mechanism (━color=mplblue) are compared against the H_2 mechanism [11](━color=mplorange); Bars indicate the FFCM-2 uncertainty band. 118
B.2 Direct uncertainty propagation using the original FFCM-2 mechanism and covariance matrix for a representative counterflow flame at JICF-relevant conditions. Temperature is shown as a function of Bilger mixture fraction Z. The shaded region denotes the 5–95% interval, the red solid line denotes the ensemble median, and the black dashed line denotes the baseline solution. Insets highlight the uncertainty level near the stoichiometric mixture fraction. 120
B.3 Direct uncertainty propagation using the original FFCM-2 mechanism and covariance matrix for the same representative counterflow flame as in Fig. B.2. The OH production rate $\dot{\omega}_{\mathrm{OH}}$ is shown as a function of Bilger mixture fraction Z. The shaded region denotes the 5–95% interval, the green solid line denotes the ensemble mean, and the black dashed line denotes the baseline solution. Insets highlight the uncertainty level near the stoichiometric mixture fraction. 121

B.4 Direct uncertainty propagation using the original FFCM-2 mechanism and covariance matrix for a counterflow flame at strain rates approaching the steady extinction limit. The OH production rate $\dot{\omega}_{\mathrm{OH}}$ is plotted as a function of Bilger mixture fraction Z. The shaded region denotes the 5–95% interval, the green solid line denotes the ensemble mean, and the black dashed line denotes the baseline solution. Insets highlight the uncertainty level near the stoichiometric mixture fraction. The broadening of the uncertainty band demonstrates that OH-production variability increases substantially as the steady flame approaches extinction. 121

C.1 Convergence history of the variational-inference optimization for the covariance-transfer prior (*Prior*) and five additional runs initialized from randomized covariance matrices. The lower panel shows the normalized objective $\tilde{\mathcal{L}}(N)$ as a function of iteration N, and the upper panel shows the normalized iteration-to-iteration change, $\Delta\mathcal{L}(N)/\max(1, |\mathcal{L}(N-1)|)$. The inset gives a magnified view of the late-stage regime. 124

LIST OF TABLES

TABLE

3.1 Cases considered in the hydrogen jet-in-crossflow study. Cases A7 and C7 correspond to the experimental configurations of Steinberg et al. [12], while Cases A9 and C9 are hydrogen-enriched numerical extensions. 40

4.1 List of cases based on experiments [13; 14] 63

LIST OF APPENDICES

APPENDIX

A Grid Convergence **116**

B FFCM-2 for Hydrogen Fuel **118**

C Variational Inference Convergence **122**

LIST OF ACRONYMS

AFS Axial Fuel Staging

AMR Adaptive Mesh Refinement

DNS Direct Numerical Simulation

JICF Jet in Crossflow

LES Large-Eddy Simulation

FGM Flamelet-Generated Manifold

FPVA Flamelet Progress Variable Approach

S-FGM Strain-sensitive Flamelet-Generated Manifold

MTM Multi-Tube Micromixer

NSCBC Navier-Stokes Characteristic Boundary Conditions

UQ Uncertainty Quantification

ELBO Evidence Lower Bound

ABSTRACT

Hydrogen is an important low-carbon-intensity fuel pathway for dispatchable gas-turbine power generation, long-duration energy storage, and utilization of renewable electricity that cannot be used immediately by the grid. Its value in gas turbines is not that it is an efficiency-neutral replacement for direct electrification, but that it can provide fuel-flexible, high-power-density, dispatchable operation in energy systems where short-duration battery storage and direct electrification are insufficient. The corresponding combustor problem is substantially more difficult than conventional fuel substitution. Hydrogen's high reactivity, low ignition energy, broad flammability limits, strong differential diffusion, and intrinsic lean-flame-front instability alter flame position, local heat-release structure, flashback propensity, and unsteady response. For practical combustors, the relevant question is therefore not only whether hydrogen burns stably at a nominal operating point, but how local flow structures, mixture gradients, recirculation zones, and finite-rate chemistry determine where heat release anchors and whether a flame branch remains robust, lifts, extinguishes, or propagates upstream.

This dissertation investigates flame stabilization and unsteady dynamics in hydrogen-fueled reacting flows relevant to staged and distributed gas-turbine combustors. The study combines a canonical hydrogen jet in crossflow with a more application-oriented pressurized multi-tube micromixer. The jet-in-crossflow cases use a 2 mm injector, 70–95% hydrogen by volume, jet-to-crossflow momentum-flux ratios $J = 1.96$ and 8.41, jet velocities $U_j = 100$–342 m/s, jet Reynolds numbers $Re_j = 2600$–6000, a hot-crossflow velocity of 55 m/s, and $Re_c = 4.4 \times 10^4$. The multi-tube combustor contains 19 elements and is operated at approximately 11 bar, $\phi = 0.524$–0.530, crossflow velocities $U_c = 159$–162 m/s, crossflow temperatures $T_c = 758$–762 K, and fuel-jet velocities $U_j = 213$–303 m/s. The numerical approach combines large-eddy simulation with a strain-sensitive flamelet-generated manifold for reduced-model assessment and AMReX-based three-dimensional compressible finite-volume simulations with adaptive mesh refinement, embedded boundaries, detailed finite-rate chemistry, and mixture-averaged differential diffusion. The AMReX combustor simulations are interpreted as implicit large-eddy simulations, or resolved-large-eddy calculations: no explicit subgrid turbulence model is used, and the effective filter is set by the local AMR spacing and

the dissipation of the finite-volume scheme. These calculations resolve the dominant flame branches, shear layers, recirculation topology, wall-adjacent flow, and finite-rate chemistry, but they are not claimed to be uniform-grid direct numerical simulations of every turbulent scale in the full combustor.

The jet-in-crossflow results show that hydrogen flame stabilization is organized by branch-specific flow and chemistry histories rather than by a single global flame topology. At $J = 1.96$ and $U_j = 100$ m/s, the lee-stabilized branch anchors approximately two jet diameters downstream of the injector, where wake recirculation and relatively low-strain transport support a compact stabilization region. At $J = 8.41$ and $U_j = 200$–342 m/s, the lifted branch occupies a broader and more intermittent thermochemical state space. Representative lifted-branch trajectories sample mixture-fraction excursions of $\Delta Z \sim 0.4$; the local mixture-fraction distribution at one lifted-branch location has a mean $\widetilde{Z} \approx 0.18$, close to $Z_{st} \approx 0.17$, and a variance $\widetilde{Z''^2} \approx 0.03$; and two trajectories passing through the same spatial region differ in peak OH mass fraction by approximately a factor of five. These differences explain why reduced flamelet descriptions can reproduce the mean flame topology while missing high-intensity radical-production events in strained, three-dimensional lifted branches. Increasing the hydrogen content from 70% to 95% by volume at fixed $J = 8.41$ preserves the gross jet-penetration scale but changes the local stability response: the lifted-branch edge exhibits an ignition-extinction loop with $T \approx 550$–2100 K near Z_{st}, indicating that increased reactivity does not uniformly increase robustness when shear-layer strain, density variation, and differential diffusion are also modified.

The multi-tube micromixer analysis extends this branch-resolved interpretation to a pressurized, application-relevant combustor. The 19-element configuration is simulated at approximately 11 bar, with oxidizer velocities of $U_c \approx 159$–162 m/s, oxidizer temperatures of $T_c \approx 758$–762 K, fuel-jet velocities of $U_j \approx 213$–303 m/s, and global equivalence ratios near $\phi \approx 0.52$–0.53. Under these conditions, no flame branch propagates upstream into the tube elements. The stable response is associated with how heat release is distributed across the tube bundle: the dominant HRR remains in the jet shear layers, while the characteristic HRR in the low-speed recirculation regions is approximately 0.1 of the shear layer value. The joint PDFs of principal extensive strain rate and $\log_{10}(\mathrm{HRR})$ show that different tube locations occupy different strain-response regimes. Outer branches exhibit fragmented HRR distributions and earlier weakening by $x = 15$–20 mm downstream of the tube exit, whereas the center branch maintains non-negligible HRR at strain rates near and beyond the representative counterflow extinction band over the same axial range. This indicates that the center flame is more strain-tolerant and more coherently stabilized, while outer branches are more sensitive to wall confinement, neighboring-jet interaction, and transverse

recirculation. Geometrically, the center flame has the longest and most symmetric reaction zone, but its reaction zone width is still about 30% smaller in the closer-spaced transverse direction than in the wider-spaced direction. These results connect local combustion physics to gas-turbine design by showing that stability assessment should include flame penetration distance, recirculation-zone-to-shear-layer HRR ratio, local strain relative to extinction, mixture-fraction stratification, pressure/velocity fluctuation amplitude, and hydrogen fraction, rather than only bulk velocity or laminar flame speed.

Finite-rate chemistry and kinetic uncertainty provide a second quantitative measure of local flame robustness. Two uncertainty-aware approaches are developed: a state-reconstruction method for mapping reduced thermochemical states back to detailed-composition reaction trajectories and a covariance-transfer method for constructing an uncertainty model for reduced hydrogen chemistry. In the hydrogen jet-in-crossflow cases, the uncertainty response depends strongly on both hydrogen content and scalar-dissipation history. For the 70% H_2 cases, the lifted-branch OH-production variability, $\beta_{\dot{\omega}_{\mathrm{OH}}} = \sigma(\dot{\omega}_{\mathrm{OH}})/|\mu(\dot{\omega}_{\mathrm{OH}})|$, spans a broad range of approximately 0.6–2.0, whereas the 95% H_2 cases collapse primarily around $\beta_{\dot{\omega}_{\mathrm{OH}}} \approx 0.55$–$0.7$ with much weaker high-variability tails. The scalar-dissipation PDFs show the same separation: the 70% H_2 lifted branches sample broad high-χ distributions extending to approximately 20 s^{-1}, while the 95% H_2 cases are concentrated mainly below about 1 s^{-1}. Thus, increasing the hydrogen fraction from 70% to 95% shifts the lifted diffusion flame toward lower scalar-dissipation histories and substantially reduces the kinetic sensitivity of OH production. Across the jet-in-crossflow and multi-tube combustor configurations, the central conclusion is that hydrogen combustor stability is governed by local, branch-resolved quantities: heat-release placement, strain relative to extinction, scalar dissipation, mixture stratification, and state-dependent chemical sensitivity. High-fidelity implicit-LES calculations with finite-rate chemistry therefore provide a basis for identifying which flame branches are robust, which are extinction- or flashback-relevant, and which operating conditions should be targeted in future canonical experiments and simulation-based stability maps.

CHAPTER 1

Gas Turbine Engines and Coupled Flame Characteristics

1.1 Future of Gas Turbines

Gas turbines are expected to remain a central technology in future energy systems because they provide dispatchable, high-power-density electricity generation with fast load-following capability and mature large-scale infrastructure. Although renewable sources such as solar and wind are expanding rapidly, their output is inherently intermittent and often does not align with the temporal profile of electricity demand. This mismatch between generation and demand creates a continuing need for flexible power-generation technologies that can respond rapidly to fluctuations in grid conditions while maintaining grid reliability. Daily and seasonal mismatches between renewable generation and grid demand produce periods of excess energy followed by steep ramping requirements. This effect is illustrated in Fig. 1.1, where the well-known California net-load "duck curve" shows midday over-generation risk and a sharp evening ramp as solar generation declines, while the daily generation profile further highlights how renewable-rich systems can simultaneously experience excess energy during part of the day and significant dispatch needs later in the same operating cycle [1; 2]. These conditions place increasing value on grid assets that can start quickly, load-follow effectively, and provide reliable power when renewable output is insufficient.

Recent changes in electricity demand further amplify this need. In addition to traditional growth in industrial, commercial, and residential electricity consumption, emerging high-power digital infrastructure—especially large-scale data centers supporting artificial intelligence (AI) training and inference—is driving a substantial increase in projected electricity demand. As shown in Fig. 1.2, projected AI-related electricity demand is increasing rapidly, adding new pressure to already stressed electrical grids. This trend is especially important because the growth of AI infrastructure is concentrated, power-intensive, and often coupled with regions where electricity supply is already constrained.

Because of these system-level requirements, gas turbines remain highly attractive in future

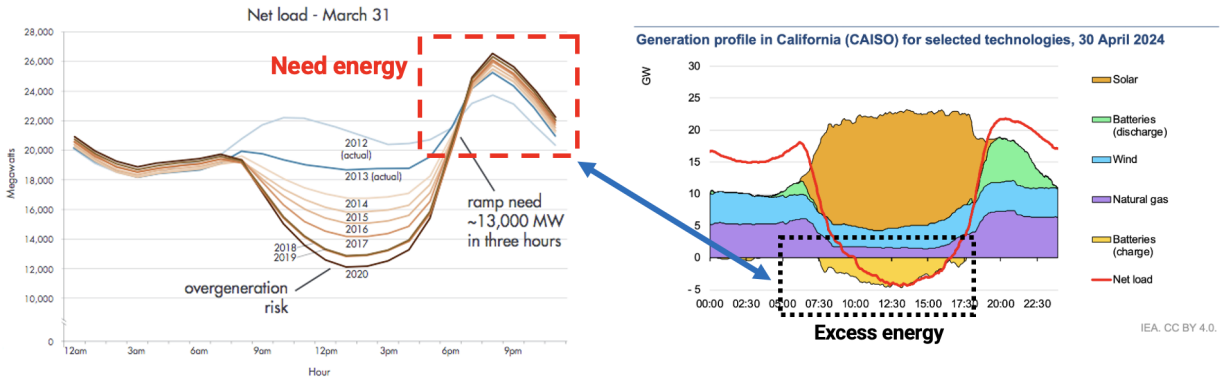


Figure 1.1: Illustration of the mismatch between electricity generation and demand in renewable-rich power systems. The left panel shows the California net-load "duck curve," including midday overgeneration risk and steep evening ramping demand, adapted from CAISO materials [1]. The right panel shows a daily California generation profile highlighting periods of excess renewable generation and later dispatch requirements, adapted from IEA analysis graphics [2].

low-carbon energy systems. They already play a major role in utility-scale and industrial power generation, and they offer several advantages that remain important in a changing grid: compactness, high specific power, relatively rapid startup, operational flexibility, compatibility with combined-cycle systems, and proven deployability across a broad range of power generation environments. Even as the energy mix evolves, gas turbines are therefore likely to remain indispensable as flexible generation assets that complement renewable power and help maintain grid stability.

A key question, however, is what fuels will support this future role. Hydrogen is an important candidate, but it should be described as a low-carbon-intensity energy carrier rather than as a universally zero-carbon fuel. Even when hydrogen is produced from renewable electricity, the pathway includes electrolysis, compression or liquefaction, storage, transport, and reconversion to mechanical or electrical power. These steps introduce life-cycle carbon intensity, material requirements, and thermodynamic losses. This distinction is important because direct use of electricity can be much more efficient than conversion through hydrogen or synthetic hydrocarbon fuels in applications where batteries are practical. For example, the International Council on Clean Transportation compared a battery-electric pathway with a renewable-electricity-to-liquid-fuel pathway for passenger vehicles and estimated total pathway efficiencies of approximately 72% and 16%, respectively [15]. Hydrogen combustion is therefore most compelling where its system value is not simply energy efficiency but dispatchability, storage duration, fuel flexibility, high-temperature heat, or compatibility with existing turbine infrastructure.

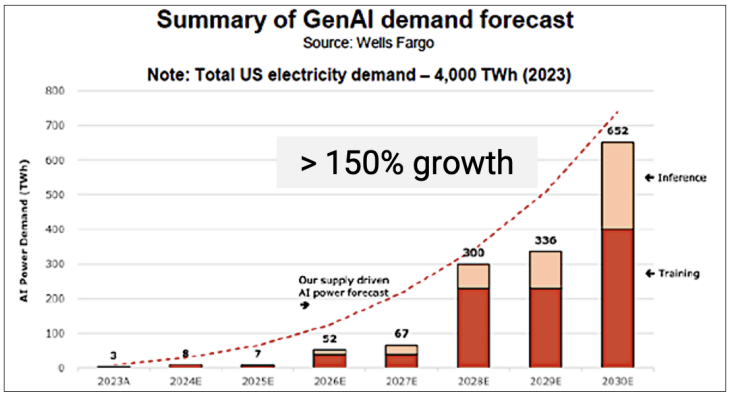


Figure 1.2: Projected growth in AI-related electricity demand, illustrating the increasing power requirements associated with large-scale training and inference infrastructure. Adapted from Wells Fargo analysis [3] of AI-driven electricity demand.

The idea of hydrogen-containing turbine fuel is also not new. Hydrogen-rich syngas has been central to gasification and integrated gasification combined cycle (IGCC) development for decades. DOE gasification program materials describe gasification as a baseline technology for producing hydrogen, substitute natural gas, fuels from coal, and concentrated CO_2 streams for sequestration, and they identify syngas as a fuel for electricity and steam generation as well as a building block for chemicals and hydrogen production [16]. In the same historical context, DOE's Vision 21 program described fuel-flexible integrated energy plants that could use gasification, advanced low-NO_x combustion systems, fuel-flexible turbines, fuel cells, hydrogen separation, and coproduction of electricity, syngas, hydrogen, chemicals, liquid fuels, and process heat [17]. These programs are important context for the present dissertation: hydrogen-capable gas turbines are not emerging from a blank technological history, but from a long sequence of syngas, IGCC, fuel-flexible turbine, and coproduction concepts.

The present opportunity differs from the earlier IGCC context because the fuel source and system requirement have shifted. Instead of using coal-derived syngas primarily for baseload power or coproduction, future low-carbon energy systems may use renewable hydrogen or hydrogen blends for flexible, dispatchable turbine operation. As illustrated in Fig. 1.3, renewable electricity can be converted into hydrogen, stored, and later supplied to a gas turbine either as a pure fuel or in blended operation with natural gas [4; 5]. If that hydrogen or syngas is not immediately required for electricity production, the historical gasification and Vision 21 frameworks also show that it can be redirected toward other products, including chemicals, liquid fuels, industrial hydrogen, or process heat [16; 17]. The combustor-design implication is that future turbines must tolerate variable fuel composition, variable demand,

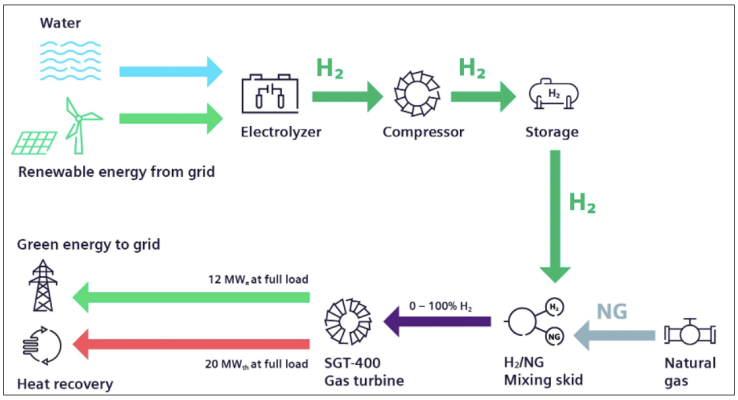


Figure 1.3: Conceptual pathway linking renewable electricity, hydrogen production, compression, storage, and subsequent gas-turbine power generation through hydrogen or hydrogen/natural-gas blended fueling. Adapted from Siemens Energy and HYFLEXPOWER project materials [4; 5].

and transient operation while still maintaining stable, low-emission flames.

Despite this promise, hydrogen-fueled gas turbines are not a straightforward extension of existing natural-gas systems. Recent reviews emphasize that the central difficulty is not simply fuel substitution but the need to control the stabilization and location of a highly reactive flame while simultaneously suppressing flashback, limiting NO_x formation, and avoiding combustion instability [18; 19]. Hydrogen offers several favorable properties, including high gravimetric energy content and broad flammability limits, but these same characteristics also imply high reactivity, high burning velocity, low ignition energy, and increased sensitivity to local flow structure and mixture distribution. In practical combustors, these features complicate premixer design, flame stabilization, emissions control, and operability over a wide range of conditions. As a result, hydrogen-capable gas turbines require combustor architectures that do more than accommodate a different fuel; they must actively manage where and how combustion occurs.

For this reason, the development of hydrogen-capable gas turbines has increasingly relied on advanced combustor strategies that distribute reactant preparation and reduce the burden placed on a single compact flame stabilization region. Recent reviews describe micromixer concepts, multi-tube premixers, distributed fuel injection, and staged or sequential-combustion architectures as key technological pathways for managing flashback resistance, heat-release distribution, emissions, and operational flexibility in hydrogen-fueled gas turbines [18; 20; 21]. This broader design trend is reflected across the gas-turbine industry. GE has developed AFS architectures for advanced heavy-duty turbines, Siemens Energy has described hydrogen-capable combustion strategies for flexible gas-turbine operation, and

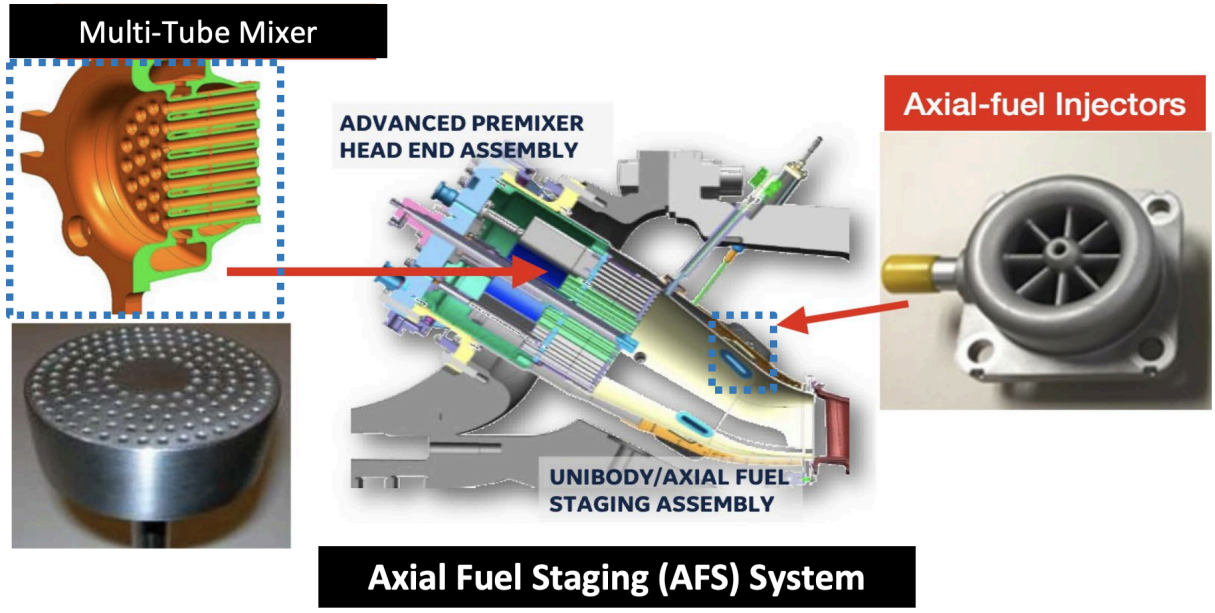


Figure 1.4: Representative axial fuel staging (AFS) combustor architecture integrating a multi-tube mixer, a premixing head-end assembly, and downstream axial-fuel injectors. The configuration illustrates how upstream premixing and downstream staging can be combined to distribute heat release across multiple combustor zones. Adapted from advanced gas-turbine combustor development materials in Hughes et al. [6] and National Energy Technology Laboratory and GE Power [7].

Ansaldo Energia has advanced sequential-combustion concepts for high-hydrogen systems [22; 23; 24; 25]. Although the terminology varies across manufacturers, the underlying objective is similar: to achieve more effective control of flame position, mixture preparation, and heat-release distribution than is possible in a conventional single-zone combustor.

Among these approaches, GE's AFS system provides a useful representative example because it combines distributed upstream reactant preparation with downstream staged fuel addition in a single integrated combustor concept. The corresponding architecture is shown in Fig. 1.4.

1.2 Axial Fuel Staging in Gas Turbines

Axial fuel staging (AFS) is one example of the broader shift toward distributed and multi-zone combustor architectures for hydrogen-capable gas turbines. In contrast to a conventional combustor, in which most of the mixture preparation and heat release are concentrated in a single primary zone, AFS combines distributed upstream premixing with a second, axially separated fuel-delivery location. This arrangement provides additional control

over flame stabilization, local equivalence ratio, and the axial distribution of heat release, thereby improving flexibility over a broad operating range [22; 23]. Figure 1.4 shows a representative AFS combustor architecture composed of a multi-tube micromixer (Multi-Tube Micromixer (MTM)), a premixing head-end assembly, and downstream axial-fuel injectors. Here, the term MTM refers specifically to the upstream distributed-mixing hardware, while the term multi-tube combustor is used more broadly to describe the reacting combustor configuration formed by the MTM together with the downstream reaction zone that it feeds. The figure therefore illustrates that AFS is an integrated system in which distributed upstream reactant preparation and downstream staged fuel delivery are designed together to create a multi-zone combustion process.

The first major component is the MTM, shown on the left side of Fig. 1.4. In this component, air enters from upstream and passes through an array of small tubes, while fuel is introduced through multiple distributed injection locations associated with these passages. Mixing therefore occurs in a spatially distributed manner across many small streams rather than in a single, highly loaded premixing passage. The resulting prepared reactive mixture then exits the MTM and enters the downstream combustor. In advanced gas-turbine combustor development, this type of hardware is intended to improve reactant preparation and support high-efficiency, low-emissions operation by avoiding an overly concentrated single mixing region [6; 26]. For hydrogen-rich operation, the MTM is especially important because this distributed premixing strategy can reduce flashback susceptibility relative to configurations in which the entire fuel flow is processed through a single compact premixer. At the same time, it creates a combustion environment that is intrinsically nonuniform: the mixture entering the downstream chamber is distributed across many jets and passages, so local equivalence ratios, velocity gradients, and scalar gradients need not be spatially uniform even when the overall operating condition is nominally steady.

The second major component is the premixing head-end assembly, located in the center of the figure. This section receives the mixture prepared by the MTM and establishes the primary upstream flame-supporting environment. In premixed gas-turbine combustors, the head-end assembly governs how the prepared mixture is introduced into the combustor and how the primary reaction zone is formed and stabilized. GE's combustor descriptions emphasize that this upstream premixer remains a central element of the overall combustion system even when downstream staging is employed [22; 27]. Accordingly, the head-end assembly forms the first stage of the staged-combustion process and defines the primary upstream combustion zone. From a combustion-physics standpoint, this region is important because it sets the initial flame topology and establishes the local balance among recirculation, convective transport, mixing, and chemical conversion that determines where the upstream flame

can persist.

The third major component is the set of axial-fuel injectors, shown on the right side of Fig. 1.4. These injectors introduce additional fuel farther downstream in the combustor, thereby creating a second controllable combustion zone in addition to the upstream head-end region. This downstream staged-fuel circuit is the defining feature of AFS. Its function is not merely to add fuel downstream but to provide an additional degree of control over flame stabilization, local equivalence ratio, and axial heat-release distribution. By shifting part of the combustion process downstream, the combustor reduces the fraction of total heat release confined to the primary upstream zone. This redistribution can shorten the residence time of the hottest combustion products and thereby help reduce thermal NO_x formation, while also improving turndown capability and extending the emissions-compliant operating window [22; 23].

These three hardware elements define the engineering rationale of AFS. The MTM provides distributed upstream fuel–air preparation, the head-end assembly establishes the primary upstream flame zone, and the downstream axial-fuel injectors provide a second, spatially separated fuel-delivery location. As a result, combustion can be distributed across multiple axial zones rather than being confined to a single compact reaction region. From an engineering standpoint, this architecture is attractive because it can extend low-load operability, broaden the emissions-compliant operating range, and provide greater flexibility in responding to changes in load conditions and fuel composition [22; 6].

At the same time, the same features that make AFS attractive also make its combustion behavior more difficult to analyze. In a conventional single-zone combustor, combustion behavior is often dominated by one primary flame-stabilizing region. In an axially staged combustor, by contrast, the overall response is controlled by the coupled interaction of upstream mixture preparation, head-end flame stabilization, downstream staged fuel addition, and axial redistribution of heat release. The combustor, therefore, behaves as a multi-zone reacting-flow system in which local burning modes can differ from one region to another and can evolve differently over time. Within this multi-zone architecture, the upstream multi-tube combustor is especially challenging because its behavior is controlled by the combined effects of distributed injection, tube-bundle geometry, local transport, and multi-flame interaction. Upstream jet interactions within the MTM produce mixture stratification before the flow enters the combustor, and this nonuniformity is subsequently amplified by geometry-induced strain and confinement effects in the downstream chamber. Once combustion is established, the flame branches associated with different tubes do not behave uniformly: stabilization, heat-release structure, local radical production, and unsteady response can vary substantially across the bundle, particularly between the center and near-wall regions.

Further complexity arises from asymmetric recirculation, shear-layer burning, and the recurrent appearance of reaction pockets and fuel filaments. The upstream multi-tube combustor should therefore be regarded as a coupled reacting-flow subsystem whose local flame behavior is essential for understanding and improving the overall AFS architecture.

Multi-tube combustors should be regarded as coupled reacting-flow systems rather than as collections of independent flame elements. In these configurations, combustion is shaped by the interaction of distributed injection, geometric confinement, local flow redistribution, recirculation, and flame-flame coupling, so the behavior of any one flame branch cannot be interpreted in isolation from the surrounding flow and neighboring burning regions. This complexity is further intensified in hydrogen combustion, where high reactivity, low ignition energy, broad flammability limits, and strong sensitivity to local transport and mixture nonuniformity amplify the effects of injector-to-injector variation and spatial flow nonuniformity. As a result, the key scientific challenge is not only to describe the overall flame structure but also to understand how local burning modes are established, why different regions of the combustor behave differently, and how local transport and chemistry shape both flame stabilization and dynamic response. More broadly, this complexity also implies that combustor stability cannot always be interpreted as a purely deterministic yes-no outcome. Near operating limits, combustion systems often approach instability through intermittent and fluctuation-sensitive transitions. Therefore, the relevant question is not only whether the combustor is globally stable on average, but also how local regions move toward instability, which flame branches first exhibit intermittent behavior, and how likely such local excursions are to grow into larger-scale unsteady responses. These questions motivate the next four sections, which discuss flame stabilization, the transition to combustion instability, unsteady flame dynamics, and the role of chemistry and kinetic uncertainty as the linked physical themes that organize the remainder of this dissertation.

A useful distinction is needed before those topics are introduced. Hydrogen flames can exhibit intrinsic flame-front or thermo-diffusive instabilities associated with differential diffusion and preferential transport in lean premixed flames; these instabilities can increase local flame wrinkling and consumption speed even without a combustor-scale acoustic mode [28]. This dissertation uses the terms flame-front instability, flashback, and combustor instability for different phenomena. Flame-front instability refers to local cellular or thermo-diffusive behavior of the flame surface. Flashback refers to upstream propagation of the reaction zone into the premixer or tube elements. Combustor instability refers to larger-scale unsteady response, including pressure-coupled thermoacoustic behavior. These mechanisms can interact, but separating them is important for interpreting the simulation results and for translating them into gas-turbine design guidance.

1.3 Flame Stabilization in Reactive Flows

The complex behavior of hydrogen multi-tube combustors ultimately depends on a more fundamental question: where combustion is sustained, by what local mechanisms it is anchored, and how those anchoring mechanisms change across different flow environments. Distributed injection, local flow redistribution, geometric confinement, and multi-flame interaction all influence combustor response through their effect on flame stabilization. Viewed in this way, flame stabilization provides a natural physical framework for understanding not only multi-tube combustors but also reactive-flow systems more broadly, ranging from canonical jet flames to practical staged combustors.

Flame stabilization is a central problem in reactive flows because it determines whether a localized burning region can be sustained under continuous flow-through conditions. In practical combustors, it governs where heat is released, how the flame interacts with the surrounding flow, and whether operation remains efficient, robust, and safe. For this reason, flame stabilization plays a fundamental role across a wide range of configurations, including premixed flames, reacting jets in crossflow, micromixer combustors, and multi-injector gas-turbine systems.

In general, flame stabilization arises from a balance among fluid transport, chemical conversion, and thermal feedback. A flame can be sustained only when local mixing, residence time, and reaction rates combine in a manner that allows heat release to persist against convective losses, strain, scalar dissipation, and dilution. Depending on the configuration, this balance may be established through different physical mechanisms, including recirculation-assisted anchoring, shear-layer stabilization, autoignition-assisted burning, reaction in partially premixed mixtures, or combinations of these processes. Previous studies of reacting jets in crossflow, practical model combustors, and micromixer flames show that stabilization is not governed by chemistry alone but by the coupled interaction of flame structure with the surrounding flow field and geometric confinement [29; 30; 31; 32; 33; 34; 35].

This problem becomes especially important in hydrogen combustion because hydrogen's high reactivity, low ignition energy, broad flammability limits, and strong preferential transport amplify the influence of small variations in the local flow environment. As a result, local changes in strain rate, scalar dissipation, recirculation strength, wall proximity, or equivalence ratio can substantially modify burning behavior, flame position, flashback propensity, and local extinction resistance. Reviews of hydrogen gas-turbine combustion therefore identify flame stabilization, together with flashback, autoignition, NO_x formation, and thermoacoustic response, as a central challenge in the development of practical hydrogen combustors [18; 20; 21; 36].

A physically predictive understanding of combustor behavior therefore requires more than global performance measures such as pressure loss, overall emissions, or mean outlet temperature. These quantities remain important for system-level assessment, but they do not by themselves reveal why a flame stabilizes in one region rather than another, why a change in geometry alters the burning mode, or why neighboring injectors behave differently under nominally similar conditions. A more fundamental interpretation must instead identify the local flow structures, mixture fields, transport processes, and reaction environments that organize burning in space. This perspective is particularly important in spatially heterogeneous systems such as the multi-tube combustor, where stabilization is governed not by a single uniform mechanism but by multiple interacting local environments.

1.4 Transition to Combustion Instability

Flame stabilization alone does not fully characterize combustor behavior because the loss of stability is often not realized as a single abrupt threshold in practice. In turbulent reacting flows, the transition to instability frequently proceeds through intermittency or other intermediate dynamical states rather than through a clean deterministic jump. This has been shown in canonical thermoacoustic studies, where instability emerges from combustion noise through intermittent organized bursts, and also in flashback studies, where flames can repeatedly intrude upstream and then retreat before a full transition occurs [37; 38; 39; 40; 41; 42; 43; 44]. Experimental studies of swirl-stabilized combustors further show that the onset of instability is closely linked to changes in flame macrostructure and local stabilization mode, and that fuel composition can shift the transition points even when the geometric configuration is unchanged [45; 46].

This transition pathway has been documented in several complementary ways. Nair et al. [37] showed that combustion-driven oscillations are preceded by intermittent bursts embedded within low-amplitude aperiodic fluctuations. George et al. [38] further showed that the global transition begins in localized inceptive regions where heat-release fluctuations strengthen before large-scale organized motion appears across the combustor. In annular combustors, Roy et al. [39] reported a sequence from combustion noise to low-amplitude thermoacoustic instability through intermittency, while Singh et al. [40] showed that additional intermediate states, including mixed-mode oscillations, can arise before high-amplitude instability is reached. In the flashback literature, Schneider and Steinberg [41] observed that, over a range of conditions between stable burning and total flashback, the flame intermittently propagated through the bluff-body boundary layer into the reactant feed tube before retreating back to the combustor. Willems [42] further concluded that unconfined flash-

back is rather a statistical phenomenon, where the chance of flashback increases as the bulk velocity is reduced. In a lean hydrogen reheat combustor representative of an industrially relevant sequential-combustion configuration, Floris et al. [43] likewise treated intermittent flashback as an extreme event and showed that identifiable precursor states exist before flashback onset. These studies indicate that near the instability boundary, combustion stability is better interpreted statistically—in terms of the frequency, duration, and spatial growth of intermittent excursions—than as a single sharply defined threshold [37; 38; 41; 42; 43].

This perspective is important because it shifts the problem from a purely binary classification of stable versus unstable to a question of where instability first develops and what local mechanisms amplify it. The relevant quantities are therefore not only the mean operating condition but also the spatial distribution of heat-release fluctuations, the residence time spent in intermittent states, and the sensitivity of local flame structure to perturbations in flow, mixing, and reaction [38; 45; 47]. A combustor that is nominally stable on average may still be close to transition if localized fluctuations repeatedly grow in flame-anchoring regions, or if changes in flame macro-structure move the system toward a more strongly coupled response [38; 45; 46]. This point is also relevant to axially staged combustors. Public AFS studies show that first- and second-stage flames can couple to different acoustic modes and timescales, and that the second-stage flame can exhibit flapping and periodic partial extinction depending on its position relative to the acoustic mode shape [48; 49]. These results support the view that transition in staged combustors should be interpreted locally and branch-wise.

For hydrogen combustion, this issue becomes even more important because fuel chemistry directly modifies the flame features that enter the instability mechanism. Hydrogen enrichment changes flame shape, flame length, flame attachment tendency, burning rate, and the location of the dominant heat release zone. These changes shift both instability limits and the phase relation between unsteady heat release and acoustics [50; 51; 52; 53]. In partially premixed systems, the feedback loop is also altered by interactions between velocity fluctuations and equivalence-ratio fluctuations, which can produce local extinction, reignition, and additional convective delay in the heat-release response [47]. More generally, even outside thermoacoustic or flashback problems, detailed stability analyses of reacting flows have shown that finite-rate chemistry and transport can shift flame structure and heat release location enough to modify the predicted instability behavior [54]. The transition to combustion instability in hydrogen-fueled systems is, therefore, controlled by chemistry–transport coupling, which determines how local perturbations are converted into sustained heat-release oscillations. This is one of the central motivations for the chemistry-focused and uncertainty-aware analysis developed in this dissertation.

1.5 Unsteady Flame Dynamics in Hydrogen Combustors

Beyond the onset of global instability, combustor behavior must also be understood within each operating state because a flame that is globally stable can still exhibit strong local motion, intermittent weakening, branch reorganization, or unsteady heat-release variation. The transition problem discussed above concerns how instability emerges; the present section instead focuses on how different flame regions behave dynamically over time once a reacting-flow configuration is established.

Previous experimental studies of multi-nozzle and micromixer combustors have shown that neighboring flames in nominally regular injector arrays can differ not only in mean flame shape but also in fluctuation level, luminosity, and instability behavior [55; 56; 57; 58]. These observations indicate that local flow redistribution, injector interaction, and branch-to-branch coupling can produce dynamically distinct flame environments within the same combustor. Numerical studies support this interpretation by showing that hydrogen combustors can contain multiple coupled burning regions associated with recirculation, mixing layers, and shear-layer reaction, each with its own local timescales and dynamic response [32; 35; 34].

In gas-turbine combustion, unsteady flame dynamics are particularly important because heat-release oscillations can couple with acoustic modes, producing thermoacoustic instability; however, important dynamic behavior also occurs below that level through local flame displacement, intermittent branch motion, and nonuniform responses to perturbations. Hydrogen intensifies these issues because higher reactivity, shorter chemical timescales, and stronger preferential transport can alter flame length, flame position, local heat-release distribution, and the sensitivity of the flame to flow forcing. Reviews of hydrogen combustion dynamics, therefore, emphasize that hydrogen enrichment can substantially modify flame response and thermoacoustic behavior through its influence on flame structure, flame position, and local burning rates [18; 19; 20].

For multi-tube and staged combustors, this means that unsteady flame behavior must be interpreted both locally and globally. Different flame branches may experience different mixing histories, different recirculation environments, and different local transport balances, so they need not respond identically even under the same nominal operating conditions. A complete physical interpretation must therefore explain not only where the flame is anchored on average but also how different burning regions fluctuate, reorganize, and exchange influence over time.

1.6 Role of Chemistry and Kinetic Uncertainty in Hydrogen Combustion and Simulation

Chemistry plays a central role in this problem because flame stabilization, transition to instability, and unsteady flame response depend not only on the surrounding flow field but also on how chemical conversion proceeds under local transport conditions. In hydrogen flames, this dependence is especially strong because the burning structure is controlled by fast chain-branching chemistry, rapid radical-pool development, and strong differential diffusion of light species and radicals. As a result, two regions with a similarly large-scale flow structure may still behave differently if they occupy different thermochemical states or reach those states through different transport histories.

This issue is especially important when combustor stability is viewed as a transition problem rather than a purely binary outcome. If the onset of instability is fluctuation-sensitive and proceeds through intermittent local reorganization, then the flame response to perturbation depends directly on local chemistry. In hydrogen combustion, chemistry influences flame position, heat release compactness, convective timescales, and the phase relation between unsteady heat release and the surrounding flow or acoustic field. Previous studies, therefore, report that hydrogen can alter thermoacoustic instability characteristics in either a stabilizing or destabilizing manner through its influence on flame structure and flame location. This means that chemistry is not merely an auxiliary closure embedded within the simulation but an active part of the mechanism by which local fluctuations are either damped or amplified.

The role of chemistry is also critical from a simulation standpoint. Many practical combustor studies rely on reduced-order combustion descriptions because they are computationally efficient and often capture large-scale flame structures reasonably well. However, hydrogen flames present a more demanding modeling problem because finite-rate chemistry and differential diffusion can strongly influence local flame behavior. This is particularly true when the objective is not only to reproduce the mean flame shape but also to interpret branch-dependent flame structures, local reaction-zone differences, transition behavior, and unsteady response. For these reasons, high-fidelity simulations with finite-rate chemistry remain essential for identifying the physical mechanisms that underlie hydrogen flame behavior, especially in spatially heterogeneous combustors where local chemistry–transport coupling is central to the problem.

This perspective also motivates the uncertainty-aware analysis developed later in the dissertation. If chemistry materially influences whether local perturbations decay, persist intermittently, or grow toward instability, then uncertainty in the kinetic description becomes

physically relevant to how robustly that flame behavior can be interpreted. Kinetic uncertainty is therefore not introduced here merely as a numerical formality. It is used because the chemistry itself helps determine the local robustness or fragility of the reacting state. Uncertainty quantification provides a systematic way to assess that sensitivity, identify flame regions that are especially chemistry-dependent, and distinguish conclusions that are robust from those that depend strongly on uncertain reaction kinetics.

1.7 Chapter Summary

Hydrogen-capable gas turbines will play an important role in future low-carbon power systems because they combine fuel flexibility with the dispatchable, high-power-density operation required to complement renewable electricity. At the same time, hydrogen combustion introduces a particularly demanding flame-control problem. Its high reactivity, broad flammability limits, low ignition energy, and strong preferential transport make flame stabilization, emissions control, flashback resistance, and unsteady flame response more difficult to manage than in conventional natural-gas combustors. These challenges have motivated the development of staged and distributed combustor architectures, including multi-tube premixers, micromixer concepts, and axial fuel staging systems, which seek to distribute mixture preparation and heat release across multiple regions of the combustor.

The preceding discussion shows that four linked combustion-physics themes are central to this dissertation. The first is flame stabilization: understanding where combustion is anchored, what local mechanisms sustain it, and how those mechanisms vary across recirculation zones, shear layers, and partially premixed regions. The second is transition to instability: understanding how nominally stable operation approaches intermittent and ultimately global unstable responses. The third is unsteady flame dynamics: understanding how different flame branches fluctuate, reorganize, and respond to perturbations in spatially heterogeneous combustor environments. The fourth is the role of chemistry: understanding how finite-rate chemistry, radical-pool development, and preferential transport influence local burning behavior and, therefore, shape stabilization, transition, and dynamic response. A predictive interpretation of hydrogen combustor behavior, therefore, requires a local, physics-based framework that connects flow structure, transport, and chemistry to the observed flame behavior. High-fidelity simulation is particularly well suited to this problem because it can capture the coupled effects of flow, transport, differential diffusion, and geometric confinement while also resolving the chemistry needed to explain why different regions of the flame exhibit different stabilization characteristics and different dynamic responses. These ideas define the physical scope of the dissertation and motivate the chapter organization below.

1.8 Scope of the Dissertation

Based on the preceding context, this dissertation investigates flame stabilization and unsteady dynamics in complex hydrogen-fueled reacting-flow systems relevant to advanced gas-turbine combustion, with particular emphasis on the role of finite-rate chemistry. The overall objective is to develop a predictive, physics-based understanding of how hydrogen flames are established, sustained, and dynamically modified in spatially heterogeneous combustor environments. The quantitative operating envelope considered here spans hydrogen contents from 70% to 95% by volume in the transverse-jet studies, jet-to-crossflow momentum-flux ratios $J = 1.96$ and 8.41, jet Reynolds numbers $Re_j = 2600$–6000, crossflow Reynolds numbers up to $Re_c = 4.4 \times 10^4$, and a pressurized multi-tube combustor at approximately 11 bar with $\phi = 0.524$–0.530, crossflow velocities of 159–162 m/s, and fuel-jet velocities of 213–303 m/s. These values are not intended to cover an entire engine operating map. Instead, they define a set of combustor-relevant regimes in which local shear, recirculation, stratification, and finite-rate chemistry can be isolated and interpreted.

The dissertation is organized around three connected research questions. First, what local flow and mixture conditions determine whether a hydrogen flame branch anchors, lifts, weakens, or approaches extinction? Second, which aspects of this behavior can be represented by reduced flamelet-based descriptions, and which require finite-rate chemistry with differential diffusion and three-dimensional transport? Third, how can high-fidelity simulation results be translated into design-oriented stability information for hydrogen gas turbines, including quantities relevant to flashback avoidance, branch robustness, and local instability precursors?

The resolution regime is also defined explicitly. The reduced-order jet-in-crossflow comparison uses conventional LES with a strain-sensitive flamelet-generated manifold. The detailed AMReX calculations are treated as implicit LES or resolved-large-eddy simulations with detailed finite-rate chemistry, rather than as Reynolds-averaged calculations or full-device direct numerical simulations. In these AMReX calculations, the flame front, dominant shear layers, recirculation topology, wall-adjacent flow, and large coherent vortices are resolved by AMR, while motions below the local grid scale are represented by the numerical dissipation of the finite-volume scheme. The conclusions are therefore framed around resolved branch-wise flame/transport mechanisms and grid-aware stability indicators, not around claims of resolving the complete Kolmogorov-scale turbulence field of a practical combustor.

The main contributions are as follows. The first contribution is a quantitative comparison of reduced-order and high-fidelity descriptions for hydrogen jets in crossflow, showing

that large-scale topology can be reproduced while branch-specific chemistry-transport behavior remains difficult to represent with a compact flamelet table. The second contribution is a three-dimensional analysis of a pressurized multi-tube hydrogen combustor, showing that nominally identical tube elements form distinct stabilization environments because of confinement, recirculation, local stratification, and branch-to-branch interaction. The third contribution is a chemistry-sensitive uncertainty analysis that uses kinetic uncertainty not only as an output error bar but also as a diagnostic for chemically fragile flame regions. A further practical contribution is the definition of local stability-map variables for simulation-based combustor design: flame penetration distance, recirculation-zone-to-shear-layer heat-release ratio, local strain/extinction proximity, scalar-dissipation level, thermochemical-state variability, and pressure/velocity fluctuation amplitude.

These modeling and physics questions are pursued throughout the subsequent chapters of this dissertation:

- **Chapter 2: Numerical Methods for High-Subsonic Hydrogen Combustion.** This chapter answers what numerical framework is required to simulate the relevant regimes. The detailed calculations use a three-dimensional compressible finite-volume reacting-flow solver with adaptive mesh refinement, embedded boundaries, characteristic boundary conditions, detailed finite-rate chemistry, and mixture-averaged differential diffusion. The chapter also clarifies the numerical scope: the jet-in-crossflow study includes both large-eddy simulation with a strain-sensitive flamelet-generated manifold and detailed finite-rate AMReX calculations, while the multi-tube analysis uses the AMReX-based detailed-chemistry framework in an implicit-LES/resolved-large-eddy regime to resolve local flame/transport interactions in a practical geometry.

- **Chapter 3: Fluid-Chemistry Interactions and Modeling Challenges in Hydrogen Jets in Crossflow.** This chapter answers how turbulence, three-dimensional shear-layer dynamics, and differential diffusion alter hydrogen flame states relative to laminar or tabulated flame references. It considers 70% and 95% hydrogen by volume, $J = 1.96$ and 8.41, $U_j = 100$–342 m/s, $Re_j = 2600$–6000, and $Re_c = 4.4 \times 10^4$. Its resolution regime combines an LES-S-FGM reduced model with a detailed-chemistry reference in which the relevant flame branches and large-scale vortex structures are resolved sufficiently to compare branch-wise thermochemical trajectories. The contribution is a quantitative branch-wise interpretation of the lee-stabilized and lifted flame branches and a demonstration that lifted-branch trajectories sample broad mixture-fraction and progress-variable ranges that are not fully captured by the reduced manifold.

- **Chapter 4: Flame Stabilization and Characteristics in a Multi-Tube Mi-**

cromixer. This chapter answers how a practical distributed-injection combustor remains stable, and which local mechanisms could become flashback-relevant. The 19-element combustor is analyzed at approximately 11 bar, $\phi \approx 0.53$, crossflow velocities of 159–162 m/s, and fuel-jet velocities of 213–303 m/s. The AMReX calculation is an implicit LES at approximately 5.0×10^8 cells, with finest spacing 48.75 μm and near-wall $y^+ \approx 0.5$, so it resolves the dominant branch dynamics while remaining filtered at the grid scale. The contribution is a quantitative connection between local heat-release distribution and stability: in the stable cases studied here, dominant heat release remains in the shear layers, while heat release in low-speed recirculation zones is approximately one order of magnitude smaller and does not drive upstream flame propagation into the tube elements.

- **Chapter 5: Kinetic Uncertainty in Complex Reacting Systems.** This chapter answers how finite-rate chemistry and kinetic uncertainty influence the interpretation of local flame robustness. It introduces state-reconstruction and covariance-transfer methods and applies them to resolved thermochemical states extracted from the implicit-LES AMReX fields and jet-in-crossflow calculations. The contribution is to use chemistry uncertainty as a local diagnostic for fragile thermochemical states, especially in partially reacted, high-scalar-dissipation, or near-extinction regions.

- **Chapter 6: Conclusions and Future Directions.** This final chapter synthesizes the main results and translates them into gas-turbine design implications. It proposes a simulation-based stability-map perspective in which global operating parameters are supplemented by local quantities that identify whether a flame branch is securely stabilized, close to extinction, or capable of upstream propagation.

CHAPTER 2

Numerical Methods for High-Subsonic Hydrogen Combustion

The simulations in this dissertation use two related but distinct numerical descriptions. The reduced-order comparison in Chapter 3 uses large-eddy simulation (LES) with a strain-sensitive flamelet-generated manifold. The detailed calculations in Chapters 3–5 use a three-dimensional compressible finite-volume AMReX-based solver with adaptive mesh refinement, embedded boundaries, detailed finite-rate chemistry, and mixture-averaged differential diffusion. These AMReX calculations are interpreted as implicit LES or resolved-large-eddy simulations: no explicit subgrid-scale turbulence model or Reynolds-averaged Navier–Stokes closure is used, and the effective filter is set by the local AMR spacing together with the dissipation of the finite-volume discretization. The jet-in-crossflow detailed calculations are refined enough to resolve the selected flame branches, near-wall region, and dominant wake/shear-layer structures used for model comparison, while the multi-tube calculations should be interpreted as AMR-assisted implicit LES of a practical combustor rather than as uniform-grid direct numerical simulations of every turbulent scale in the full device. This distinction is important because the conclusions below are based on resolved local flame/transport mechanisms, while the remaining numerical uncertainty is assessed through grid refinement, validation against OH-PLIF structure, and comparison between reduced-order and detailed-chemistry descriptions.

High-subsonic turbulent hydrogen combustion is difficult to study because the relevant flow and reaction physics span a very wide range of coupled spatial and temporal scales. In multi-tube and micromixer combustors, distributed injection and complex internal geometry generate strongly three-dimensional turbulent flow fields with thin shear layers, recirculation zones, and localized mixing structures. In particular, MTM relies on many small, high-velocity air passages and jet-in-crossflow fuel injection to intensify mixing and reduce flashback risk, which further strengthens the small-scale turbulent character of the flow. A fully detailed description of such turbulence would, in principle, require access to scales ex-

tending toward the Kolmogorov scale, making the problem computationally demanding even before combustion is considered [59; 35].

Hydrogen combustion adds a second and more severe scale-separation problem. Because hydrogen flames can exist as very thin reaction fronts and remain highly sensitive to strain, differential diffusion, and local mixture inhomogeneity, the flame front itself must be resolved with sufficient fidelity to capture the chemistry–transport coupling that governs stabilization and burning behavior [60; 61]. At the same time, the combustor is a much larger system, with characteristic dimensions on the order of $O(10^{-1})$ to $O(10^{0})$ m. The resulting problem is therefore inherently multiscale: physically meaningful simulation must retain the full three-dimensional combustor context while still resolving the small localized structures that organize the flame.

The problem is further complicated by a substantial separation of characteristic timescales. Because MTM configurations employ relatively high jet velocities to promote rapid mixing and flashback-resistant operation, the flow remains in a high-subsonic regime for which a compressible formulation is appropriate [59]. That choice, however, introduces additional numerical difficulty, particularly in the treatment of open inflow and outflow boundaries, for which characteristic-based formulations such as Navier-Stokes Characteristic Boundary Conditions (NSCBC) are important [62]. At the same time, finite-rate hydrogen chemistry is stiff, and the stable timestep can be driven down to the order of $O(10^{-10})$ to $O(10^{-9})$ s by the combined constraints of acoustics, transport, and chemical source terms, whereas the convective flow-through and flame-development times in the laboratory-scale domains considered here are much longer, typically on the order of $O(10^{-3})$–$O(10^{-2})$ s, with still longer times required for full combustor transients. Time-resolved simulation of the full problem is therefore limited simultaneously by the need to resolve very small numerical timescales and much larger physical evolution times.

These combined difficulties motivate the use of a specialized numerical framework. The simulations in this dissertation are performed with a finite-volume compressible reacting-flow solver built on the AMReX framework [8; 63; 64]. The solver is designed specifically for hydrogen-combustion problems in which the important physics are strongly localized in space but dynamically coupled across a much larger three-dimensional domain. It solves the compressible Navier–Stokes equations with multi species transport on block-structured Cartesian meshes, represents practical injector geometry with embedded boundaries, and employs Adaptive Mesh Refinement (AMR) to place the highest resolution only near flame fronts, shear layers, and other dynamically important regions. In this framework, AMR provides a practical means of resolving the sharply localized structures that govern the flow while avoiding the prohibitive cost of uniformly fine resolution over the full combustor domain.

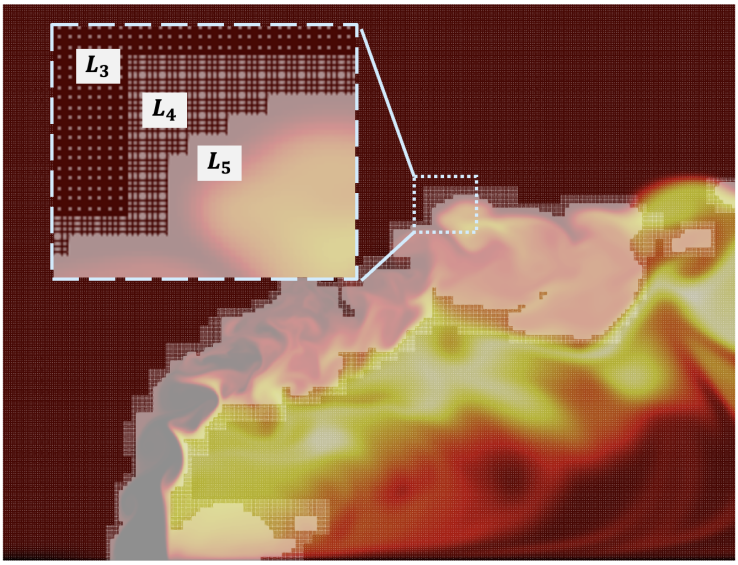


Figure 2.1: Example of block-structured adaptive mesh refinement used to concentrate resolution near localized reacting-flow structures in an AMReX-based solver [8].

Figure 2.1 illustrates the AMR strategy used throughout this dissertation. Rather than resolving the entire domain with a uniformly fine mesh, the solver places the highest resolution only where strong density gradients and flame-associated structures appear. This capability is essential for the present Jet in Crossflow (JICF) and MTM simulations, where the physically important reacting layers occupy only a limited fraction of the full domain. The solver also targets the temporal and algorithmic difficulties associated with detailed reacting flow. To reduce the cost associated with stiff finite-rate chemistry, the reaction integration uses specialized chemistry treatment along with GPU-oriented acceleration strategies, including matrix-based formulations of chemical source-term evaluations designed to improve the performance of detailed kinetics on modern accelerators [65]. More broadly, the solver uses custom GPU-oriented CUDA implementations within the AMReX framework to accelerate large-scale three-dimensional reacting-flow simulations with strongly disparate spatial and temporal scales, thereby making the present calculations computationally feasible [9].

2.1 Conservation equations

For clarity, the phrase high-fidelity in this dissertation does not imply that every simulation is a uniform-grid DNS. It means that the resolved equations retain compressibility, finite-rate chemistry, differential diffusion, and three-dimensional geometry without replacing the flame by an empirical global reaction or RANS closure. The practical MTM calculations are therefore filtered simulations in an implicit-LES regime. Their grid is selected to resolve

the flame front and the large coherent structures that control stabilization, while smaller turbulent motions are below the local grid filter.

The reacting-flow simulations are based on the compressible Navier–Stokes equations with multi-species transport and finite-rate chemistry. Mass transport is described by the following continuity equation

$$\frac{\partial \rho}{\partial t} + \frac{\partial (\rho u_i)}{\partial x_i} = 0, \tag{2.1}$$

where ρ is the density of the fluid, t is time, x_i and u_i represent the spatial coordinate and the velocity component in the i^{th} direction. The momentum transport is given by

$$\frac{\partial \rho u_i}{\partial t} + \frac{\partial \rho u_i u_j}{\partial x_j} = -\frac{\partial p}{\partial x_i} + \frac{\partial \tau_{ij}}{\partial x_j}, \tag{2.2}$$

where p is the fluid pressure, and τ_{ij} is the viscous stress tensor, given by

$$\tau_{ij} = -\frac{2}{3}\mu \frac{\partial u_k}{\partial x_k}\delta_{ij} + \mu\left(\frac{\partial u_j}{\partial x_i} + \frac{\partial u_i}{\partial x_j}\right), \tag{2.3}$$

where μ is the dynamic viscosity evaluated from a tabulated temperature fit over the solution of collision integrals [66]. The total chemical energy transport is governed by the following equation:

$$e = \int_{T_0}^{T} C_P dT - \frac{p}{\rho} + \sum_{k=1}^{N_s} \Delta h^0_{f,k} Y_k + \frac{1}{2} u_i u_i. \tag{2.4}$$

In Eq. 2.4, T_0 is the reference temperature (typically 298.15 K), T and C_p are the mixture temperature and the mixture specific heat, Y_k and $\Delta h^0_{f,k}$ are the mass fraction and enthalpy of formation for the *kth* species, and N_s is the total number of species in the mixture. The transport of the total chemical energy e is given by:

$$\frac{\partial \rho e}{\partial t} + \frac{\partial u_j \rho h}{\partial x_j} = \frac{\partial}{\partial x_j}\alpha \frac{\partial T}{\partial x_j} + \frac{\partial (u_i \tau_{ij})}{\partial x_j} + \sum_{k=1}^{N} \left(h_k \frac{\partial}{\partial x_i} \left(\rho V_{k,i} Y_k \right) \right), \quad k \in [1, N_s], \tag{2.5}$$

where $h = e + p/\rho$ is the total enthalpy of the mixture (sensible, chemical, and kinetic), and α is the mixture's thermal conductivity. The enthalpy and internal energy are computed relative to this minimum bounding temperature using the fixed specific heat. The gas is treated as an ideal gas, and the governing equations are thus closed using an ideal gas equation of state. The viscosity and thermal conductivity for each species are fit as a function of temperature and pressure to reduce computational cost [66]. Finally, the transport equation

for a species Y_k is given by:

$$\frac{\partial \rho Y_k}{\partial t} + \frac{\partial \rho u_i Y_k}{\partial x_i} = -\frac{\partial}{\partial x_i}(\rho V_{k,i} Y_k) + \dot{\omega}_k, \quad k \in [1, N_s] \tag{2.6}$$

The differential diffusion effects are modeled in this solver through diffusion velocity to account for the fast diffusion of hydrogen and hydrogen-related radicals. The diffusion velocities can be modeled using various methods, including the mixture-averaged diffusion model and the multicomponent diffusion model. According to the findings presented by Bruno et al. [67], both models produce comparable predictions of fluid-dynamic and thermochemical fields when applied to partially premixed hydrogen jet flames at high Reynolds numbers. However, the mixture-averaged diffusion model distinguishes itself by accommodating variable species diffusivity depending on the composition of the mixture, thus addressing the differential diffusion effects. Such effects contrast with preferential diffusion, where the diffusivity of individual species remains constant regardless of the composition of the mixture. In the context of current research, where species composition undergoes significant changes due to chemical reactions, the resulting variability in mixture composition requires accounting for differential diffusion effects for accurate predictions. After assessing the balance between computational effort and numerical accuracy, we selected the mixture-averaged diffusion model as the most suitable method for this investigation. The mixture-averaged diffusion model uses the mass-based mixture-averaged diffusion coefficients matrix, defined as [68]:

$$\frac{1}{D_{km}} = \sum_{j \neq k} \frac{X_j}{D_{kj}} + \frac{X_k}{1 - Y_k} \sum_{j \neq k} \frac{Y_j}{D_{kj}}, \tag{2.7}$$

where D_{kj} is the binary diffusion coefficient matrix. Then the diffusion velocity, $V_{k,i}$ used in Eq. (2.5) and Eq. (2.6) is defined as follows:

$$V_{k,i} = V_{k,i}^D + V_{k,i}^C = -\frac{1}{Y_k} D_{km} \frac{\partial Y_k}{\partial x_i} + \sum_{k=1}^{N} D_{km} \frac{\partial Y_k}{\partial x_i}, \tag{2.8}$$

Due to the modeling of diffusion velocity, the correction velocity, $V_{k,i}^C$, was necessary to ensure that $\sum_{k=1}^{N} V_{i,k} \frac{\partial Y_k}{\partial x_i} = 0$.

Chemical source terms are modeled using detailed finite-rate chemical kinetics. For a mechanism with N_s species and N_r elementary reactions, the net production rate of species k is obtained by summing the contributions of all forward and backward reaction steps.

$$\dot{\omega}_k = \sum_{l=1}^{N_r} M_k \left(\nu''_{k,l} - \nu'_{k,l}\right) \left(R_{f,l} - R_{b,l}\right), \tag{2.9}$$

where M_k is the molecular weight of species k, $\nu'_{k,l}$ and $\nu''_{k,l}$ are the reactant and product stoichiometric coefficients, and $R_{f,l}$ and $R_{b,l}$ are the forward and backward rates for reaction l. The forward rates are evaluated using Arrhenius expressions, while the reverse rates are obtained from the corresponding equilibrium relations.

To reduce this cost, the present solver uses the matrix-based chemistry formulation developed by Barwey and Raman [65], in which the evaluation of detailed chemical source terms is recast into a sequence of dense matrix operations that map efficiently to GPU hardware. This formulation substantially accelerates chemistry integration in large three-dimensional reacting-flow calculations while retaining the underlying detailed kinetic description [65; 9]. Because chemical timescales are much shorter than the characteristic transport timescales, the solver advances reactions and fluid transport with an operator-splitting approach [69; 70], allowing the stiff chemistry update to be treated separately from the convective and diffusive evolution.

Thermochemical properties are obtained from the NASA polynomial representation, which is used to evaluate species heat capacities, enthalpies, and internal energies. This provides a consistent thermodynamic closure for the multi-species reacting system and allows the mixture properties to be assembled directly from the species states. To broaden the temperature range over which the thermodynamic model remains well behaved and to avoid nonphysical behavior at low temperatures, the present solver applies a modified temperature treatment: below a prescribed minimum temperature $T_{\min}$, the species heat capacity is held at its value at $T_{\min}$, and the species enthalpy is evaluated relative to a reference state defined at the same temperature. The internal energy is then obtained from the corresponding enthalpy relation. This treatment preserves smooth and physically reasonable thermodynamic behavior in under-expanded or strongly cooled regions without changing the standard NASA-polynomial form in its normal range of validity [71].

A finite volume formulation is used to discretize the governing equations. Denoting the conserved variables $\mathbf{U}$, fluxes $\mathbf{F}$, and source terms $\mathbf{S}$, the governing equations can be formulated in a generalized form as

$$\frac{\partial \mathbf{U}}{\partial t} + \frac{\partial \mathbf{F}}{\partial x_j} = \frac{\partial \mathbf{S}}{\partial x_j}, \tag{2.10}$$

where $\mathbf{U} = [\rho, \rho u_j, \rho e, \rho Y_k]$ are the conserved variables, $\mathbf{F}$ is the Euler term, and $\mathbf{S}$ represents the source terms that include bulk viscous dissipation, heat diffusion, viscous shear dissipation, enthalpy diffusion, and species diffusion terms. The governing equations are then integrated over each cell, which is treated as the control volume. Applying the divergence theorem allows the time rate of change of the volume-averaged conserved state $\mathbf{U}$ to

be related to the sum of the fluxes and source terms evaluated on the cell faces:

$$\frac{\partial \mathbf{U}}{\partial t} + \sum_{j}^{N_f} \mathbf{F}_j A_j = \sum_{j}^{N_f} \mathbf{S}_j A_j, \tag{2.11}$$

where A_j is the face area of the jth face over the total faces N_f enclosing a cell volume. The finite volume update procedure then requires the following: (1) convert averaged conserved states to cell-centered primitive states, (2) interpolate primitive cell-centered states to cell face centers, (3) compute the average flux over each face, and (4) update the averaged conserved states with a time integrator.

2.2 Complex Geometry and Embedded boundaries

Both the JICF and MTM configurations considered in this dissertation involve practical injector and tube-bundle geometries that cannot be conveniently represented using body-fitted structured meshes. To accommodate these complex internal surfaces, the present solver employs an embedded-boundary formulation on Cartesian grids within our in-house compressible reacting-flow framework [72]. For these complex geometries, the mesh generation process is often time-consuming and expensive. Meshing geometries in unstructured grids is more complicated and computationally intensive than in Cartesian grids due to their irregular and adaptive nature. Embedded boundary Cartesian grids vastly simplify the grid generation process by reducing it to computing intersections of the geometry with the underlying nonaligned Cartesian mesh. As a result, the mesh generation process becomes fast and robust in handling geometries of arbitrary complexity. In addition, the meshes are computationally efficient: typically, most of the mesh consists of regular Cartesian cells, with no additional geometric metrics to store [73]. The challenge lies with the cut cells, which are more irregular than unstructured meshes and impose a significant time step restriction for explicit time integration methods. The geometry treatment in the present work is divided into two steps. The first step is the construction of a functional representation of the complex geometry. The second step is mapping the continuous functional representation of the geometry onto the Cartesian mesh at all AMR levels and storing this information in an AMReX-distributed database class. The embedded boundary formulation for the treatment of complex geometries requires a mathematical implicit function that describes the relative position of the point x (cell centers) with respect to the boundary of the geometry Ω. The function takes in the position x as an input argument and returns a positive value at points inside Ω, zero at the boundary of Ω, and negative outside of Ω. The geometries can be constructed using implicit functions or directly from CAD-based representations in the form

of stereolithography (STL) files.

Current framework uses a cut-cell Embedded Boundary (EB) approach [74; 75], enabling the treatment of arbitrary non-mesh conformal geometries. The embedded boundary will 'cut' through cells arbitrarily, resulting in a new face on the interior of the cell and altered cell volume, centroid, and face centroids and areas. AMReX provides the data structures representing the cut-cell geometry. The cut-cells require special EB treatment to enforce the desired boundary conditions. In particular, we must impose a new flux on the EB face, and the cut-face fluxes are modified according to their shifted centroid and area. This implementation interpolates the cut-face state to the shifted centroid before calculating the fluxes. Thus, it ensures that the wave speeds in the HLLC flux calculation use the face information at the corrected location.

While the EB implementation described above is sufficient to represent non-mesh conformal geometries, it suffers from a CFL constraint proportional to $1/\kappa_V$, where κ_V is the volume fraction of the cut-cell. This CFL constraint is also known as the small cell problem and is prohibitive in complex geometries with cells where $\kappa_V \ll 1$. To alleviate the small cell problem, state redistribution [76; 77] is implemented in the solver through AMReX-Hydro [78]. In state redistribution, cut-cells beneath a target threshold volume fraction redistribute the fluid state to neighboring cells in their merging neighborhood. The desired target volume fraction, with a default of 0.5, determines the merging neighborhood. This eliminates the dependence of the CFL number on the volume fraction.

State redistribution has been successfully applied in compressible flows [76; 77], but in its current form, it suffers from challenges of boundedness in the transport of passive scalars. This arises from distributing the merged neighborhood solution to the computational cells using a least squares limited reconstruction. The boundedness problem is thus analogous to the boundedness problem in flux evaluation, in which face variables are reconstructed from cell values. Previous work addressing boundedness errors within flux evaluation includes [79; 80], which is applied to state redistribution as described below. The primary source of error in state redistribution is the limited least squares reconstruction of the conserved variables. Reconstructing mass, ρ, and species mass, ρY_i, separately results in $\sum \rho Y_i \neq \rho$, guaranteeing a non-physical species mass fraction. A simple second-order accurate solution is to reconstruct the mass, ρ, and mass fractions, Y_i, separately; this will give the sum of the mass fractions to be 1. However, to maintain the boundedness of individual mass fractions, the smallest limiter among all species must be uniformly applied to the reconstruction of all the species mass fractions. These modifications to ensure species boundedness are implemented in the current solver.

2.3 Characteristic boundary conditions for reacting flows

High subsonic turbulent hydrogen combustion analysis requires a compressible solver to couple pressure and density due to the high subsonic flow speed and density variations from reactions. Because of this coupling between pressure and density, the treatment of inlet and outlet boundaries must remain consistent with the characteristic structure of the governing equations. Otherwise, spurious pressure waves can reflect back into the domain and contaminate the interior flame and flow response. The present solver therefore employs a NSCBC treatment following previous work [81], based on the characteristic framework of Poinsot and Lele [62]. It presents a characteristic boundary treatment, an extension of the original NSCBC method proposed by [82]. The current implementation is for AMR-based codes that utilize the embedded boundaries (EB) formulation for complex geometry treatment. We also extended the previous implementations by [83; 84; 85] to include more boundary ghost cells and species treatment for the AMReX framework with EB, respectively. The NSCBC formulation is directly based on primitive variables; the non-conservative formulation of the NS equations can be shown as follows:

$$\frac{\partial \rho}{\partial t} + u_i \frac{\partial \rho}{\partial x_i} + \rho \frac{\partial u_i}{\partial x_i} = 0, \tag{2.12}$$

$$\frac{\partial u_j}{\partial t} + u_i \frac{\partial u_j}{\partial x_i} + \frac{1}{\rho} \frac{\partial p}{\partial x_i} = \frac{1}{\rho} \frac{\partial \tau_{ij}}{\partial x_i}, \tag{2.13}$$

$$\frac{\partial p}{\partial t} + \rho c^2 \frac{\partial u_i}{\partial x_i} + u_i \frac{\partial p}{\partial x_i} = (\gamma - 1) \left(\tau_{ij} \frac{\partial u_j}{\partial x_i} - \frac{\partial q_i}{\partial x_i} + \sum_{k=1}^{k} h_k \frac{\partial}{\partial x_i} \left(\rho D \frac{\partial Y_k}{\partial x_i} \right) \right), \quad k \in [1, N_s], \tag{2.14}$$

$$\frac{\partial Y_k}{\partial t} + u_i \frac{\partial Y_k}{\partial x_i} = \frac{\partial}{\partial x_i} D \frac{\partial Y_k}{\partial x_i} + \frac{1}{\rho} \dot{\omega}_k, \quad k \in [1, N_s]. \tag{2.15}$$

$$\tau_{ij} = \mu \left(\frac{\partial u_i}{\partial x_j} + \frac{\partial u_j}{\partial x_i} - \frac{2}{3} \delta_{ij} \frac{\partial u_k}{\partial x_k} \right),$$

$$q_i = -\lambda \frac{\partial T}{\partial x_i},$$

Using characteristic wave analysis [82] in the x direction, the wave propagation speeds are

$$\lambda_1 = u_1 - c, \quad \lambda_2 = \lambda_3 = \lambda_4 = \lambda_{5+k} = u_1, \quad \lambda_5 = u_1 + c,$$

, and the wave amplitudes are defined as:

$$\mathcal{L}_1 = \lambda_1 \left(\frac{\partial p}{\partial x_1} - \rho c \frac{\partial u_1}{\partial x_1} \right), \tag{2.16}$$

$$\mathcal{L}_2 = \lambda_2 \left(c^2 \frac{\partial \rho}{\partial x_1} - \frac{\partial p}{\partial x_1} \right), \tag{2.17}$$

$$\mathcal{L}_3 = \lambda_3 \frac{\partial u_2}{\partial x_1}, \tag{2.18}$$

$$\mathcal{L}_4 = \lambda_4 \frac{\partial u_3}{\partial x_1}, \tag{2.19}$$

$$\mathcal{L}_5 = \lambda_5 \left(\frac{\partial p}{\partial x_1} + \rho c \frac{\partial u_1}{\partial x_1} \right), \tag{2.20}$$

$$\mathcal{L}_{5+k} = \lambda_{5+k} \frac{\partial Y_k}{\partial x_1}. \tag{2.21}$$

Using these wave amplitudes, the non-conservative NS equations (Eq. 2.12 - 2.15) can be recast as:

$$\frac{\partial \rho}{\partial t} + \frac{1}{c^2} \left(\mathcal{L}_2 + \frac{1}{2} \left(\mathcal{L}_5 + \mathcal{L}_1 \right) \right) = -u_2 \frac{\partial \rho}{\partial x_2} - \rho \frac{\partial u_2}{\partial x_2} - u_3 \frac{\partial \rho}{\partial x_3} - \rho \frac{\partial u_3}{\partial x_3}, \tag{2.22}$$

$$\frac{\partial u_1}{\partial t} + \frac{1}{2\rho c} \left(\mathcal{L}_5 - \mathcal{L}_1 \right) = -u_2 \frac{\partial u_1}{\partial x_2} - u_3 \frac{\partial u_1}{\partial x_3} + \frac{1}{\rho} \frac{\partial \tau_{i1}}{\partial x_i}, \tag{2.23}$$

$$\frac{\partial u_2}{\partial t} + \mathcal{L}_3 = -u_2 \frac{\partial u_2}{\partial x_2} - u_3 \frac{\partial u_2}{\partial x_3} - \frac{1}{\rho} \frac{\partial p}{\partial x_2} + \frac{1}{\rho} \frac{\partial \tau_{i2}}{\partial x_i}, \tag{2.24}$$

$$\frac{\partial u_3}{\partial t} + \mathcal{L}_4 = -u_2 \frac{\partial u_3}{\partial x_2} - u_3 \frac{\partial u_3}{\partial x_3} - \frac{1}{\rho} \frac{\partial p}{\partial x_3} + \frac{1}{\rho} \frac{\partial \tau_{i3}}{\partial x_i}, \tag{2.25}$$

$$\begin{aligned} \frac{\partial p}{\partial t} + \frac{1}{2}(\mathcal{L}_1 + \mathcal{L}_5) = & -\rho c^2 \frac{\partial u_2}{\partial x_2} - u_2 \frac{\partial p}{\partial x_2} - \rho c^2 \frac{\partial u_3}{\partial x_3} - u_3 \frac{\partial p}{\partial x_3}, \\ & + (\gamma - 1) \left(\tau_{ij} \frac{\partial u_j}{\partial x_i} - \frac{\partial q_i}{\partial x_i} + \sum_{k=1}^{k} h_k \frac{\partial}{\partial x_i} \left(\rho D \frac{\partial Y_k}{\partial x_i} \right) \right) \quad k \in [1, N_s], \end{aligned} \tag{2.26}$$

$$\frac{\partial Y_k}{\partial t} + \mathcal{L}_{5+k} = -u_2 \frac{\partial Y_k}{\partial x_2} - u_3 \frac{\partial Y_k}{\partial x_3} + \frac{\partial}{\partial x_i} D \frac{\partial Y_k}{\partial x_i} + \frac{1}{\rho} \dot{\omega}_k \quad k \in [1, N_s]. \tag{2.27}$$

The left-hand side is the Local One-Dimensional Inviscid LODI system [82] with the species transport equation, while the right-hand side represents the diffusion, reaction, and transverse terms, which are referred to as the modified LODI in [84]. In order to clearly define the transverse, diffusion, and reaction terms for each wave amplitude, Eq.(2.22 -

2.27) can be written as:

$$\frac{\partial p}{\partial t} - \rho c \frac{\partial u_1}{\partial t} + \mathcal{L}_1 + \Im_1^{(x)} = \mathcal{D}_1, \tag{2.28}$$

$$c^2 \frac{\partial \rho}{\partial t} - \frac{\partial p}{\partial t} + \mathcal{L}_2 + \Im_2^{(x)} = \mathcal{D}_2, \tag{2.29}$$

$$\frac{\partial u_2}{\partial t} + \mathcal{L}_3 + \Im_3^{(x)} = \mathcal{D}_3, \tag{2.30}$$

$$\frac{\partial u_3}{\partial t} + \mathcal{L}_4 + \Im_4^{(x)} = \mathcal{D}_4, \tag{2.31}$$

$$\frac{\partial p}{\partial t} + \rho c \frac{\partial u_1}{\partial t} + \mathcal{L}_5 + \Im_5^{(x)} = \mathcal{D}_5, \tag{2.32}$$

$$\frac{\partial Y_k}{\partial t} + \mathcal{L}_{5+k} + \Im_{5+k}^{(x)} = \mathcal{D}_{5+k} + \mathcal{R}_{5+k}, \qquad k \in [1, N_s]\,. \tag{2.33}$$

Associating with each wave's amplitude, the transverse term, $\Im_i^{(x)}$ is defined as:

$$\Im_1^{(x)} = \left(u_2 \frac{\partial p}{\partial x_2} + \gamma p \frac{\partial u_2}{\partial x_2} - \rho c u_2 \frac{\partial u_1}{\partial x_2} \right) + \left(u_3 \frac{\partial p}{\partial x_3} + \gamma p \frac{\partial u_3}{\partial x_3} - \rho c u_3 \frac{\partial u_1}{\partial x_3} \right), \tag{2.34}$$

$$\Im_2^{(x)} = u_2 \left(c^2 \frac{\partial \rho}{\partial x_2} - \frac{\partial p}{\partial x_2} \right) + u_3 \left(c^2 \frac{\partial \rho}{\partial u_3} - \frac{\partial p}{\partial x_3} \right), \tag{2.35}$$

$$\Im_3^{(x)} = \left(u_2 \frac{\partial u_2}{\partial x_2} + \frac{1}{\rho} \frac{\partial p}{\partial x_2} \right) + u_3 \frac{\partial u_2}{\partial x_3}, \tag{2.36}$$

$$\Im_4^{(x)} = u_2 \frac{\partial u_3}{\partial x_2} + \left(\frac{1}{\rho} \frac{\partial p}{\partial x_3} + u_3 \frac{\partial u_3}{\partial x_3} \right), \tag{2.37}$$

$$\Im_5^{(x)} = \left(u_2 \frac{\partial p}{\partial x_2} + \gamma p \frac{\partial u_2}{\partial x_2} + \rho c u_2 \frac{\partial u_1}{\partial x_2} \right) + \left(u_3 \frac{\partial p}{\partial x_3} + \gamma p \frac{\partial u_3}{\partial x_3} + \rho c u_3 \frac{\partial u_1}{\partial x_3} \right), \tag{2.38}$$

$$\Im_{5+k}^{(x)} = u_2 \frac{\partial Y_k}{\partial x_2} + u_3 \frac{\partial Y_k}{\partial x_3}, \qquad k \in [1, N_s]\,. \tag{2.39}$$

Diffusion transverse term, $\mathcal{D}_i$ are defined as:

$$\mathcal{D}_1 = (\gamma - 1)\left(\tau_{ij}\frac{\partial u_j}{\partial x_i} - \frac{\partial q_i}{\partial x_i} + \sum_{k=1}^{k} h_k \frac{\partial}{\partial x_i}\left(\rho D \frac{\partial Y_k}{\partial x_i}\right)\right) - c\frac{\partial \tau_{i1}}{\partial x_i}, \tag{2.40}$$

$$\mathcal{D}_2 = -(\gamma - 1)\left(\tau_{ij}\frac{\partial u_j}{\partial x_i} - \frac{\partial q_i}{\partial x_i} + \sum_{k=1}^{k} h_k \frac{\partial}{\partial x_i}\left(\rho D \frac{\partial Y_k}{\partial x_i}\right)\right), \tag{2.41}$$

$$\mathcal{D}_3 = \frac{1}{\rho}\frac{\partial \tau_{i2}}{\partial x_i}, \tag{2.42}$$

$$\mathcal{D}_4 = \frac{1}{\rho}\frac{\partial \tau_{i3}}{\partial x_i}, \tag{2.43}$$

$$\mathcal{D}_5 = (\gamma - 1)\left(\tau_{ij}\frac{\partial u_j}{\partial x_i} - \frac{\partial q_i}{\partial x_i} + \sum_{k=1}^{k} h_k \frac{\partial}{\partial x_i}\left(\rho D \frac{\partial Y_k}{\partial x_i}\right)\right) + c\frac{\partial \tau_{i1}}{\partial x_i}, \tag{2.44}$$

$$\mathcal{D}_{5+k} = \frac{\partial}{\partial x_i} D \frac{\partial Y_k}{\partial x_i}, \qquad k \in [1, N_s]\,. \tag{2.45}$$

The reaction term only appears in species equations Eq. 2.33 where $\mathcal{R}_{5+k} = \frac{1}{\rho}\dot{\omega}_k$. With the temporal integration procedure in the solver, the ghost cell values are updated for each time integration step $(n, n+\frac{1}{2})$, assuming that the ghost cells and the interior cells are in the same timestep. Therefore, the time derivative in Eq.(2.22 - 2.27) can be eliminated naturally. The method of updating the primitive variables of the ghost cells is to express the spatial derivatives of each primitive variable in Eq.(2.22 - 2.27) in terms of the last interior cells and ghost cells using some finite difference scheme [83]. To show the calculation for different cells with compact equations, primitive variables are defined as $\boldsymbol{Q} = [\rho, u, v, w, p]$. The main modification is to extend the formulation for $\frac{\partial \boldsymbol{Q}}{\partial x_1}$ to five ghost cells due to the requirement for the implementation of EB in AMReX. From the LODI system in the x-direction, we can

express $\frac{\partial \boldsymbol{Q}}{\partial x_1}$ in terms of wave amplitudes as:

$$\frac{\partial \boldsymbol{Q}}{\partial x_1} = \begin{bmatrix} \frac{\partial \rho}{\partial x_1} \\ \\ \frac{\partial u_1}{\partial x_1} \\ \\ \frac{\partial u_2}{\partial x_1} \\ \\ \frac{\partial u_3}{\partial x_1} \\ \\ \frac{\partial p}{\partial x_1} \\ \\ \frac{\partial Y_k}{\partial x_1} \end{bmatrix} = \begin{bmatrix} \frac{1}{c^2}\left(\frac{\mathcal{L}_2}{\lambda_2} + \frac{1}{2}\left(\frac{\mathcal{L}_5}{\lambda_5} + \frac{\mathcal{L}_1}{\lambda_1}\right)\right) \\ \\ \frac{1}{2\rho c}\left(\frac{\mathcal{L}_5}{\lambda_5} - \frac{\mathcal{L}_1}{\lambda_1}\right) \\ \\ \frac{\mathcal{L}_3}{\lambda_3} \\ \\ \frac{\mathcal{L}_4}{\lambda_4} \\ \\ \frac{1}{2}\left(\frac{\mathcal{L}_1}{\lambda_1} + \frac{\mathcal{L}_5}{\lambda_5}\right) \\ \\ \frac{\mathcal{L}_{5+k}}{\lambda_{5+k}} \end{bmatrix} \tag{2.46}$$

All ghost cells are expressed in terms of the last interior and other ghost cells using certain finite difference schemes, where the subscript i represents the last interior cell; the expressions for the left boundary ($i = 1$) are as follows:

$$\boldsymbol{Q}_{i-1} = \boldsymbol{Q}_{i+1} - 2\Delta x \frac{\partial \boldsymbol{Q}}{\partial x}, \tag{2.47}$$

$$\boldsymbol{Q}_{i-2} = -2\boldsymbol{Q}_{i+1} - 3\boldsymbol{Q}_i + 6\boldsymbol{Q}_{i-1} + 6\Delta x \frac{\partial \boldsymbol{Q}}{\partial x}, \tag{2.48}$$

$$\boldsymbol{Q}_{i-3} = 3\boldsymbol{Q}_{i+1} + 10\boldsymbol{Q}_i - 18\boldsymbol{Q}_{i-1} + 6\boldsymbol{Q}_{i-2} - 12\Delta x \frac{\partial \boldsymbol{Q}}{\partial x}, \tag{2.49}$$

$$\boldsymbol{Q}_{i-4} = -4\boldsymbol{Q}_{i+1} - \frac{65}{3}\boldsymbol{Q}_i + 40\boldsymbol{Q}_{i-1} - 20\boldsymbol{Q}_{i-2} + \frac{20}{3}\boldsymbol{Q}_{i-3} + 20\Delta x \frac{\partial \boldsymbol{Q}}{\partial x}, \tag{2.50}$$

$$\boldsymbol{Q}_{i-5} = \frac{1}{107}\left(-27\boldsymbol{Q}_{i+1} + 1162\boldsymbol{Q}_i - 2565\boldsymbol{Q}_{i-1} + 2620\boldsymbol{Q}_{i-2} - 1765\boldsymbol{Q}_{i-3} + 682\boldsymbol{Q}_{i-4} - 480\Delta x \frac{\partial \boldsymbol{Q}}{\partial x}\right). \tag{2.51}$$

As mentioned in [83], simple central finite schemes using two stencils only lead to numerical instability. Instead, all available stencils will be used to form a particular scheme for each ghost cell. For the first four ghost cells, the finite difference schemes are derived from the method of undetermined coefficients [86] to obtain the highest order of accuracy possible with the available stencils. In contrast, for the 5^{th} ghost cell, to achieve numerical stability, we use a scheme of zero-order accuracy with $\frac{\partial Q}{\partial x} = \sum_{j=-1}^{r} a_j Q_j = \frac{5}{6}\frac{\partial Q}{\partial x} + \frac{1}{4}\Delta x \frac{\partial^2 Q}{\partial x^2} + O\left(\Delta x^2\right)$.

For the right boundary (i = L_x), expressions can be shown as:

$$\boldsymbol{Q}_{i+1} = \boldsymbol{Q}_{i-1} + 2\Delta x \frac{\partial \boldsymbol{Q}}{\partial x}, \tag{2.52}$$

$$\boldsymbol{Q}_{i+2} = -2\boldsymbol{Q}_{i-1} - 3\boldsymbol{Q}_i + 6\boldsymbol{Q}_{i+1} - 6\Delta x \frac{\partial \boldsymbol{Q}}{\partial x}, \tag{2.53}$$

$$\boldsymbol{Q}_{i+3} = 3\boldsymbol{Q}_{i-1} + 10\boldsymbol{Q}_i - 18\boldsymbol{Q}_{i+1} + 6\boldsymbol{Q}_{i+2} + 12\Delta x \frac{\partial \boldsymbol{Q}}{\partial x}, \tag{2.54}$$

$$\boldsymbol{Q}_{i+4} = -4\boldsymbol{Q}_{i-1} - \frac{65}{3}\boldsymbol{Q}_i + 40\boldsymbol{Q}_{i+1} - 20\boldsymbol{Q}_{i+2} + \frac{20}{3}\boldsymbol{Q}_{i+3} - 20\Delta x \frac{\partial \boldsymbol{Q}}{\partial x}, \tag{2.55}$$

$$\boldsymbol{Q}_{i+5} = \frac{1}{107}\left(-27\boldsymbol{Q}_{i-1} + 1162\boldsymbol{Q}_i - 2565\boldsymbol{Q}_{i+1} + 2620\boldsymbol{Q}_{i+2} - 1765\boldsymbol{Q}_{i+3} + 682\boldsymbol{Q}_{i+4} + 480\Delta x \frac{\partial \boldsymbol{Q}}{\partial x}\right). \tag{2.56}$$

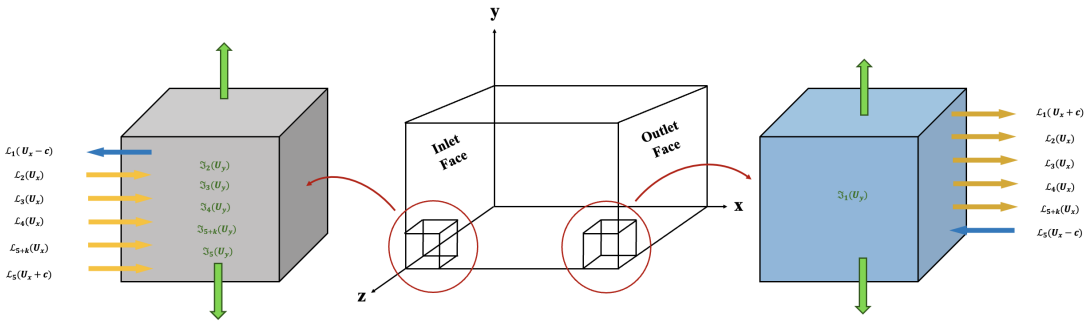


Figure 2.2: Computational domain showing the waves entering and leaving through inlet and outlet.

For outgoing waves, the wave amplitudes can be directly calculated from definitions in Eq.(2.16 - 2.21); the ghost cell values are updated from Eq.(2.47 - 2.56). It is noteworthy that the amplitudes of outgoing waves can be directly obtained from the LODI equations, excluding transverse and diffusion effects, since they do not induce artificial waves entering the domain that might alter the internal solution. In contrast, incoming waves do generate such spurious waves, necessitating the incorporation of transverse and diffusion terms in the amplitude calculations, along with the target value treatment [87]. For example, for outflow at $x = L_x$, only $\mathcal{L}_5$ is an incoming wave, as shown in Fig. 2.2; it was originally defined as $\mathcal{L}_5 = K\left(p - p_t\right)$ without any consideration of the transverse and diffusion terms. When substituting this expression for $\mathcal{L}_5$ into Eq.(2.32), the result will be expressed as:

$$\frac{\partial p}{\partial t} + \rho c \frac{\partial u_1}{\partial t} + K\left(p - p_t\right) + \Im_5^{(x)} = \mathcal{D}_5. \tag{2.57}$$

From this equation, at steady state ($\frac{\partial}{\partial t} = 0$), it leads to $K\left(p - p_t\right) + \Im_5^{(x)} = \mathcal{D}_5^{(x)}$. This implies that pressure $p = \frac{\mathcal{D}_5 - \Im_5^{(x)}}{K} + p_t$ will not reach the target pressure p_t, resulting in pressure drifting. Including transverse and diffusion terms, $\mathcal{L}_5 = K\left(p - p_t\right) - \Im_5^{(x)} + \mathcal{D}_5^{(x)}$, will lead to $K\left(p - p_t\right) = 0$ at steady state. However, the transverse term leads to numerical

instability when the mean flow direction does not dominate over the transverse direction near the boundary layer. Therefore, a relaxation term defined as χ for the transverse term is needed [84]. In the current implementation, diffusion and reaction terms are ignored in the wave amplitudes approximation, while the transverse term is considered, as it is expected to dominate over the diffusion terms, and reactions do not appear at the inflow region in the case of interest. In the subsequent section, we present the formulation for flow along the x_1-direction (inflow ($x = 0$) and outflow ($x = L_x$) formulations). Although the formulation for the x_2 and x_3 directions is not included, it is similar in structure and can be readily extrapolated.

For subsonic inflow, there is one outgoing wave; all other waves are incoming waves, as shown in Fig. 2.2. The amplitude of incoming waves with transverse terms can be expressed as [85], [83]:

$$\mathcal{L}_2 = \eta_2 \frac{\rho c \mathcal{R}}{L_x} (T - T_t) - \Im_2^{(x)}, \tag{2.58}$$

$$\mathcal{L}_3 = \eta_3 \frac{c}{L_x} (v - v_t) - \Im_3^{(x)}, \tag{2.59}$$

$$\mathcal{L}_4 = \eta_4 \frac{c}{L_x} (w - w_t) - \Im_4^{(x)}, \tag{2.60}$$

$$\mathcal{L}_5 = \eta_5 \frac{\rho c^2 (1 - M^2)}{L_x} (u - u_t) - \Im_5^{(x)}, \tag{2.61}$$

$$\mathcal{L}_{5+k} = \eta_{5+k} \frac{c}{L_x} (Y_k - Y_{k_t}) - \Im_5^{(x)}. \tag{2.62}$$

The outgoing wave will be calculated directly from Eq.(2.16). For derivatives in the x_1 direction, a one-sided finite difference scheme needs to be used for any scalar ϕ ($x = 0$):

$$\frac{\partial \phi}{\partial x_1} = \frac{-3\phi_i + 4\phi_{i+1} - \phi_{i+2}}{2\Delta x}. \tag{2.63}$$

The transverse terms are defined by Eq.(2.35 - 2.39). To calculate these transverse terms, a simple central finite difference method can be applied to derivatives in the x_2 and x_3 directions. Near the corner of the EB wall and the inflow, a one-sided finite difference method was used. Previous work [88; 89] considered an additional unsteady term $\frac{\partial u_i^{'}}{\partial t}$ for the wave amplitude calculations in vortical and acoustic flow. In the current work, as described for Eq.(2.22 - 2.27), the time derivative vanishes for $\frac{\partial u_i}{\partial t}$; therefore, this time derivative term of unsteady fluctuation was ignored.

For subsonic outflow, in contrast to inflow, there is only one incoming wave and all other waves are outgoing waves, as shown in Fig. 2.2. The amplitudes of the incoming wave along

with transverse terms can be expressed as [85], [83] :

$$\mathcal{L}_5 = \frac{\sigma c\,(1-M^2)}{L_x}\,(p-p_t) - (1-\chi)\Im_5^{(x)}. \tag{2.64}$$

The outgoing wave will be calculated directly from Eq.(2.16 - 2.19 and 2.21). For derivatives in the x_1 direction, a one-sided finite difference scheme must be used for any scalar ϕ ($x = L_x$):

$$\frac{\partial \phi}{\partial x_1} = \frac{3\phi_i - 4\phi_{i+1} + \phi_{i+2}}{2\Delta x}. \tag{2.65}$$

The transverse terms are defined by Eq.(2.38). In order to calculate these transverse terms, a simple central finite difference method can be applied for derivatives in the x_2 and x_3 directions. At the corner of the EB wall and the outflow, a similar one-sided finite-difference method is used. Based on previous work [82; 90], an initial optimal value of 0.25 will be used for σ. Following the idea proposed in [85], the value of χ is set as a local Mach number or some constant averaged Mach number. However, these parameters are highly case-dependent and require further tuning.

In reactive flow simulations, the reaction induces significant temperature and species gradients that result in density gradients and vortical flow near the outlet boundary. When a transverse term is incorporated in $\mathcal{L}_1$ with χ as the local Mach number, the solution diverges due to the mean flow direction gradients not being dominant over the transverse term under such conditions. The solution involved tuning the value of χ to control the transverse term $\mathcal{T}_1$ in $\mathcal{L}_1$ in the outflow equations after the reactions, combined with damping the fluctuations by coarsening the mesh and decreasing the value of σ.

In this numerical implementation, the boundary update is constructed by solving the LODI system within the ghost-cell region using approximated characteristic amplitudes, along with a relaxation-based boundary treatment. The outgoing characteristic information is taken from the interior solution, while the incoming characteristic information is determined from prescribed target boundary states. In this way, the boundary treatment remains consistent with the direction of wave propagation and avoids imposing nonphysical information on characteristics that should leave the domain. Once the characteristic update is obtained, the primitive variables in the ghost cells are reconstructed from the updated LODI relations. The ghost-cell values are therefore not imposed directly as fixed primitive states; instead, they are inferred from the local characteristic evolution implied by the boundary treatment. The relaxation parameters control how strongly the boundary state is driven toward its prescribed target values. At the inflow, the parameters η_i set the relaxation strength for the incoming thermodynamic, velocity, and species characteristics

and therefore determine how rapidly the boundary state approaches the desired inflow condition. At the outflow, the parameter σ controls the strength of the pressure relaxation and thus how strongly the outlet pressure is enforced, while χ modulates the contribution of the transverse correction terms in the outflow treatment. These parameters must be chosen to balance accurate boundary enforcement against excessive acoustic reflection or numerical stiffness. In practice, overly weak relaxation can allow boundary drift, whereas overly strong relaxation can introduce spurious feedback into the computational domain. This procedure is important for maintaining compatibility with the compressible finite-volume solver, since it provides ghost-cell states that are consistent with both the interior solution and the prescribed boundary behavior. As discussed in previous works [81], retaining the transverse corrections in this reconstruction is particularly important in high-subsonic multidimensional reacting flows, where pressure drift and spurious wave reflection can otherwise become significant.

2.4 GPU-Oriented Implementation

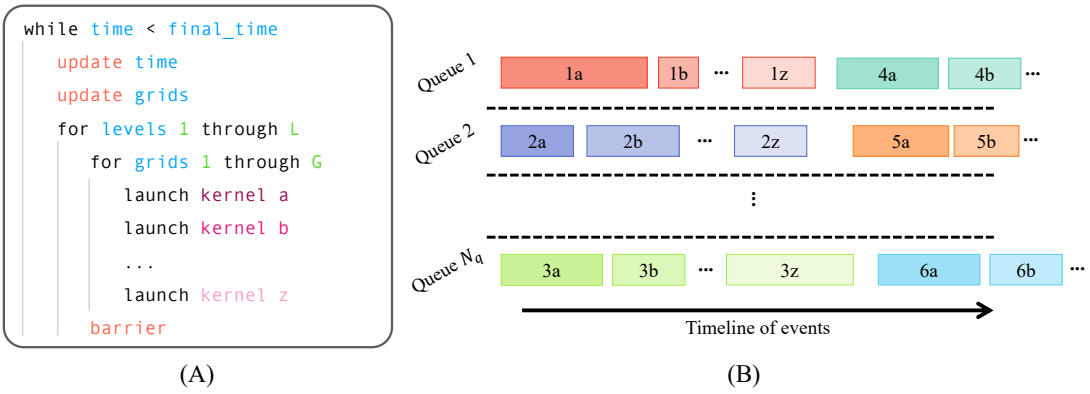


Figure 2.3: Illustration of GPU-oriented execution strategies for AMReX-based reacting-flow solvers, highlighting how mesh, physics, and chemistry kernels are organized for accelerator performance [9].

The substantial computational cost of multiscale, three-dimensional compressible reacting-flow simulation is further addressed in the present solver through a GPU-oriented implementation within the AMReX framework, using custom CUDA kernels and execution strategies designed specifically for this class of calculations [9]. The main performance challenges arise from the combined effects of memory-access efficiency, localized chemistry cost, and the nonuniform workload associated with adaptive mesh refinement. The implementation is therefore organized to target these issues directly through data-layout optimization,

chemistry-specific execution strategies, and AMR-aware load management.

Figure 2.3 summarizes the overall organization of the GPU implementation. Rather than treating the solver update as a single monolithic operation, the major algorithmic components—including hydrodynamic updates, chemistry evaluation, and mesh-management operations—are decomposed into fine-grained kernels that are launched across the active AMR hierarchy. This structure exposes concurrency across grid patches and refinement levels while preserving the distinct performance requirements of the major solver components. In practice, the execution model relies on many kernel launches and asynchronous work queues so that operations with different memory and arithmetic characteristics can be scheduled efficiently on the accelerator. This organization is especially important for reacting-flow calculations, where chemistry is highly localized and significantly more expensive per cell than the hydrodynamic update.

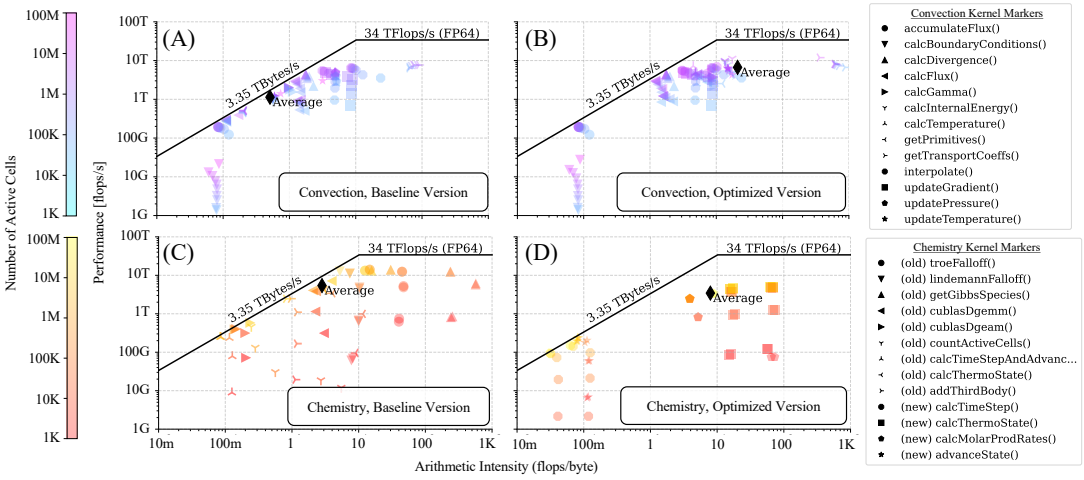


Figure 2.4: Roofline analysis comparing baseline and optimized convection and chemistry kernels, showing improved performance and hardware utilization in the GPU-oriented solver implementation [9].

The performance implications of this design are illustrated by the roofline analysis in Fig. 2.4. The figure compares baseline and optimized implementations for both convection and chemistry kernels. In both cases, the optimized kernels achieve higher sustained performance and move toward more favorable arithmetic intensity, indicating improved utilization of the underlying GPU hardware. The improvement is particularly significant for chemistry, which remains one of the dominant costs in high-fidelity reacting-flow simulation. These optimizations produce substantial overall speedup relative to the initial implementation and demonstrate that meaningful gains require coordinated improvement of the major solver components rather than isolated optimization of a single kernel. Overall, the GPU-

oriented implementation achieves its performance gains through coordinated improvements in memory access efficiency, chemistry-kernel execution, and the scheduling of AMR workloads across the GPU. Additional details of the GPU-oriented implementation, including the execution strategy and performance analysis, are presented in [9].

CHAPTER 3

Fluid-Chemistry Interactions and Modeling Challenges in Hydrogen Jets in Crossflow

3.1 Introduction

Numerical study of turbulent hydrogen combustion remains demanding even in canonical configurations. Thin reaction zones, strong local strain, finite-rate chemistry, and differential diffusion all interact with three-dimensional turbulent transport, so the flame response cannot be inferred from the large-scale flow field alone [91; 32]. Reduced-order combustion models remain attractive for Large-Eddy Simulation (LES) because they offer a practical route to turbulent reacting-flow calculations at tractable cost, and flamelet-based approaches continue to be among the most widely used formulations in this setting [92; 93; 94; 95]. Their use in hydrogen flames, however, remains more delicate. The strong diffusivity of hydrogen and the resulting sensitivity to local transport can move the flame away from the assumptions embedded in tabulated manifolds, especially when multiple burning modes and strongly non-uniform stabilization environments coexist [96; 97].

The reacting jet in crossflow retains these modeling difficulties in a flow configuration that remains physically compact and well characterized. Despite its simpler geometry, it retains features that are central to hydrogen combustion in more complex systems: strong shear between dissimilar streams, inherently three-dimensional vortex dynamics, wake recirculation, local extinction and re-ignition tendencies, and multiple candidate flame-stabilization pathways [12; 98; 29; 99]. The broader relevance of JICF to combustor and flare applications is also evident in prior work. Some works investigated reacting transverse hydrogen jets in high-enthalpy supersonic crossflow, showing that the jet-to-crossflow momentum-flux ratio reorganizes ignition, near-wall burning, and shear-layer reaction structure over $J = 0.3$–5.0 [100; 31]; subsequent staged-transverse-jet work showed that a downstream pulsed-detonation jet can reorganize the wake and increase cumulative heat release [101]. While other works treated non-assist flare flames as reacting JICF configurations, explicitly linking

crosswind turbulence to local strain, scalar dissipation, flame detachment, and degraded combustion efficiency; in that methane-flare study, combustion efficiency dropped by about 10% as crossflow turbulence intensity approached 20% [102]. A companion experimental/LES study of utility-pipe flares showed that crosswind speed can reduce measured combustion efficiency from nearly 100% at 0.3 m/s to 80.2% at 10 m/s for natural gas, while LES with 3–12 m/s crosswinds yielded combustion efficiencies from 99.45% to 95.89% [103]. Although the fuels and Mach numbers differ from the present hydrogen cases, these studies support the same physical point: jet momentum, crossflow turbulence, recirculation, and strain determine whether a transverse reacting jet remains attached, lifts, locally extinguishes, or shifts its dominant heat-release pathway. Related high-fidelity simulations by Sharma et al. [104] showed that a hydrogen jet in high-speed crossflow can contain simultaneous windward flamelet-like reaction, lee-side distributed reaction, and counter-rotating-vortex-driven jet-core breakdown. These same ingredients appear in staged and distributed combustors, where fuel jets interact with hot crossflow gases and where the location of flame anchoring is closely tied to operability and safety. In hydrogen-fueled configurations, the jet in crossflow is therefore not only a canonical turbulent flame problem but also a compact representation of the coupled flow-transport-chemistry interactions that appear more broadly in practical combustors.

For gas-turbine design, the relevance of this configuration is most direct when it is interpreted as a controlled representation of staged fuel injection, dilution-jet interaction, and transverse fuel addition into a hot main stream. The important design variables are therefore not only geometric, but nondimensional: the momentum-flux ratio J, the jet and crossflow Reynolds numbers Re_j and Re_c, the fuel density ratio, the hydrogen volume fraction, the stoichiometric mixture fraction Z_{st}, and the scalar-dissipation and strain fields near the flame edge. In the present study, these quantities span $J = 1.96$–8.41, $Re_j = 2600$–6000, $Re_c = 4.4 \times 10^4$, and hydrogen contents of 70–95% by volume. This range is used to connect the canonical jet-in-crossflow flame to a combustor-design question: which branch of the flame is robustly stabilized, and which branch is more susceptible to extinction, re-ignition, or upstream propagation under hydrogen-enriched operation?

A range of combustion-modeling strategies has been applied to reacting jets in crossflow. High-fidelity simulations and experiments have clarified many aspects of flame structure and stabilization [98; 12; 105; 99], while flamelet-generated manifold approaches remain attractive in LES due to their efficiency and their ability to represent turbulence-chemistry interaction in a reduced form [92; 93; 94; 95]. Their performance in hydrogen-rich jets, however, depends on how well the model captures the local burning mode and the transport processes that feed the reaction zone. Recent work on high-speed hydrogen jets in crossflow has shown that

strain-sensitive flamelet formulations improve the representation of the large-scale flame organization, but it also leaves open the question of how differential diffusion and detailed chemistry alter the local stabilization behavior [10].

Differential diffusion is particularly important in this context. Its influence has long been recognized in flamelet theory [96; 97], and subsequent studies have shown that it can substantially modify local flame structure in hydrogen-rich reacting flows, including turbulent non-premixed flames and hydrogen-containing ignition kernels [106; 107; 108]. In jets in crossflow, its impact is not expected to be uniform throughout the flame. Regions dominated by strong shear and turbulent mixing need not respond in the same way as low-speed recirculation zones, where molecular transport can more directly alter the local mixture encountered by the flame [109; 110]. This makes the jet in crossflow a useful configuration for separating where reduced-order combustion models remain adequate and where higher-fidelity treatment of chemistry and transport becomes necessary.

The discussion that follows examines these issues through a combined view of flame structure, local stabilization behavior, and thermochemical organization in hydrogen jets in crossflow. Particular attention is given to the comparison between experimental measurements [12] and numerical predictions, including both a strain-sensitive flamelet LES description and a higher-fidelity detailed-chemistry simulation, in order to assess model performance along with the underlying flame physics. The influence of differential diffusion is then examined across the different branches of the flame and their associated transport environments, yielding a more complete interpretation of hydrogen flame stabilization in crossflow.

The resolution regime in this chapter is therefore mixed by design. The strain-sensitive manifold calculation is an explicit LES closure for the filtered reacting flow, whereas the detailed AMReX calculation is interpreted as an implicit LES/resolved-large-eddy finite-rate simulation with no explicit subgrid turbulence model. In this regime, AMR resolves the flame-front region, the jet shear layer, the wake recirculation, and the large coherent vortices that organize the lee and lifted branches, while sub-filter turbulent motions remain represented by the numerical dissipation of the finite-volume scheme. Where DNS terminology is retained in figure labels or model-comparison discussion, it should be read as the high-resolution detailed-chemistry reference for this compact laboratory configuration, not as a claim that the practical gas-turbine-scale problem is fully resolved down to all Kolmogorov scales.

3.2 Configuration and Modeling Approach

The reacting configuration consists of a round fuel jet injected normally into a hot crossflow. The principal control parameter is the jet-to-crossflow momentum-flux ratio.

$$J = \frac{\rho_j U_j^2}{\rho_c U_c^2}, \tag{3.1}$$

where ρ_j and U_j denote the jet density and velocity, and ρ_c and U_c are the corresponding crossflow quantities. This parameter controls the balance between jet penetration and crossflow deflection and, therefore, strongly influences the large-scale flame topology. Prior reacting-transverse-jet measurements have shown that J can separate distinct near-wall and shear-layer burning regimes, including low-J lifted/wake-stabilized behavior and high-J upstream-recirculation/shear-layer burning in high-speed hydrogen crossflow flames [31]. In the present subsonic hot-crossflow cases, increasing J from 1.96 to 8.41 similarly moves the controlling stabilization environment away from a compact lee-side branch and toward a stronger lifted/shear-layer branch, although the absolute regime differs from the supersonic configuration. The cases follow the hydrogen jet-flame measurements of Steinberg et al. [12]. In the reference configurations, a hydrogen-nitrogen jet issues perpendicularly into a hot air crossflow, and the resulting flame morphology is compared against the measured branch location and mean flame contour. Additional hydrogen-enriched cases are also considered in order to examine how increased hydrogen content by volume modifies the local transport and stabilization behavior. The cases used in the present analysis are summarized in Table 3.1. Cases A7 and C7 correspond directly to the experimental conditions, while Cases A9 and C9 extend the configuration to higher hydrogen content by volume for analysis of differential-diffusion effects.

Table 3.1: Cases considered in the hydrogen jet-in-crossflow study. Cases A7 and C7 correspond to the experimental configurations of Steinberg et al. [12], while Cases A9 and C9 are hydrogen-enriched numerical extensions.

Case	H_2 Fuel (vol.%)	J	U_j (m/s)	Re_j	U_c (m/s)	Re_c	Exp.
A7	70	1.96	100	3000	55	44000	✓
C7	70	8.41	200	6000	55	44000	✓
A9	95	1.96	171	2600	55	44000	–
C9	95	8.41	342	5200	55	44000	–

Throughout this chapter, Z denotes the Bilger mixture fraction, a conserved-scalar measure constructed from elemental mass fractions so that $Z = 0$ corresponds to the oxidizer stream and $Z = 1$ corresponds to the fuel stream; this definition provides a common mixture coordinate for comparing partially premixed and non-premixed hydrogen flame states [111]. For the present 70% hydrogen-by-volume reference cases, the stoichiometric value is approximately $Z_{st} = 0.17$, which is used below to interpret flame-edge statistics and laminar-reference comparisons.

The computational domain is shown in Fig. 3.1. A circular injector with a diameter of $D_j = 2$ mm is mounted on the lower wall of a rectangular domain with dimensions $80 \times 40 \times 60$ mm^3 in the streamwise, spanwise, and vertical directions, respectively. The fuel jet issues normally from the wall into a crossflow entering from upstream. This arrangement generates the characteristic jet bending, upper-shear-layer roll-up, and lee-side wake recirculation associated with flame stabilization in crossflow. Although the geometry is simple, the reacting structures remain highly localized near the injector and in the downstream reaction zone. The mesh is therefore refined dynamically in the vicinity of the flame front and the surrounding vortical structures.

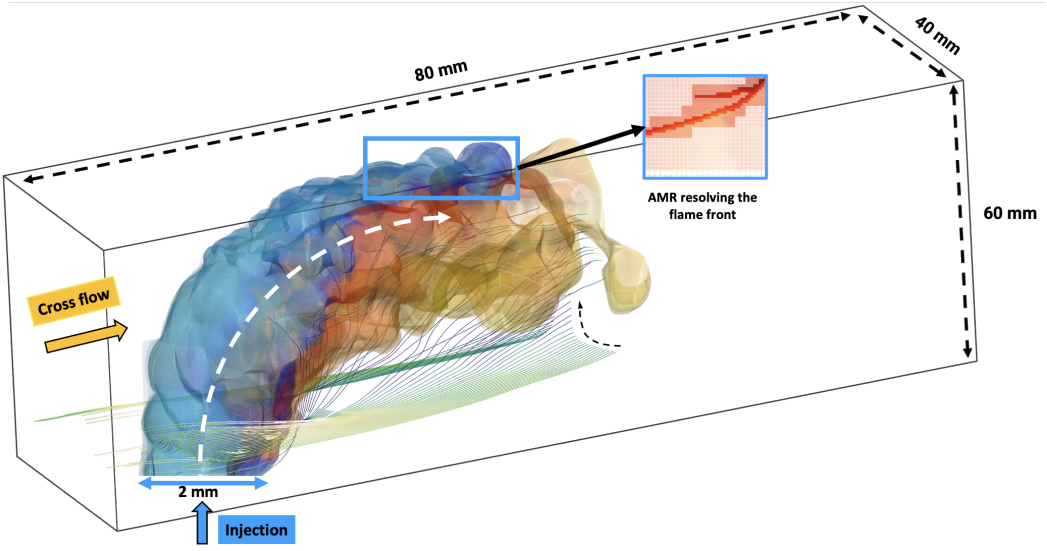


Figure 3.1: Computational domain with major dimensions and injector-region mesh view. The hydrogen jet issues normally from a 2 mm injector into a hot crossflow, while mesh refinement is concentrated near the flame front and other localized reacting structures.

Two numerical descriptions are considered for this configuration. One is a LES using a strain-sensitive flamelet-generated manifold combustion model. The other is a highly resolved finite-volume simulation with detailed finite-rate chemistry and differential diffusion. The experimental comparison provides a reference for mean flame morphology, while the

two numerical approaches provide complementary descriptions of the same reacting flow at different modeling fidelity.

3.2.0.1 Large-Eddy Simulation with S-FGM

The LES employs a low-Mach-number reacting-flow solver coupled with tabulated chemistry. The solver is formulated to retain second-order spatial and temporal accuracy while minimizing numerical dissipation of kinetic energy so that the resolved turbulent fluctuations remain physically meaningful [112; 113]. Combustion is represented using a Strain-sensitive Flamelet-Generated Manifold (S-FGM) formulation [10]. In this approach, the tabulated chemistry includes the sensitivity of the source terms to local strain, which improves the representation of multi-mode flame behavior relative to more conventional Flamelet-Generated Manifold (FGM) and Flamelet Progress Variable Approach (FPVA) formulations.

The S-FGM formulation adopted here follows the approach presented by Sharma et al. [10]. To incorporate strain effects into the tabulated chemistry description, a family of strained counter-flow premixed flamelets is constructed. Consistent with the tabulation framework, the manifold is parameterized by the mixture fraction, Z, and the progress variable, C, defined as $C = Y_{\mathrm{H_2O}}$. To represent the effect of imposed strain, an additional coordinate based on the OH mass fraction, Y_{OH}, is introduced. The flamelet solutions are computed using the H_2/O_2 chemical mechanism of Li et al. [114] with FlameMaster [115]. Strain is introduced through a counter-flow premixed flame configuration following the stretched premixed flame formulation of Rogg [116]. In the present implementation, a back-to-back configuration is employed. Although previous studies have shown that back-to-back and fresh-to-burned arrangements can yield different characteristics for laminar stretched flames [117], they have also shown that the resulting flame structures become nearly identical for tabulation purposes once the flamelets are mapped onto the same manifold coordinates [118]. For this reason, the back-to-back configuration provides a practical basis for the present tabulation strategy.

The strained premixed flamelets exhibit the characteristic S-shaped response of peak temperature with strain rate. The unstable branch of this response is difficult to obtain numerically and requires an arc-length continuation procedure, as implemented in FlameMaster [119; 115]. In addition, the flamelet-generation procedure is accelerated and stabilized by using Cantera to provide a high-quality initial guess for the strain rate before the final FlameMaster calculations are performed [120]. Unlike previous strained-FGM formulations developed mainly for premixed turbulent flames [121; 122], the present formulation is designed for the jet-in-crossflow configuration, where strong strain and fuel-air stratification coexist in the windward shear layer. To account for this coupled effect, premixed flamelets

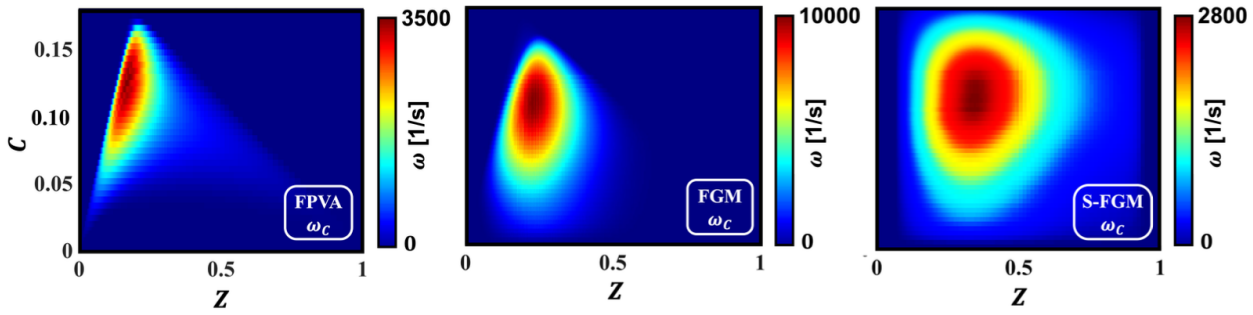


Figure 3.2: Source terms plotted in progress variable–mixture fraction space for FPVA, unstrained-FGM, and strained-FGM (S-FGM) tabulations from left to right, adapted from Sharma et al. [10].

are generated over a range of fuel-air compositions rather than for a single premixed state. In this way, the tabulated manifold accounts simultaneously for the effects of strain and local fuel-air mixing. To be precise, 120 points were extracted from the mixing branch, and a total of 4800 flamelets were solved to capture the S-shaped response for the sampled compositions.

The choice of the additional strain coordinate is important. A suitable marker must vary rapidly over small spatial scales so that it remains sensitive to the local strained flame structure. Several species could, in principle, be used for this purpose, including H_2 and excited hydrogen species, but prior analysis has shown that OH provides a more effective parameterization of strain effects in strained flamelet manifolds [121; 118]. For this reason, Y_{OH} is selected as the additional manifold coordinate in the present S-FGM formulation.

Figure 3.2 compares the tabulated source terms for FPVA, unstrained FGM, and S-FGM in progress variable and mixture fraction space. The source term shown for S-FGM corresponds to a specific level of the additional strain coordinate. The unstrained FGM formulation exhibits the highest peak source term because it does not account for strain-induced weakening of reactivity. In contrast, both FPVA and S-FGM show substantially reduced peak values, reflecting the influence of strain. At the same time, the S-FGM source term broadens over the composition space, particularly for $0.5 \leq Z \leq 1.0$, indicating that burning flamelet solutions remain available over a wider range of local mixture states. This broader support leads to relatively larger reaction rates than FPVA in these regions and is important for representing highly strained, partially premixed flames, where stabilization depends on the coupled effects of mixing, strain, and chemical reactivity.

The tabulation is constructed using 4800 flamelet solutions in the (Z, C, Y_{OH}) space, as shown in Fig. 3.3. The subgrid-scale distribution of mixture fraction is represented with a β-PDF through the transported mixture fraction variance, while δ-PDF closures are used for the progress variable and OH mass fraction. A unity Lewis-number assumption is adopted

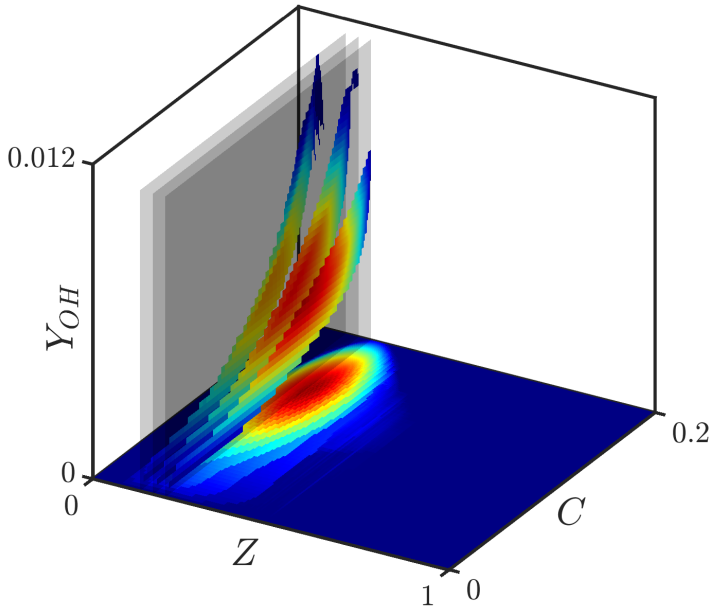


Figure 3.3: 3-D view of the S-FGM tabulation with vertical slices of reaction source visualized at different Z levels.

in the LES description, consistent with the original formulation used for the high-Reynolds-number hydrogen jet cases. The LES grid is strongly refined in the reaction region, with an effective mesh count of approximately 30 million cells and near-wall resolution of about $y^+ \approx 5$. The grid filter is chosen to resolve the dominant energy-containing structures in the jet shear layer and wake while retaining a tractable computational cost; the remaining subgrid scalar fluctuations are represented through the presumed-PDF closure.

3.2.0.2 High-Fidelity AMReX Simulations

The higher-fidelity simulations are performed with the compressible finite-volume solver described in Chapter 2. The governing equations are solved on block-structured Cartesian grids with adaptive mesh refinement and an embedded-boundary representation of the injector geometry. Convective fluxes are evaluated using a limited interpolation procedure together with an HLLC approximate Riemann solver, while viscous fluxes are computed using second-order central differencing. Detailed hydrogen-air chemistry is represented using the 9-species, 21-reaction mechanism of Mueller et al. [11]. Differential diffusion is incorporated through a mixture-averaged transport model, allowing the local species diffusivity to vary with the evolving mixture composition. The inflow and outflow boundaries are treated using Navier-Stokes characteristic boundary conditions with species treatment, which is important for the subsonic reacting-flow regime of the present configuration [81]. The relaxation

parameters are taken as $\sigma = 0.25$ at the outflow and $\eta_i = 3.0$ at the inflow. Turbulent inflow fluctuations are introduced by mapping a homogeneous isotropic turbulence field to the inlet plane. In the present configuration, the inflow fluctuation level is defined by an rms velocity of 5 m/s and a Taylor length scale of $\lambda = 0.125$. The top and bottom walls are treated as non-slip boundaries. Adaptive mesh refinement is used to resolve the flame front, the near-wall region, and the surrounding vortical structures without uniformly refining the entire domain. In the hydrogen-enriched cases, refinement is driven by the heat-release rate and vorticity magnitude. With five levels of refinement, the minimum cell size is $\Delta = 19.5$ μm, corresponding to approximately $y^+ = 0.65$ in the near-wall region under cold-flow estimates. A characteristic premixed flame thickness of about 247 μm yields roughly 12 cells across the flame front at the finest level. In the 70% hydrogen-by-volume cases, the AMR study spans multiple refinement levels, leading to approximately 50 million cells at level 3, 70 million cells at level 4, and 130 million cells at level 5. Additional details of the grid-refinement study and convergence behavior are provided in Appendix A. This refinement strategy makes it possible to resolve both the flame surface and the surrounding transport structures while keeping the full three-dimensional calculation computationally feasible.

Besides the use of finite-rate chemistry and differences in grid refinement, another important distinction between the present high-fidelity AMReX-based solver and the previous LES with S-FGM is the inclusion of differential diffusion (DD) and the use of characteristic boundary conditions. Accordingly, a series of verification and validation cases was performed to assess both the mixture-averaged diffusion model and the characteristic boundary condition treatment within the current framework.

First, to verify the implementation of differential diffusion, a purely two-dimensional diffusion case without convection was considered at $T = 300$ K and $p = 1$ atm. On the left side of the domain, the initial composition was set to $Y_{H_2} = 0.5$ and $Y_{N_2} = 0.5$, while the right side was initialized with $Y_{OH} = 1$.

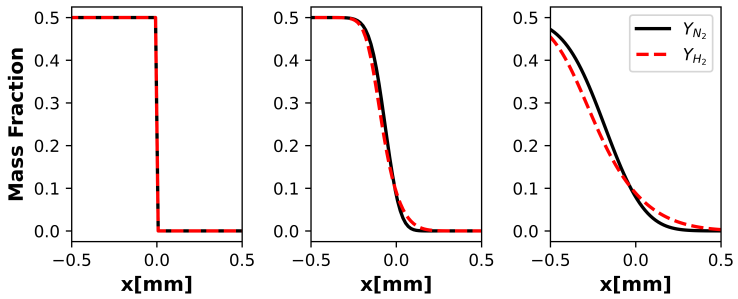


Figure 3.4: Mass fraction evolution showing diffusion of different species into a pure OH region.

The results at three different time instants are shown in Fig. 3.4. They clearly demonstrate the faster diffusion of hydrogen relative to nitrogen. In addition, even hydrogen diffuses to the left and right at different rates because of the different mixture compositions on the two sides of the interface; this asymmetric behavior is captured by the mixture-averaged diffusion model. Quantitatively, the computed diffusivities of H_2 and N_2 agree with values obtained from Cantera [123].

Next, a vortex-convection case was used to verify the basic implementation of the NSCBC treatment. This two-dimensional test consists of a vortex convecting toward the right boundary ($x = L$). The initial temperature is uniform at 300 K, while the pressure field is prescribed as

$$p(x, y) = p_{\text{ref}} - \rho_{\text{ref}} \frac{G^2}{R_v^2} \exp\left(-\frac{(x-a)^2 + (y-b)^2}{2R_v^2}\right), \tag{3.2}$$

and the density ρ is determined from the equation of state using the specified T and p. The flow field is defined through the stream function

$$\Phi(x, y) = G \exp\left(-\frac{(x-a)^2 + (y-b)^2}{2R_v^2}\right), \tag{3.3}$$

where G is the vortex strength, R_v determines the vortex size, and (a, b) denotes the vortex center. The velocity components are then obtained as

$$U_x = U_{x,\text{ref}} + \frac{1}{\rho} \frac{\partial \Phi(x, y)}{\partial x_2}, \tag{3.4}$$

$$U_y = \frac{1}{\rho} \frac{\partial \Phi(x, y)}{\partial x_1}. \tag{3.5}$$

Figure 3.5 presents an instantaneous snapshot of the U_x iso-lines at $t = 0.06$ ms. The left boundary is treated as an NSCBC inflow, the top and bottom boundaries are no-slip walls, and three different right-boundary conditions are considered: Case A1 uses a zero-gradient outflow condition, Case A2 uses NSCBC outflow without transverse terms, and Case A3 uses NSCBC outflow with transverse terms. For the transverse-term treatment, $\sigma = 0.25$, and β is taken to be the local outlet Mach number in each cell, approximately 0.1. The results in Fig. 3.5 demonstrate the importance of the transverse terms for this vortex-convection problem. In Cases A1 and A2, the iso-lines show clear fluctuations near the walls and distortion of the vortex core, indicating spurious reflections. In contrast, Case A3 remains free of such reflections and preserves the vortex structure as it exits the domain. This result highlights the importance of including transverse terms in NSCBC for accurate

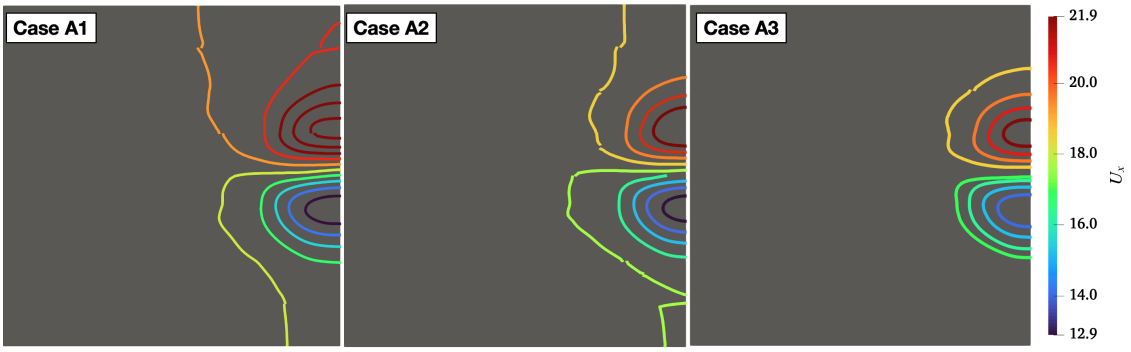


Figure 3.5: Instantaneous snapshot of U_x iso-lines for three outflow treatments: zero-gradient extrapolation (left), NSCBC without transverse terms (middle), and NSCBC with transverse terms (right).

treatment of multidimensional flow structures.

To further examine the role of species treatment in the NSCBC formulation, another test case was considered in which the domain was initialized with a Gaussian distribution of O_2 in the central region, while the remainder of the domain was filled with N_2. The species fields are prescribed as

$$Y_{O_2} = \exp\left(-\frac{(x-a)^2 + (y-b)^2}{2R_v^2}\right), \tag{3.6}$$

$$Y_{N_2} = 1 - Y_{O_2}, \tag{3.7}$$

where (a, b) denotes the center of the Gaussian distribution. The inflow corresponds to an air mixture, with $Y_{N_2} = 0.767$ and $Y_{O_2} = 0.233$, convecting in the x-direction at 20 m/s.

In this case, the NSCBC treatment for species becomes essential because the inflow composition differs from that inside the computational domain. Figure 3.6 shows that the NSCBC formulation allows the user to prescribe an arbitrary inflow mixture independently of the interior composition, while also allowing the Gaussian Y_{O_2} distribution to leave the domain smoothly without spurious oscillations. By contrast, if zero-order extrapolation were used for the mass fractions, the inflow composition would be artificially forced to match the interior cell values adjacent to the boundary, thereby constraining the specified inlet mixture. This issue becomes even more important in reacting flows, where strong chemical source terms near the inlet can couple species and pressure variations. Under such conditions, zero-order extrapolation of mass fractions becomes both inaccurate and nonphysical. The following test addresses this more challenging situation.

Finally, the JICF configuration discussed above was used to assess the NSCBC treatment under more realistic flow conditions. Figures 3.7c, 3.7b, and 3.7a show the temporal evolution

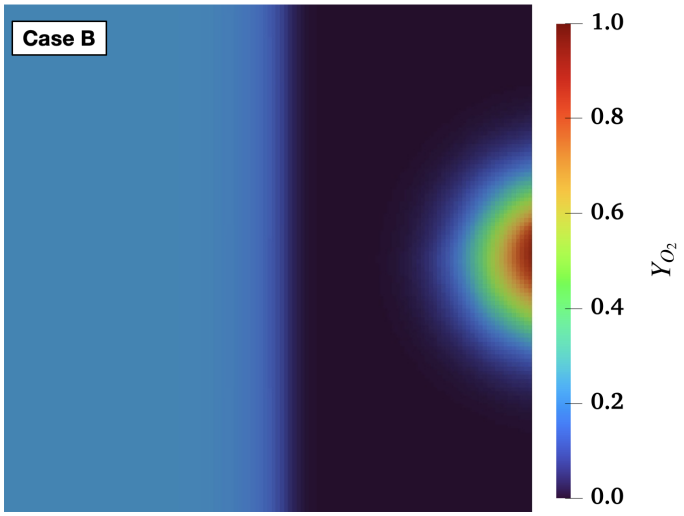


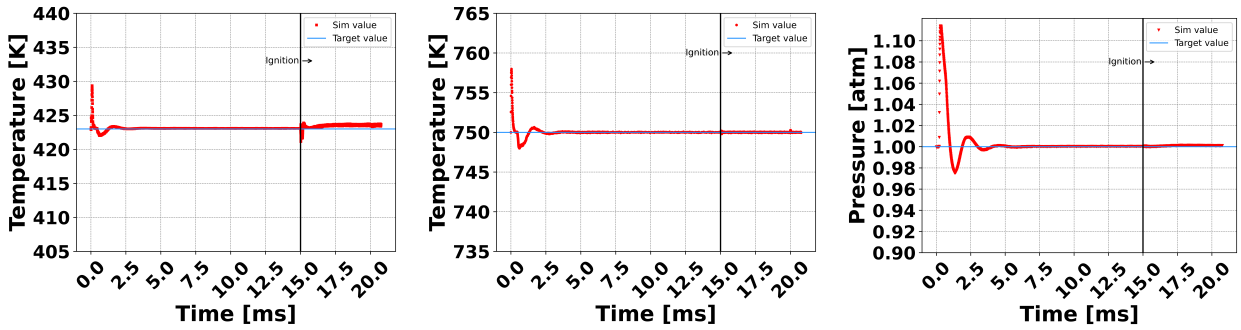
Figure 3.6: Contour of O_2 mass fraction for Case B.

of thermodynamic quantities at different boundaries. A cold-flow simulation was first run for 15 ms, with $\eta_i = 3.0$ at the injector inlet and $\eta_i = 10.0$ at the crossflow inlet, since a rapid response to turbulent fluctuations is required there. It should be noted that increasing η accelerates convergence but does not necessarily improve numerical stability. At the outlet, $\sigma = 0.8$ was used so that the initial transients decay rapidly toward a steady cold-flow solution.

As shown in the figures, the pressure fluctuation at the outlet remains within approximately 10%, although its magnitude is influenced by both the mesh resolution and the selected value of σ. During ignition at $t = 15$ ms, marked by the vertical black line, oscillations at the injector inlet are observed before the boundary signals settle again. In this transient oscillations stage, a relatively small η_2 value is important for maintaining stability. Because the flame stabilizes primarily in the jet-wake region, no additional reaction-specific treatment is required at the inflow boundary. At the outflow, mesh coarsening helps minimize wave reflection and suppresses upstream propagation of high-frequency disturbances.

3.3 Results and Discussion

These two modeling approaches provide a useful framework for further interpretation. The LES with the S-FGM formulation offers an efficient reduced-order description of turbulence-chemistry interaction and large-scale flame organization, while the higher-fidelity finite-volume simulation resolves the detailed coupling among flow structure, transport, and finite-rate chemistry. Their comparison, together with the experimental reference, helps separate



(a) (b) (c)

Figure 3.7: Temporal evolution of (a) temperature at the injector inlet, (b) temperature at the channel inlet, and (c) pressure at the channel outlet.

which aspects of the flame are governed primarily by large-scale flow organization and can therefore be captured by a reduced-order model, and which aspects depend more directly on local chemistry-transport coupling, differential diffusion, and branch-specific stabilization behavior. In this way, this configuration serves not only as a canonical hydrogen flame problem but also as a basis for assessing what level of modeling fidelity is required to represent the important stabilization physics.

3.3.1 Flame Morphology

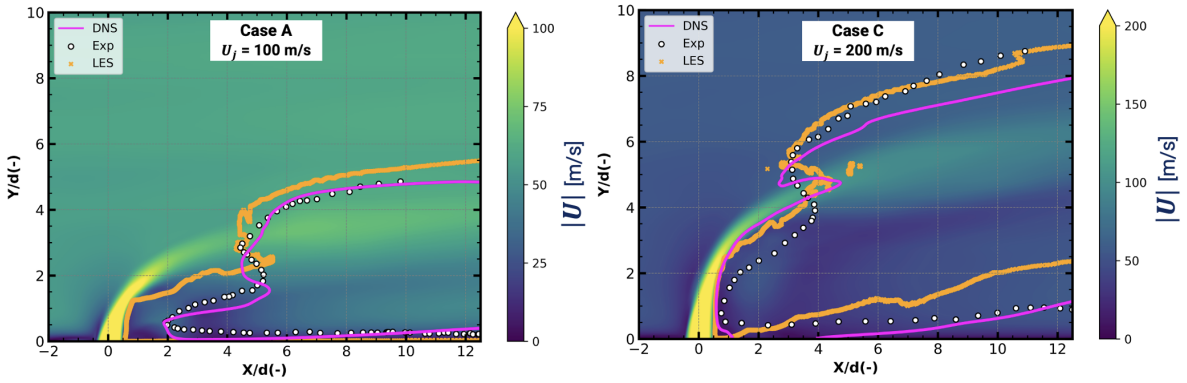


Figure 3.8: Contour plots (at the z centered planes) of temporally averaged velocity of DNS overlaid with Y_{OH} iso-lines from both DNS and LES compared to experimental findings (black dots).

For Cases A and C, the temporally averaged iso-contour of the OH mass fraction was plotted, overlaid on the contour of the magnitude of the velocity in Fig. 3.8 for both LES and DNS. Using this contour, the flame shapes are compared with the experimental results

in [12]. The comparison is not limited to visual agreement. The branch locations, attachment distances, and connection points provide quantitative measures of how the three-dimensional jet wake and upper-shear-layer dynamics change the flame relative to a laminar or two-dimensional reference. In both cases for both LES and DNS, the flame separates into two branches: a lee-stabilized branch controlled primarily by wake recirculation and a lifted branch controlled primarily by upper-shear-layer strain and stratification.

Quantitatively, increasing the momentum-flux ratio from $J = 1.96$ to $J = 8.41$ increases the jet velocity from 100 to 200 m/s for the 70% hydrogen cases and doubles the jet Reynolds number from $Re_j = 3000$ to 6000. This change modifies the dominant stabilization environment: the lower-J case is more sensitive to the weak lee-side recirculation region, whereas the higher-J case produces stronger lifted-branch intermittency and a more distinct connection region between the lifted and lee-stabilized branches. The measured and simulated connection locations differ by about one jet diameter: for Case C, the DNS places the concave connection near $y/d = 5$, while the LES and experiment place it near $y/d = 4$. Because $d = 2$ mm, this corresponds to an approximately 2 mm uncertainty in the mean branch-connection height, which is a useful quantitative measure of model sensitivity in the most multi-mode part of the flame.

In Case A with $U_j = 100$ m/s, both DNS and the experimental results show the flame stabilized approximately two jet diameters (2d) downstream of the jet exit. This can be attributed to the presence of a low-strength recirculation zone on the lee side of the jet in Case A. This region is affected by combustion-induced volumetric expansion, leading to a reduction in the local Reynolds number, which is attributed to the increased viscosity resulting from elevated temperatures within the reaction zone. This phenomenon induces laminarization of the mixing layer and spatial detachment of the vortical region from the reaction zones that occur near the jet exit. This intensifies the differential diffusion effect that causes the hydrogen gas to diffuse faster downstream, resulting in a detached flame that stabilizes further downstream of the injector. Therefore, due to the unity Lewis number assumption in the current LES, it still shows the flame completely attached to the jet in the recirculation zone. In the lifted flame regime, the elevated velocity from the fuel stream and the increased alignment between the crossflow and the jet stream intensify the role of turbulent structures, significantly influencing local fuel stratification. As a result, differential diffusion effects have a negligible impact on flame characteristics in this region, enabling both LES and DNS to accurately predict the shape and position of the lifted branch.

In contrast, Case C exhibits a higher fuel-stream Reynolds number ($Re_j = 6000$ at $J = 8.41$, with $Re_c = 44000$ in the crossflow), which induces strong turbulent mixing. This intensified turbulent mixing predominantly influences the flame characteristics, especially

within the lifted flame branch. In this regime, LES demonstrates the capability to accurately capture the flame shape and stabilization location as a result of second-order numerics with a kinetic energy-preserving scheme. Moreover, due to the higher jet velocity of the fuel stream, larger velocity fluctuations and local flame quenching are observed in the lifted flame branch in both simulation results. In the lee region, both DNS and LES reveal that the flame remains anchored to the jet, aligning well with experimental observations. This behavior is likely attributed to the strong recirculation zone in Case C, which promotes the entry of the oxidizer into the zone, leading to premixed-type burning. Furthermore, in the downstream region of the lee-stabilized branch, the DNS effectively captures the flame elevation caused by wake vortices originating from the side of the mid-plane. In contrast, the LES tends to overpredict the extent of this lift, highlighting differences in the two methods in precisely representing fluid-chemistry interactions in the boundary layer due to the varied level of grid refinement. At the merging or connection point between the lifted and lee-stabilized branches, the DNS (at y/d = 5), LES (at y/d = 4), and experimental (at y/d = 4) results predict different locations for this concave connection point. These discrepancies highlight the sensitivity of this region to the interplay between turbulence, stratification, and flame dynamics, resulting in a high probability of multi-mode combustion. These observations indicate that stratification strongly influences the unsteadiness of the flame and plays a crucial role in shaping its characteristics in this connection zone.

3.3.2 Cross-stream Flow Field

To develop a more comprehensive understanding of strain effects on the flame, particularly in Case C, the flow fields from DNS and LES at two cross-stream planes located at x/d = 2.25 and 4.00 downstream of the jet are compared in Fig. 3.9. The background contour plots represent the standard deviation of the velocity, highlighting fluctuations associated with strain effects. The DNS quiver plot illustrates the direction of the velocity vectors, while the LES streamlines depict the overall flow path, highlighting the trajectory of fluid motion. The contours reveal that both DNS and LES capture similar recirculation regions and strain distributions. Near the injection region, strong strain effects are observed along the upper edge of the jet penetration region, which suppress flame stabilization. However, as the flow progresses downstream, velocity fluctuations and strain effects diminish across the cross-stream plane, facilitating flame stabilization at these locations. These findings align with the flame stabilization characteristics depicted in Fig. 3.8 in the previous section. The streamlines indicate that the flow begins to rise with the injection (marked by vertical red arrows); further downstream, there is lateral recirculation in the cross-stream direction that

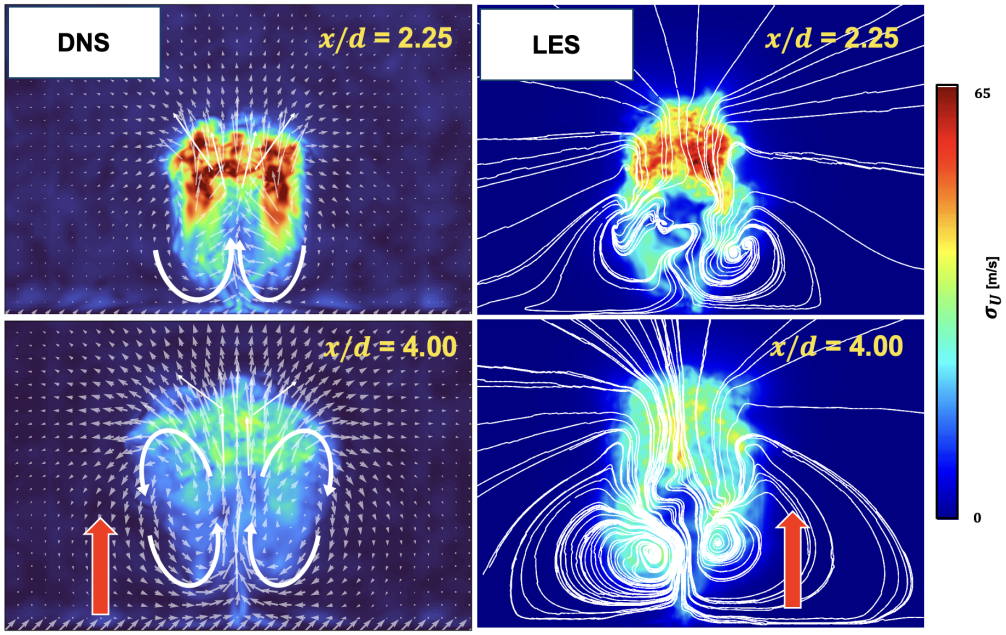


Figure 3.9: standard deviation of flow velocity (superimposed with streamlines and quivers) profiles along the flow direction from both LES and DNS for case C. Planes taken at $x/d =$ 2.25 and 4.00 downstream of the injector.

subsequently converges at the center plane (z-centered), ultimately stabilizing the flame along the mid-channel plane. The next section presents details on the flame dynamics resulting from these velocity fluctuations.

3.3.3 Flame Branch Analysis

Figure 3.10 shows the distinct flame branches in Case C, where three instantaneous velocity fields are plotted with overlaid Y_{OH} contours to highlight three unique flame branches. Three types of lifted branches are observed, as described in [12]. The left column illustrates the "straight-edge" branch with narrow horizontal OH layers, depicting the continuous flame surface on the upper-lifted branch. The flame surface is wrinkled, and the leading edge location suggests that the flame has enveloped the jet. The edge of the flame branch depends on the strain induced by the flow. The edge is usually seen downstream of the maximum strain location, and this scenario can be viewed as a balance between volumetric expansion due to heat release and the convection of the flow structure. As this branch moves downstream, it can be influenced by the normal directional velocity gradient, leading to wrinkling at the flame's leading edge. This wrinkling often results in the flame attempting to connect with the lee-stabilized branch, forming the "hooked branch" as shown in the middle column. Further downstream, the flame is fully lifted, but due to strain-induced fluctuations, local

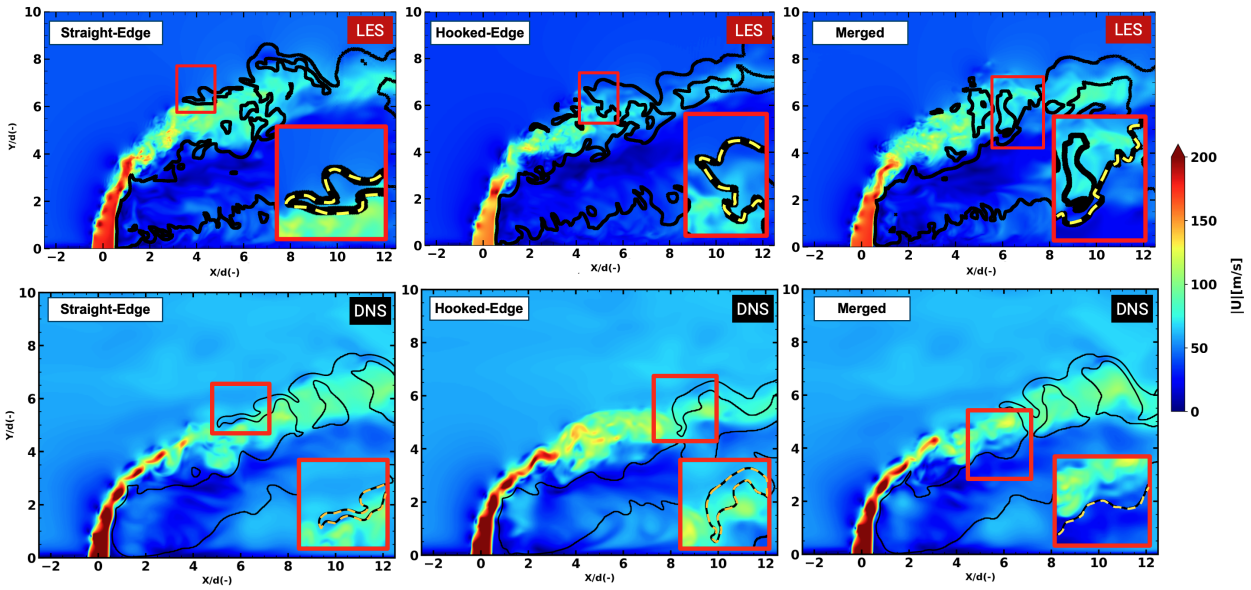


Figure 3.10: Flame Branch configurations (at the z centered planes) of Case C at different time instances. Top row: LES results. Bottom row: DNS results. Background is velocity magnitude contour overlaid with Y_{OH} iso-lines(black solid lines) representing the flame front dynamic. The inset images show the zoomed-in view of the key features for each time instance.

extinction is observed intermittently. This is where the lifted branch successfully merges with the lee-stabilized branch, and the two move downstream together and are referred to as the "merged branch" in the right column. It is important to note that even though these three branches in LES and DNS appear in different locations, the repetition of this pattern is consistent in both simulations. In Case C, both simulations successfully capture the temporally averaged flame shape and qualitatively reproduce the instantaneous flame branches with reasonable accuracy compared to the experimental results. An extended quantitative comparison of LES and DNS results in the chemical space is presented in the next section.

3.3.4 Flame Edge Characteristics

Figure 3.11 presents a comparative analysis of the flame front in chemical space using the Z and Y_{OH}. Scatter plot points, sampled at different times and a single location for each subplot, are compared against strained and unstrained flame solutions from Cantera [123] at varying strain rates. It should be noted that in the unstrained flame, Y_{OH} is lower than the strained values; however, the temperature (not shown here) of the unstrained flame is higher, as expected. Similarly, the peak temperature aligns with the stoichiometric condition ($Z_{st} = 0.17$), whereas the maximum Y_{OH} values occur under slightly leaner conditions.

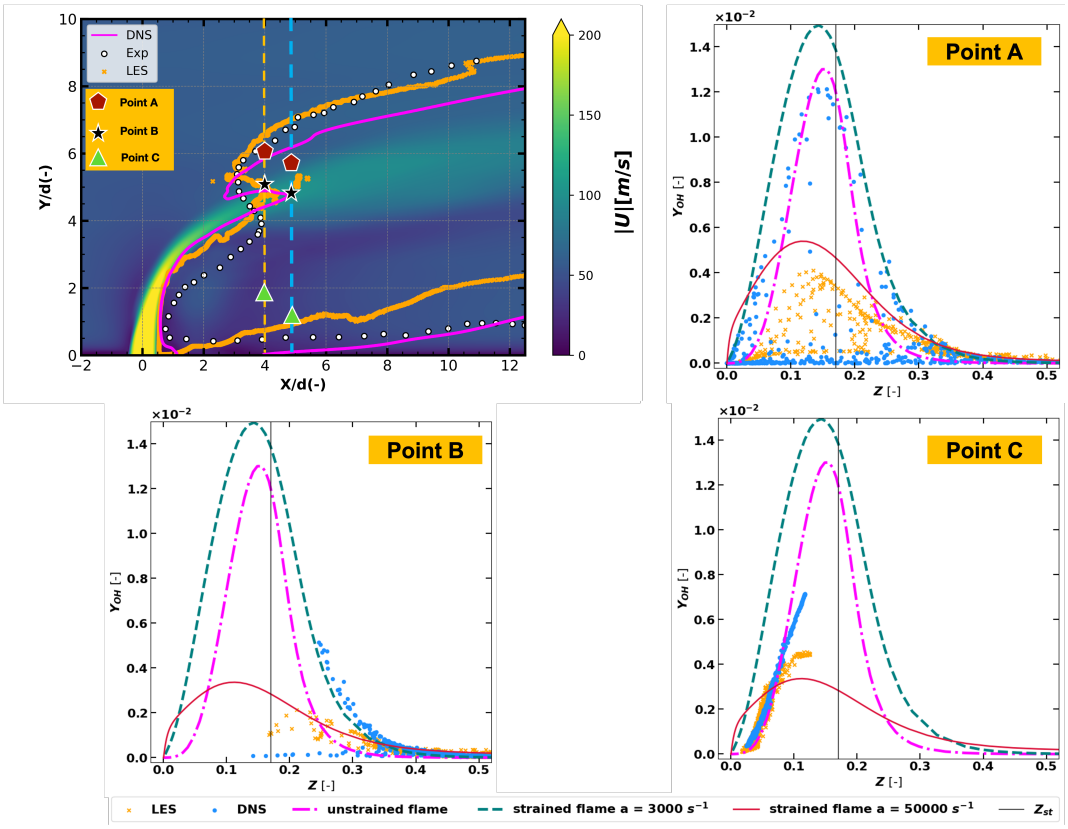


Figure 3.11: Plots for temporal average data (at the z centered planes) from DNS and LES at different points on the flame front. Points A, B and C are assumed close to the edge of the flame and corresponding Y_{OH} vs. Z data is presented with low strain and high strain solutions.

At point A, located at the top edge of the lifted flame branch, the plot shows that LES aligns with the strain rate curve of 50,000 s^{-1}, while DNS data follows the curve corresponding to a strain rate of 3,000 s^{-1}. This is due to the limitation of the flamelet table in covering the entire range of strain rates during the tabulation. Fig. 3.3 shows a global view of the S-FGM tabulation, with multiple vertical slices (shaded) of the tabulated reaction source for different levels of Z, where the effects of the strain rate are characterized by Y_{OH}. It can be shown that only a certain range of Y_{OH} is tabulated due to converging challenges during the canonical counter-flow flame calculations. The intermediate values are interpolated along the Z and C axes to fill the table. However, both simulations display a distribution over a wide range of Z values, indicating high flow fluctuations in the shear layer that result in the stratification of the fuel mixture and intermediate reaction states. In DNS results, many points are observed to follow the unstrained flame curve, particularly near stoichiometric conditions ($Z_{st} = 0.17$). Building on the discussion of the "straight-edge" branch in the previous subsection, the wide range of Z and Y_{OH} values provides quantitative

confirmation of the earlier findings. This suggests that the S-FGM effectively captures strain-induced local flame quenching and accurately represents the shape of the lifted branch.

At point B, located at the concave region where the lifted and lee-stabilized flame branches connect, the scatter plot shows a trend similar to that at point A. DNS results align with a higher strain rate curve than LES, but both simulations show that the Z and Y_{OH} values are concentrated in a very narrow range on the fuel-rich side. This is due to the constant ingress of fresh hydrogen from the fuel stream into the zone. Unsteady flame anchoring at this location prevents any upstream propagation of the flame due to the rich fuel region behind the jet-bending location.

At point C, located inside the lee-stabilized flame branch, results from both simulations follow the curve of the unstrained flame because of the low strain effects in this zone, and the majority of the points are concentrated in a narrow region of Z values, indicating a premixed reaction in this region. In addition, when the mixture fraction increases ($Z > 0.1$), both solutions show a deviation from the unstrained curve. However, similar to other locations (A and B plots), the value Y_{OH} was again underestimated by the flamelet model. This indicates that only when strain effects appear does the S-FGM model underpredict the reaction intensity.

To further explore the reaction states in the simulations, a continuous time sequence is represented in phase space to illustrate the ignition-extinction cycle observed at point A (Fig. 3.12). In the DNS results, two distinct cycles, called Path 1 and Path 2, exhibit cyclic burning characteristics. However, these cycles exhibit a substantial disparity in the Y_{OH} values, with Path 2 displaying approximately five times the magnitude observed in Path 1. This disparity highlights the variations in reaction intensities occurring at the same spatial location. Both paths exhibit considerable variation in Z ($\Delta Z \sim 0.4$), indicating a substantial influence of large-scale flow characteristics during the cycle. This effect is particularly evident in the role of stratification, which introduces irregularities in the availability of the combustible mixture. During ignition, the progress variable exhibits a rapid and steep angle change, suggesting a premixed trajectory. Subsequently, a slow extinction process is observed, characterized by nearly straight-line motion towards the origin, indicative of a diffusion-controlled phenomenon. The LES results at the same location reveal a trajectory closely resembling that of Path 1. However, Path 2 is absent from the LES results, suggesting that the S-FGM model can capture the ignition-extinction cycle at the lifted flame branch despite underpredicting the intensity or Y_{OH} values compared to finite-rate chemistry results. This observation aligns with the findings discussed in the previous section. Moreover, both simulation results suggest the potential presence of a partially-premixed combustion regime in this lifted flame branch.

This trajectory analysis provides the quantitative comparison to a laminar flame reference that is required for model interpretation. A laminar strained flame at a fixed strain rate traces a narrow curve in (Z, C, Y_{OH}) space, whereas the three-dimensional turbulent lifted branch repeatedly crosses multiple strained-flame families and samples $\Delta Z \sim 0.4$ during a single local cycle. The progress-variable trajectory is therefore not a monotonic laminar evolution at fixed mixture fraction. It contains a rapid premixed-like rise during ignition followed by a slower diffusion-controlled return toward lower C and Y_{OH}. The absence of the high-Y_{OH} Path 2 trajectory in the LES indicates that the reduced manifold captures the lower-intensity ignition-extinction cycle but underpredicts the full range of finite-rate radical production produced by the resolved three-dimensional flow.

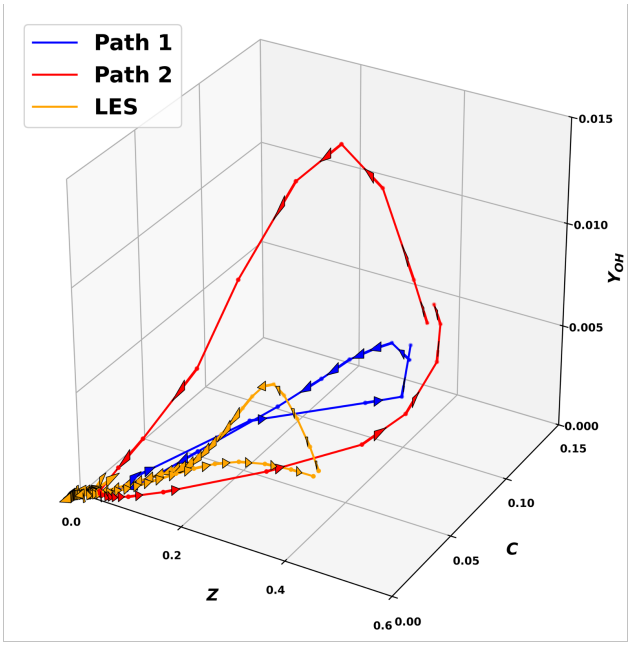


Figure 3.12: Point trajectories in Flamelet phase space for Case C. Path 1 and 2 are from DNS.

To analyze the stratification characteristics at point A, Fig. 3.13 plots the probability density functions (PDFs) of the mixture fraction. The distribution is well-approximated by a β-PDF, with a mean value $\tilde{Z} = 0.18$, which is close to the stoichiometric condition. However, the square of variance $\widetilde{Z''^2} = 0.03$ is relatively high, indicating a variability of nearly 100%, with the probability density function exhibiting a prominent peak with a value significantly greater than 1 on the lean side. This suggests that the stratification in this region promotes predominantly non-premixed flame behavior, sustained by a continuous supply of fresh oxidizer from the crossflow. Consequently, the presumed β-function PDF [124; 125] for sub-grid scale mixture fraction closure, originally developed for non-premixed

flames, remains valid in this region for representing the turbulent mixing process.

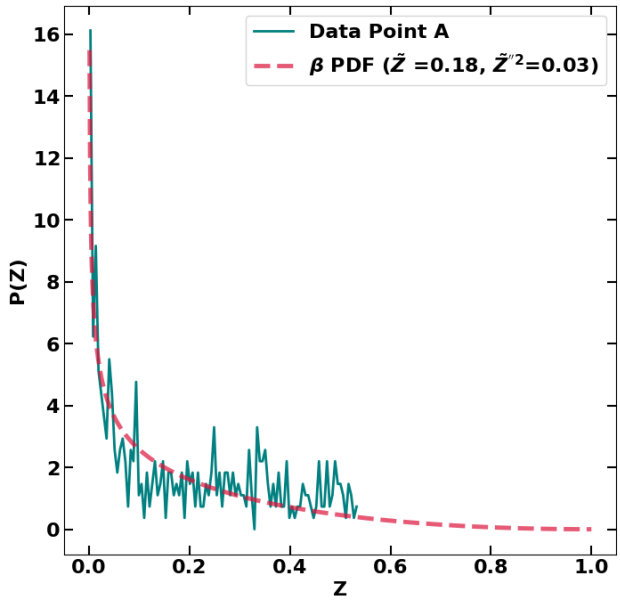
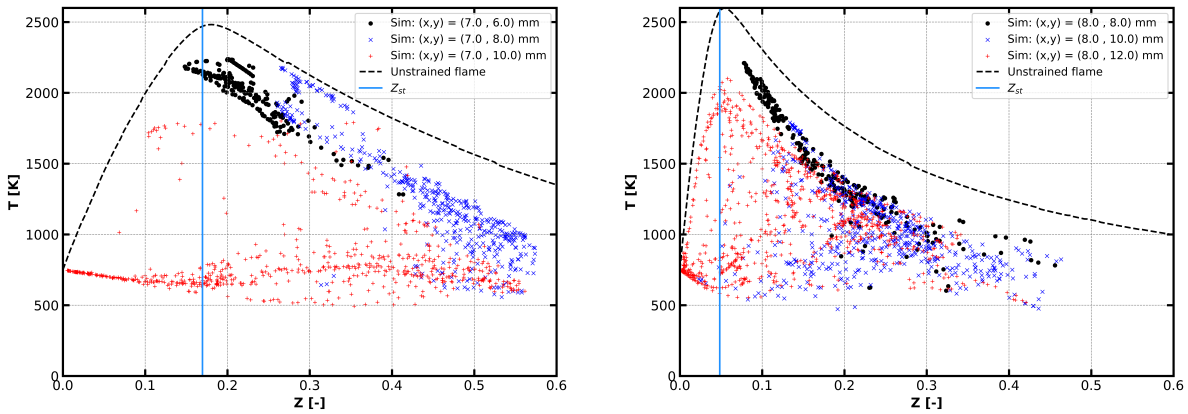


Figure 3.13: DNS mixture fraction data fit with β distribution at Point A.

3.3.5 Hydrogen enrichment

To better isolate the controlling stabilization mechanisms, high hydrogen-percentage-by-volume cases are considered, since the increased reactivity enhances the sensitivity of the flame to local transport and chemical effects. In Case C9, the fuel hydrogen content by volume increases to 95%, resulting in a lower density of the fuel stream. To achieve consistent jet characteristics with Case C7, the jet-momentum ratio ($\boldsymbol{J}$) of 8.41 was maintained constant, resulting in an increased jet velocity of 342 m/s. The increased hydrogen content by volume reduces the fuel density by approximately a factor of three relative to Case C7. Although the higher jet velocity preserves penetration characteristics similar to those of Case C7, the reduced jet density intensifies the shear effects ($\nabla\rho$ increases) caused by the relatively denser crossflow. The increased hydrogen content by volume also causes the shear layer burning to be notably intensified. To further understand the differences in the flame characteristics and mixing behavior between the two cases, a detailed thermodynamic analysis of the flame front is presented in Fig. 3.14.

The scatter plot of T and Z for both Case C's, with a constant jet momentum ratio, is presented in Fig. 3.14 along the flame front. Furthermore, a stratified premixed unstrained flame was simulated using Cantera [123], with equilibrium results included as a reference. Based on the scatter plot for Case C7 in Fig. 3.14a, the lee-stabilized branch (for y$\simeq$6



(a) Case C 70% H_2 by volume

(b) Case C 95% H_2 by volume

Figure 3.14: Scatter plot of temperature versus mixture fraction at flame front location of different cases

mm) shows a well-mixed state, with temperatures approaching those of an unstrained flame. This region exhibits low-strain and elevated temperatures, indicating strong combustion. In contrast, the lifted branch samples (for y≥8 mm) show a wide range of mixing levels and combustion properties compared to the unstrained flame. The data points are distributed across a wide Z-range, with distinctive lower reaction temperatures and states closer to mixing rather than consistent burning. Occasionally, elevated temperatures are observed, signifying sporadic burning. This behavior highlights the presence of intermediate reaction states as fresh gasses mix with combustion products, where ignition and extinction are equally probable. This behavior is attributed to the high strain rates and velocity fluctuations characteristic of this flame branch, leading to richer fuel compositions.

For the high-hydrogen case shown in Fig. 3.14b, the points are again plotted in the vicinity of the flame front (now shifted by 1 mm downstream). The points in the lee-stabilized branch are more concentrated on the leaner side compared to Case C7; however, they are spread across the Z-range and still align with the stratified premixed flame results. This behavior is attributed to the increased velocity of the jet near the edge of the lee branch. In contrast, the lifted branch in this case shows better stratification than in the 70% H_2 by volume case because of the increased density gradient and the resulting increase in shear-layer fluctuations. The points at the edge of the lifted branch (see y = 12 mm) exhibit an ignition-extinction cycle, characterized by an elliptical spread in T ∈ [550, 2100] K around the stoichiometric Z value (Z_{st}). This behavior is absent at the edge of the lifted branch in Case C7 (y = 10 mm) due to reduced mixing. Furthermore, the lifted branch is located further below the unstrained flame than in the 70% H_2 by volume case, as local

strain effects dominate in this region and promote flame extinction. Both observations in the lifted flame branch can be attributed to changes in the level of fluctuations within the mixing layer, driven by the reduced fuel density, which imposes a greater local strain on the flame. Additional results and further details of the hydrogen-enrichment study will be presented in Section 5.5.

3.3.6 Implications for stability-map construction

The quantitative branch behavior in this chapter can be translated into a simulation-based stability-map framework for staged hydrogen injection. The natural operating coordinates are J, Re_j, Re_c, hydrogen volume fraction, density ratio, and crossflow temperature, while the local stability indicators are branch lift-off distance, flame-edge strain rate, scalar dissipation rate, mixture-fraction variance, and the amplitude of ignition-extinction excursions in (Z, C, Y_{OH}) space. The present cases show how such a map would be populated. Case A7 at $J = 1.96$ and $Re_j = 3000$ occupies a regime where lee-side differential diffusion and weak recirculation shift the flame base approximately $2d$ downstream. Case C7 at $J = 8.41$ and $Re_j = 6000$ occupies a regime where the flame remains anchored in the lee branch but the lifted branch exhibits strong intermittent excursions. Case C9 preserves $J = 8.41$ but increases the hydrogen content to 95% by volume and the jet velocity to 342 m/s; this moves the lifted branch toward a more strained and more extinction-sensitive regime, with $T \approx 550$–2100 K around Z_{st}. For engine-relevant staged injection, these results indicate that flame stability cannot be inferred from fuel composition alone. The relevant design question is whether the flow places the flame edge in a low-strain recirculation-supported state or in a high-strain shear-layer state with large mixture-fraction and progress-variable excursions.

3.4 Summary and Conclusions

This chapter examined flame stabilization in hydrogen jets in crossflow through a combined comparison of experimental measurements, LES with a strain-sensitive flamelet-generated manifold model, and higher-fidelity finite-volume simulation with detailed chemistry and differential diffusion. Across the cases considered, the flame consistently organized into two principal stabilization branches: a lee-stabilized branch supported by the wake recirculation behind the jet and a lifted branch embedded in the upper shear layer. The results showed that these two branches are governed by different local balances among strain, mixing, recirculation, and chemistry, so the flame cannot be interpreted as a single uniform stabilization mode.

The comparison with the experiment showed that both numerical descriptions capture the dominant large-scale flame morphology and the two-branch structure of the reacting jet in crossflow. At the same time, the higher-fidelity simulations revealed important branch-dependent differences in the local combustion behavior. The lee-side branch was associated with a lower-strain, more recirculation-supported transport environment and exhibited states closer to stratified premixed burning, whereas the lifted branch sampled a broader range of thermochemical states and displayed stronger intermittency, ignition-extinction behavior, and sensitivity to the upper-shear-layer dynamics. Analysis in projected chemical space further showed that the lifted branch cannot be described by a single narrow family of flame states, but instead evolves through a wide range of partially reacted and intermittently burning conditions.

The hydrogen-enriched cases provided a clearer view of how these transport effects change with composition. Increasing the hydrogen content from 70% to 95% by volume at a fixed jet momentum ratio preserved the large-scale penetration behavior but altered the local flame response, especially in the lifted branch. The lower fuel density required a higher jet velocity and produced stronger density gradients, enhancing fluctuations in the shear layer. As a result, the lifted branch exhibited broader thermochemical excursions, stronger ignition-extinction behavior, and a greater departure from the unstrained flame reference. The lee-stabilized branch remained comparatively compact in state space and closer to stratified premixed-flame behavior, indicating that the effects of differential diffusion and hydrogen enrichment are strongly branch dependent rather than spatially uniform.

These results also clarify an important modeling point. Although flamelet-based hydrogen models have been extended to include differential diffusion in differential premixed flames and, separately, to include differential diffusion together with flame stretch in hydrogen flame calculations [126; 127; 128], combining differential diffusion, strong mixing, and strain effects into a single reduced-order manifold remains difficult for the present jet-in-crossflow problem. In addition to the branch-dependent impact of differential diffusion, the flame-edge analysis showed that the S-FGM tabulation does not fully cover the range of strained reaction states sampled in the flow. In the lifted branch, where the flame experiences strong shear-layer fluctuations and large local strain, the LES results were constrained by the limited tabulated range of Y_{OH} and therefore underpredicted the local reaction intensity relative to the detailed-chemistry solution. This limitation is less important in the lee-stabilized branch, where the strain is weaker and both simulations remain closer to unstrained or weakly strained flame behavior. These findings indicate that the present jet-in-crossflow flame spans stabilization environments ranging from weakly convecting lee-side recirculation zones to high-subsonic shear-layer regions, so the relevant physics cannot be represented adequately with a compact

tabulation. A more complete manifold treatment would require additional coordinates and auxiliary transport variables to retain the dependence on differential diffusion, local strain, and mixing-history effects, thereby increasing the table size and diminishing the computational advantage of the flamelet approach. For the remaining studies, the AMReX-based finite-volume solver is therefore used as the primary tool since it resolves the coupled flow, transport, and chemistry interactions directly and is better suited for a detailed analysis of flame stabilization in more complex hydrogen combustion systems.

CHAPTER 4

Flame Stabilization and Characteristics in a Multi-Tube Micromixer

4.1 Introduction

The broader experimental and numerical context for multi-tube hydrogen combustors has been discussed in Chapter 1. Prior experimental and computational studies have shown that, in these systems, the flame is shaped not only by the nominal operating conditions but also by the coupled effects of confinement, injector arrangement, local mixing, flow redistribution, and interactions among neighboring flame branches. At the same time, important limitations remain. Experiments have revealed substantial spatial variation in flame structure and combustor response, but the local mechanisms governing these variations are difficult to measure in closely packed multi-flame configurations. Simulations, in turn, have provided valuable insight into the internal reacting flow and design insights, yet often under simplified numerical approaches that do not fully capture the dynamic coupling among distributed injection, local transport, and spatially varying flame behavior. As a result, the detailed mechanisms through which flame stabilization is established and maintained in multi-tube hydrogen combustors remain incompletely understood. This issue is particularly important because flame stabilization provides the organizing framework through which the overall combustor behavior can be interpreted. Even when the geometry and boundary conditions are nominally symmetric, multi-tube combustors may develop spatially nonuniform flame structures, unequal branch intensities, and locally distinct burning states. Such behavior indicates that the combustor cannot be understood as a simple collection of independent premixed flames. Instead, combustion is sustained through a coupled multi-flame system in which recirculation, transport, injector-to-injector interaction, and heat-release distribution jointly determine where the reaction is anchored and how the combustor responds. For hydrogen combustion, this problem is further intensified by the high reactivity of the fuel and the strong sensitivity of flame behavior to local mixture and transport variations, so that

relatively small differences in flow distribution or mixing can produce disproportionately large changes in flame structure and stabilization.

Accordingly, this chapter examines the multi-tube combustor as a coupled reacting-flow system, with emphasis on the physical mechanisms linking distributed injection, internal flow redistribution, spatial flame variation, and local flame stabilization. The analysis is directed toward clarifying how combustion is organized within the combustor and why different flame branches can exhibit distinct structures and stabilization behaviors, even within a nominally regular distributed-injection configuration. In this way, the chapter establishes the physical basis for interpreting flame behavior in multi-tube hydrogen combustors and for understanding the broader stabilization challenges that emerge in more complex staged combustion systems.

4.2 Experimental Configurations and Simulation Setup

Table 4.1: List of cases based on experiments [13; 14]

Name	**Crossflow Composition**			**Crossflow Velocity (m/s)**	**Crossflow Temperature (K)**	**Fuel Jet Velocity (m/s)**	ϕ **(Global)**
	$Y_{\mathbf{O_2}}$	$Y_{\mathbf{N_2}}$	$Y_{\mathbf{CH_4}}$				
Case A	0.231347	0.761558	0.007095	159.09	761.50	212.70	0.524
Case B	0.233000	0.767000	-	162.16	758.30	302.84	0.530

Experiments [13; 14] were carried out using a premixed multi-element combustor operated at a mean chamber pressure (p_{CC}) of about 11 bar. The combustor is made up of three primary sections: an air manifold, a staged fuel-air micromixer consisting of 19 discrete injection elements, and a combustion chamber. Heated air is introduced into the air manifold from a critical flow sonic nozzle and is isolated from downstream injector components with 19 choked orifices. The micromixer is divided into three segments for the independently controlled injection of ammonia, methane, and hydrogen. A sonic nozzle at the exit of the combustion chamber pressurizes the combustor. Planar laser-induced fluorescence (PLIF) imaging of the OH (hydroxyl) radical was performed at 100 kHz.

High-fidelity numerical simulations are performed using the finite volume solver [72; 81] based on block-structured AMR with an embedded boundary (EB) implementation for complex geometry, as discussed in Chapter 2. The scenarios considered (Table 4.1) for the current analysis are consistent with the experimental setup at a similar global equivalence ratio (ϕ) with both hydrogen fuel (H_2-N_2 75/25 vol.%) at 294.3 K, issuing perpendicularly into the crossflow. In case A, with both hydrogen and methane as fuels, a methane-air mechanism with 13 species and 38 reactions [129] is used, while case B uses a H_2-air mechanism with 9 species and 21 reactions [11] for detailed chemical kinetics. The domain has dimensions of

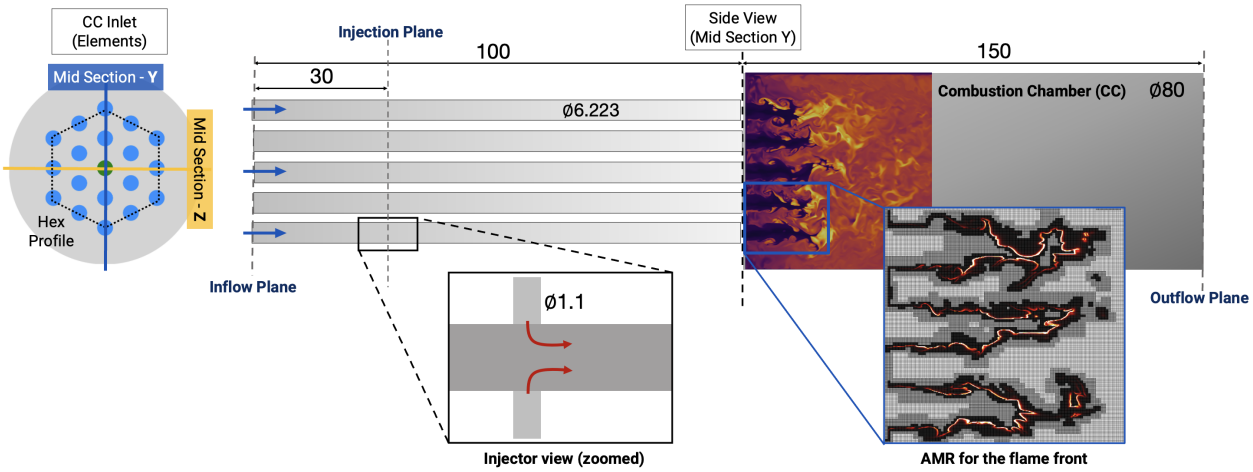


Figure 4.1: Plot shows the computational domain with major dimensions. Front view presents the mid-section Y and Z planes. The inset at the injection plane highlights the jets and the approximate fuel trajectory, while the second inset depicts the various AMR levels surrounding the flame front. All dimensions are in millimeters (mm).

250×80×80 mm, with a fuel injector diameter $D_j = 1.1$ mm and a tube element diameter of $D_e = 6.223$ mm. Figure 4.1 shows the detailed schematic of the computational domain and the mesh refinement on the flame front. The mesh was dynamically refined based on the heat release rate (HRR) and vorticity magnitude to capture the flame and flow vortices. Regions with HRR exceeding 5×10^9 W/m^3 and vorticity magnitudes above 5×10^4 s^{-1} were refined to the finest level. Using four refinement levels ($\Delta = 48.75\ \mu m$), the simulation reaches ∼504 million cells. Given an estimated flame thickness of 423 μm (from a 1D premixed flame of similar composition with a spatial average equivalence ratio of ~ 0.298 calculated from the time-averaged transverse plane at the tube exit), this yields a resolution of nearly 10 cells across the flame. Additionally, the resolution of the turbulent boundary layer was assessed by computing the non-dimensional wall coordinate $y^+ = \frac{u_\tau \delta}{\nu}$ from the simulation data [130]. The resulting value of $y^+ \approx 0.5$ confirms that the first grid point lies well within the viscous sub-layer, indicating adequate mesh refinement for wall-bounded turbulence. However, accurately resolving reacting flows involves complexities beyond specifying a target y^+ or a uniform cell density per flame thickness. As discussed further in Section 4.3, the combustion chamber exhibits significant mixture stratification, requiring spatial resolutions that vary with local conditions to accurately capture the flame front. Cantera calculations for freely propagating premixed flames at 10 atm and 600 K with equivalence ratios in the range $\phi \in [0.2, 1.3]$ show flame thickness variations from approximately 4512 μm to 30 μm. At the current finest AMR level ($\Delta x = 40\ \mu$m), the mesh resolution corresponds to roughly 115 cells to just 1 cell across the flame front. While this confirms that the mesh adequately resolves

the flame structure in most regions, it remains necessary to identify zones where the flame front may be under-resolved. As highlighted later by Fig. 4.5, most of the domain operates under lean conditions, with a small fraction of cells reaching stoichiometric or rich mixtures. Therefore, although the current grid spacing is sufficient in most of the domain, targeted mesh refinement in regions with richer mixtures would be necessary to ensure full resolution of the flame front. For subsonic flow, the boundary faces used characteristic boundary conditions [81]. The relaxation parameters are set as $\sigma = 0.1$ for the outflow and $\eta_i = 3.0$ for the inflow. The walls are non-slip and isothermal, maintained at crossflow temperature following the experiments.

The resolution regime of this chapter should therefore be interpreted as AMR-assisted implicit LES with detailed finite-rate chemistry. The finest AMR spacing, 48.75 μm, gives approximately 9–10 cells across the representative lean premixed flame thickness of 423 μm and a wall resolution of $y^+ \approx 0.5$ in the near-wall region. Because the local equivalence ratio is strongly stratified, the effective flame resolution varies spatially: lean regions are well resolved, whereas locally richer and thinner flame segments can approach the grid-filter limit. The MTM results are therefore used to interpret resolved branch-scale stabilization, shear-layer heat release, recirculation, and flashback-relevant flame penetration, but they are not presented as a uniform-grid DNS of all turbulent scales in the 19-element combustor.

4.3 Results

4.3.1 Flame structure validation

First, the global flame behavior is analyzed and validated with the experimental data for both cases. Figures 4.2 present temporally averaged Y_{OH} contours from the simulation and temporally averaged OH PLIF intensity from the experiment for Cases A and B, respectively. The bottom row of Fig. 4.2 provides a comparison for the flame in the top row, where the edges of the jet core are marked by the blue dashed lines, highlighting similar flame stabilization locations for both simulations and experiments. Hereafter, the flow exiting the tube element is referred to as the jet or streams. In addition, the contours of both figures reveal that regions with significant OH intensity exhibit a conical shape around the premixed mixture stream in both cases, indicating shear layer reactions in a narrow region. For Case A, the overall flame structure closely matches the experimental results and shows consistent reactions near the jet exit for all flame branches. In Case B (right column of Fig. 4.2), the simulations reveal a distinct lifted flame detached from the tube exit,

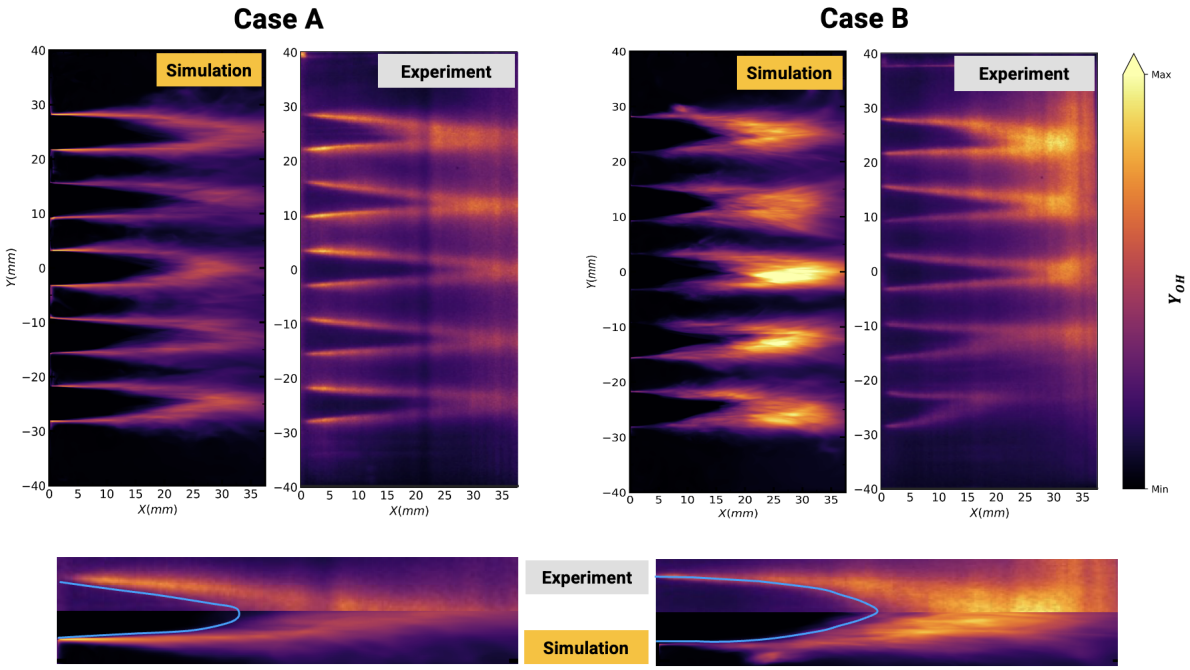


Figure 4.2: Time-averaged Y_{OH} for both Cases. Top row shows the mid-section Y planes for the combustion chamber, while bottom row presents one-to-one comparison for the topmost tube element flame structures.

attributed to fuel stratification for each flow stream caused by the high fuel injection velocity, which will be discussed in Section 4.3.2. This phenomenon is consistent with the higher OH PLIF intensity seen downstream in the experimental data. The simulation also successfully captured the experimental trend that Case B exhibits a weaker flame-branch attachment at the jet exits compared to Case A. However, the simulated attachment appears even weaker than what is observed experimentally. This discrepancy can be partly attributed to the fact that the experimental OH PLIF signal, normalized by the maximum pixel intensity, does not correspond directly to the simulated OH mass fraction. Consequently, PLIF images enable qualitative comparisons of the heat release structure (or spatial distribution of OH) relative to simulations, but they are not treated here as calibrated absolute measurements of Y_{OH} or heat release rate.

This distinction is important for interpreting the experimental uncertainty. The available 100 kHz OH-PLIF data provide high-speed information about relative flame structure, branch position, and attachment/detachment trends, but the normalized PLIF intensity is affected by laser-sheet nonuniformity, shot-to-shot energy variation, collisional quenching, temperature dependence of the fluorescence signal, and image normalization. Therefore, the validation metric used in this chapter is the spatial organization of the flame branches

and their relative attachment behavior, not pointwise agreement in absolute OH magnitude. The subsequent quantitative discussion is based on simulation-derived quantities that are directly defined in the governing equations, including ϕ, Y_{OH}, heat release rate, strain rate, velocity, and recirculation structure. This is also why the experimental comparison is used to establish that the simulation captures the correct flame morphology before the simulation fields are used to diagnose local stabilization mechanisms.

4.3.2 Global flame dynamics

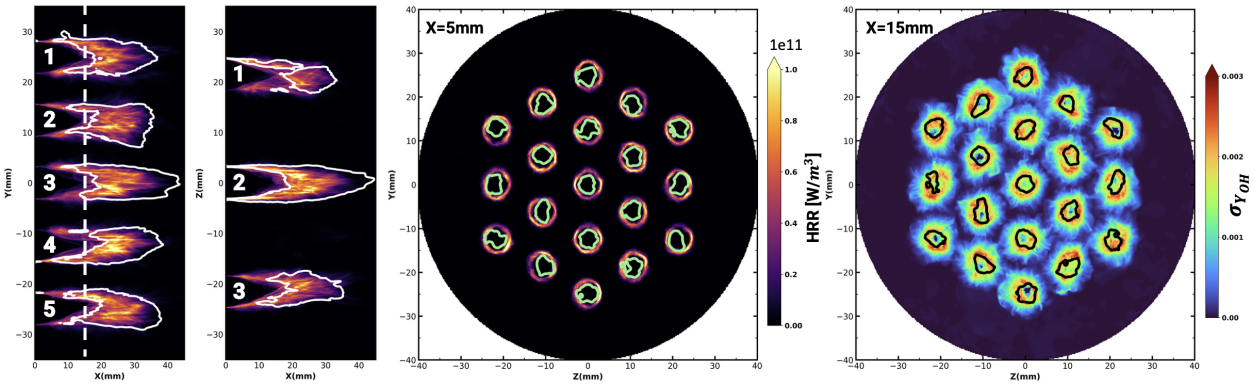


Figure 4.3: Time-averaged heat release rate (HRR) and standard deviation of Y_{OH} fields illustrating the global flame structure for Case B; The left three columns show HRR on the mid-section Y plane, mid-section Z plane and transverse plane at X = 5 mm downstream of the tube exit, respectively; The rightmost column displays the standard deviation of Y_{OH} on the transverse plane at X = 15 mm downstream of the tube exit; White solid line on mid-section planes are the isoline of OH mass fraction $Y_{\mathrm{OH}} = 0.00125$ as 30% of the maximum value; Green and black solid lines on transverse planes are the isoline of mixture fraction $Z_{\mathrm{Bilger}} = 0.0811$ corresponding to $\phi = 0.53$.

The global flame features are examined for the complete tubular bundle by plotting multiple temporally averaged slices as shown in Fig.4.3. The two plots on the left in Fig.4.3 present contours of the heat release rate (HRR) in the mid-section Y (five streams) and Z planes (three streams). In the Y-plane slice, most flame branches exhibit attachment near the jet exits, albeit with relatively weak flame anchoring for three flame branches at Y = ± 3.1, -9.18 and 22.5 mm. Similarly, in the Z-plane slice, two notably weak flame attachments are observed at Z = ± 18.5 mm, indicating localized zones of reduced flame intensity and stabilization. To visualize different global flame features, the white isoline of $Y_{\mathrm{OH}} = 0.00125$ is overlaid on the heat release contour in the mid-section planes. This value corresponds to 30% of the maximum Y_{OH} value in the flow and tends to include regions exhibiting flame

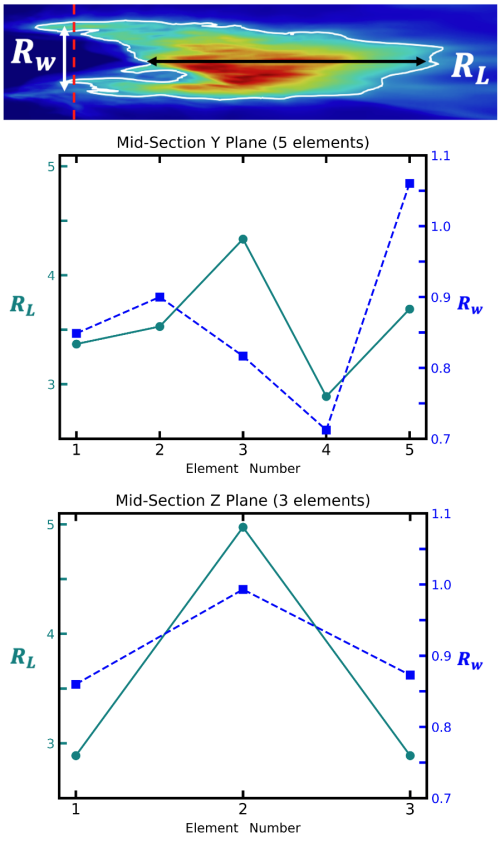


Figure 4.4: Visual definition of R_W and R_L on the top row; Reaction zone length and thickness for mid-section Y and Z planes on middle and bottom row respectively; Element number are shown for each plane separately in Fig. 4.3.

initiation along with the main reaction zone, thus marking the flame boundaries. The isolines on both the mid-section Y and Z planes reveal that the central flame exhibits a longer and more symmetric structure compared to those associated with the outer tubes. Additionally, the magnitude and confined distribution of the HRR for the central tube indicate more stable and consistent combustion over time. This flame suggests that the central region of the combustor supports a more regularized flow with minimal fluctuations and less fluid strain on the flame front.

To highlight the variation in flame structure, the width and length of the primary reaction zone for each flame branch are measured and plotted as line graphs in Fig. 4.4. The numbers 1 to 3 or 5 are assigned in top to bottom order for the tubes shown in Fig. 4.3. The width of the reaction zone R_W is defined as the distance along the red dashed line (X = 10 mm). This distance is measured between the two highest Y_{OH} values at the edge of the reaction zone marked in white. The length of the reaction zone R_L is measured from the beginning to the end of the region along the X direction, contained within the white isoline of $Y_{\mathrm{OH}} = 0.00125$,

as shown in Fig. 4.4. The observed values are further normalized with D_e in the line plots. The plots confirm that the center flame has the longest reaction zone on both Y and Z mid-section planes. However, it also exhibits a 30% smaller flame width in the Y-direction compared to the Z-direction, where neighboring tube elements are further apart, reflecting non-uniform interactions among flow streams in each direction. In particular, based on the plot in Fig. 4.4, the flame of element number 4 in the mid-section Y plane (also shown in Fig. 4.3) presents the shortest reaction length and the narrowest width, consistent with the weak and unstable top shear layer reactions observed in the corresponding HRR contour in the mid-section Y plot in Fig. 4.3. In contrast, the flame of element number 5 has a moderate reaction length but an unusually large width in the Y direction and appears inclined toward the wall, suggesting lateral asymmetry induced by wall-bounded flow effects. The observed variations in flame branch shapes and features are primarily attributed to strong flow recirculation induced near the combustor walls.

To investigate the cause of flame structure variation, the mixing characteristics of fuel and air are quantitatively analyzed in Fig.4.5. The top row of the figure shows the spatial distribution of the local equivalence ratio (ϕ) on three transverse planes located at X = 0 mm, 5 mm, and 15 mm downstream of the jet exits. The bottom plot presents the ϕ profiles extracted along the black dashed line indicated in Fig.4.3, positioned at X = 15 mm. The transverse ϕ distributions illustrate the evolution of mixing characteristics as the flow propagates downstream, while the line plot highlights the degree of stratification across the mid-plane in the Y-direction, capturing the non-uniform distribution among the five jet streams. These results clearly indicate that substantial mixture stratification persists throughout the combustion chamber in all three dimensions, contributing to partially premixed flame behavior. The influence of stratification on flame behavior is observed by plotting the temporally averaged HRR contours and the standard deviation of Y_{OH} in the transverse planes in Fig. 4.3. The transverse plane X = 5 mm presents quantities in the shear layers burning, while X = 15 mm presents fields at the root of the primary reaction zone. These fields are overlaid with the isoline corresponding to a well-mixed condition (Z_{Bilger} at $\phi = 0.53$), providing a spatial reference for the stratification boundary. In the plane at X = 5 mm, the central flow stream shows the most symmetric circular isoline of the mixture fraction Z_{Bilger}, which remains centered within the jet core. Despite uniform stratification, the center flame shows a higher heat release and a thinner reaction layer along the Z-direction, indicating directional variations in flame structure, possibly due to asymmetric disturbances from adjacent jets, as previously demonstrated in this section. In contrast, the outer tubes exhibit fuel stratification that is offset from the center of each jet stream. As a result, the well-mixed region is displaced toward the jet core and is frequently quenched by

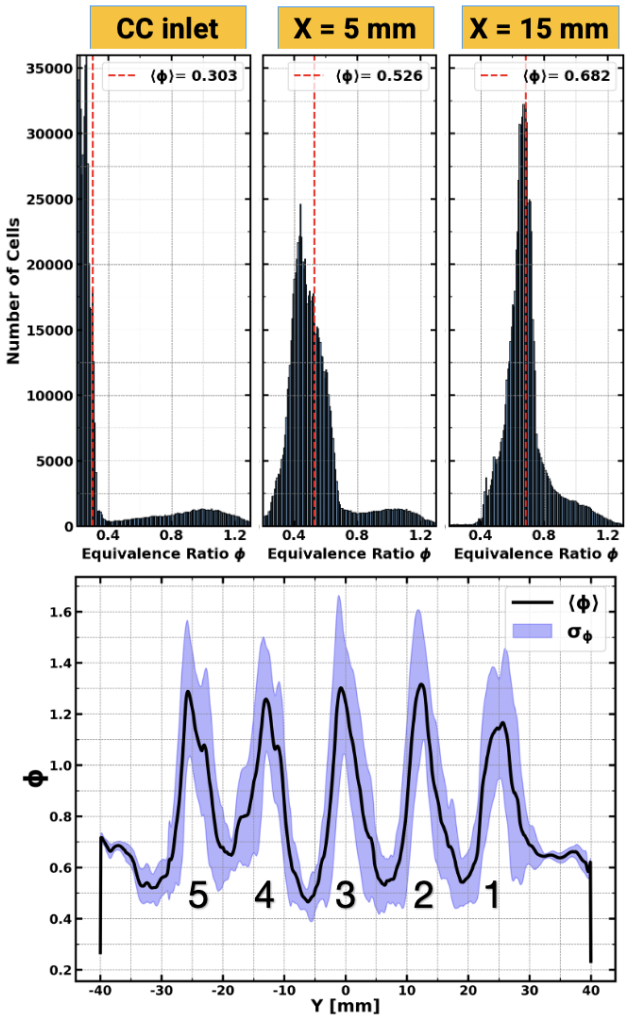


Figure 4.5: The local equivalence ratio profiles along the white dashed line indicated in Fig.4.3, located at X=15 mm downstream of the jet exits.

colder upstream mixtures with elevated strain rates, leaving relatively lean mixtures along portions of the jet stream edges. This leads to asymmetrical and weaker reactions along one side of the shear layer. An exception to the general trend is observed in the flame of element number 4 on the mid-section Y plane, where the fuel stratification remains centered within the jet stream. Despite this, the flame exhibits unstable shear layer reactions on one side, resulting in a shorter and narrower flame structure. This suggests that, in this case, the strain effect from flow-stream motion directly quenches the flame along the upper shear layer. The interactions between flow dynamics and flame structures are further discussed in Section 4.3.4 and 4.3.3. Further downstream, at 15 mm from the jet exit, the shear layer reactions have more time to develop, leading to more complex, non-circular flame shapes. As seen in this plane, these shapes begin to follow a curvature-aligned pattern in the outer

tubes, with higher magnitudes of Y_{OH} fluctuations closer to the walls. These distortions are likely driven by high-amplitude fluctuations in the velocity field in the vicinity of each stream that alter the lower density flame-containing flow during volumetric heat release. This hypothesis is investigated in the next section.

These measurements also provide the first connection between the simulated flame field and a design-oriented stability map. In the present stable operating point, the primary heat release is concentrated in the annular shear layers surrounding the tube-exit streams, while the low-speed inter-jet and near-wall recirculation zones contain substantially weaker heat release. From the time-averaged fields, the characteristic HRR level in the recirculation-dominated regions is approximately one order of magnitude smaller than the HRR in the dominant shear-layer reaction zones. This ratio is important for flashback interpretation. A recirculation zone is potentially dangerous when it stores enough heat and radicals to ignite or push a flame upstream into a premixer; in the present cases, however, the recirculation zones redistribute hot products and perturb the flame shape without becoming the dominant heat-release region. Combined with the high axial velocities through the tube elements, this prevents sustained upstream propagation into the tubes under the simulated conditions.

In this chapter, Z_{Bilger} denotes the Bilger mixture fraction, used as a conserved elemental mixture coordinate for comparing stratified states across the fuel and oxidizer streams [111]. The isoline $Z_{\mathrm{Bilger}} = 0.0811$ corresponds to the global well-mixed equivalence ratio $\phi = 0.53$ for Case B. Relative displacement of this isoline from the jet centerline is therefore a quantitative measure of local mixture stratification, not only a visualization feature. The combination of Z_{Bilger}, local ϕ, HRR, and strain rate defines the local state variables used below to interpret why some branches remain attached while others weaken or lift.

4.3.3 Local flame dynamics

The top row of Fig.4.6 presents a time series of flame front structures, visualized using HRR contours over a duration of 40μs, and the corresponding fuel contours are plotted at the same time in the bottom row for the three streams. The heat release contours reveal highly wrinkled flame fronts, consistent with observations in [14], along with localized discontinuities that are characteristic of partially premixed flame structures [131]. Following the flame in the red square and blue ellipse regions, there are reaction pockets forming inside the cold flow stream for the center and bottom jets [131]. These reaction pockets are formed on the flame front of the orthogonal directions and contain hot products, as shown in the images in the bottom row with the absence of hydrogen fuel. The pockets tend to convect towards the jet core in the transverse direction and affect the flame behavior. The reaction pocket

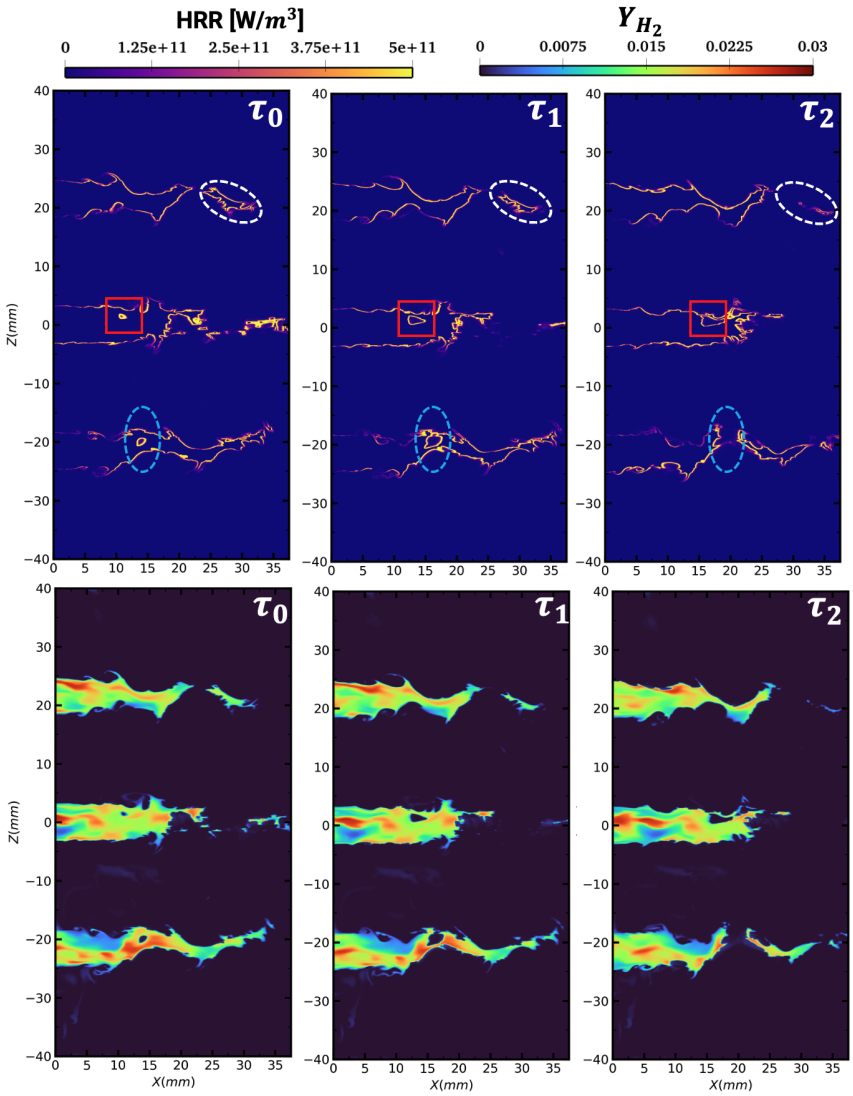


Figure 4.6: Time series images of HRR and fuel concentration representing reaction pocket and fuel filament advancement in Case B. The top row images show instantaneous HRR, while bottom row images depict fuel concentration rescaled to highlight reaction pocket and fuel filament.

formed in the center stream that convected toward the side of the flame branch directly altered the flame front and enhanced the unsteady flame structure. The second reaction pocket (in the blue ellipse) that formed in the bottom stream convected toward the center of the stream and cut the flame around 18 mm downstream of the jet exit, thereby changing both the flame front and the flame length of this stream. This gives rise to small pockets of unburnt fuel mass escaping from the main jet, called filaments hereafter.

The fuel filament (shown in the white ellipse) is subsequently consumed further downstream. Over the entire time history (not shown here), this pattern is observed to recur

for different tube elements. Another factor contributing to the emergence of these filaments, apart from the reaction pockets, is the presence of fuel stratification in the main flow stream, leading to the shedding of rich fuel filaments at the tip of the flow streams. Similar observations have been reported in experimental studies involving ammonia fuel [13; 14].

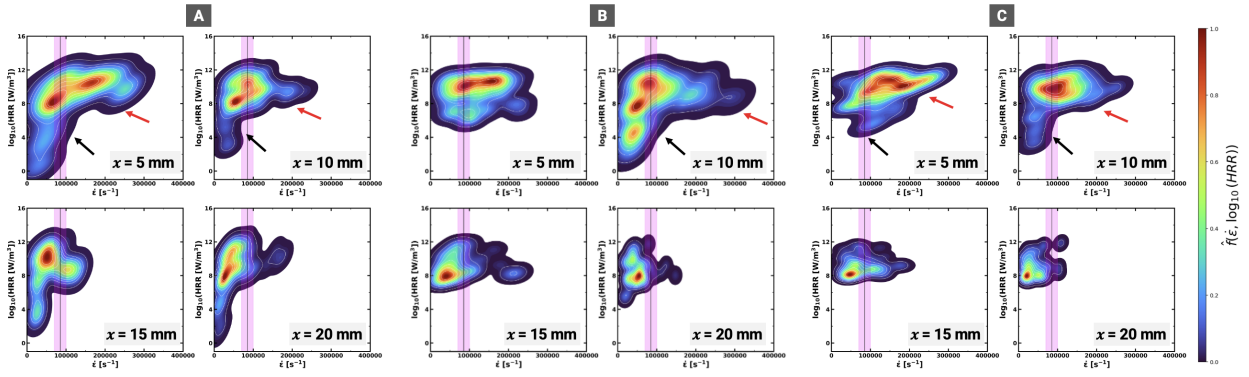


Figure 4.7: KDE plots for joint PDFs of $\dot{\varepsilon}$ and $\log_{10}(HRR)$ at location A measured along outer tube at Y-axis (marked 1 in Fig 4.3), B measured along outer tube at Z-axis and C for center tube for Case B; Four probe locations are used along the flame edge, downstream of the tube exit.

To provide a more quantitative analysis of the effect of strain on flame dynamics, the correlation between the local strain rate and heat release behavior at the flame edges is examined next. The strain rate is characterized using the principal extensive strain rate in three-dimensional space, following the definition in [12]. Specifically, it is computed as the largest eigenvalue of the symmetric strain rate tensor, $S_{ij} = \frac{1}{2}(\frac{\partial U_i}{\partial x_j} + \frac{\partial U_j}{\partial x_i})$,which captures regions of high extensive deformation in the local flow field. Next, figure 4.7 is plotted, representing the kernel density estimates (KDEs) of the joint probability density function (PDF) for the local principal extensive strain rate $\dot{\varepsilon}$ and the logarithm of the volumetric heat release rate $\log_{10}(HRR)$ obtained at selected probe locations along the flame edge. The x-axis denotes the strain rate in s^{-1}, and the y-axis represents the base-10 logarithm of the heat release rate in W/m^3. The colormap corresponds to the estimated joint density $\hat{f}(\dot{\varepsilon}, \log_{10}(HRR))$, where higher values indicate regions of increased statistical occurrence in the dataset. Isolines of constant density are overlaid in white for reference. Additionally, the magenta vertical band is added as a reference to denote the range of extinction strain rates for a premixed counterflow flame under representative conditions near the tube exit, accounting for variations in mixture composition. The solid vertical line within the band indicates the mean extinction strain rate.

Following the trends in plot A, at x = 5 mm, the distribution is broad and exhibits multiple HRR modes, including a significant high-strain lobe (red arrow) that suggests the presence

of transient or strain-tolerant flame structures. As the flow progresses downstream (x = 10–15 mm), the distribution becomes more localized near the extinction strain rate band, indicating partial-flame stabilization in that region. By x = 20 mm, the KDE becomes more compact with a slight reduction in peak HRR, suggesting a transition towards post-flame behavior. Overall, the flame appears weakly attached and highly dynamic, with evidence of both partial stabilization and sensitivity to local strain-rate fluctuations. In plots for location B, at x = 5 mm, the flame initially stabilizes near the extinction strain rate band, similar to location A. However, by x = 10 mm, the distribution broadens significantly (see black and red arrows) with a prominent high-strain tail, indicating stronger local-strain interactions and increased flame instability compared to A. Downstream at x = 15 mm and x = 20 mm, the HRR magnitude diminishes and the distributions fragment further, reflecting earlier onset of flame weakening and loss of coherence. Compared to plot A, the flame in plot B shows weaker stabilization, greater sensitivity to local strain, and a more fragile attachment to the tube exit. In contrast, Plot C (center tube) shows a distinctly different flame behavior. At x = 5 mm, the HRR distribution is broad with a pronounced high-strain tail extending well beyond the extinction limit (red arrow), indicating that substantial burning occurs under strong strain conditions, possibly due to shear-driven ignition or transient premixed flame elements. By x = 10 mm, while the peak remains near the extinction strain rate, the high-strain lobe persists, suggesting a continued coupling between flow-induced stretch and combustion. Compared to the A and B plots, the flame shows a stronger correlation between elevated strain rates and sustained HRR, especially downstream. At x = 15 mm, the distribution is still non-negligible beyond the extinction threshold, implying that the flame is resilient to strain-induced quenching. Even at x = 20 mm, the presence of multiple HRR modes across a narrow magenta strain range suggests localized re-ignition (reaction pockets) or persistent strain-modulated burning. In contrast to A and B, this configuration demonstrates more robust flame–strain coupling over a longer axial range, indicating that the local flame response is more tightly governed by the local straining field than by passive flame decay.

4.3.4 Flow field dynamics

Flame dynamics are directly influenced by the flow field variation induced by geometric effects. Figure 4.8 presents a time-instantaneous 3D streamline visualization (left and right plots) around two representative tubes—labeled 1 and 2—corresponding to the locations shown in the center plot with temporally averaged quiver data. In the 3D view, the incoming flow enters the combustion chamber in the positive X-direction. After entering the

combustion chamber, the jets spread in the transverse YZ plane and sustain combustion primarily within the shear layer regions surrounding each jet stream, as indicated by the temperature colormap. Flow motion at the recirculation zone near the jet exits is shown by the temporally averaged quiver plot on a transverse plane located 5 mm downstream of the jet exit in the middle of Fig. 4.8.

In this quiver plot, flow moving into the plane (streamwise or towards the outlet) is shown in red, recirculating flow moving out of the plane is shown in blue, and stagnant or low-velocity regions are indicated by white arrows following values of U_x. Based on the quiver plot, the center tube experiences relatively weak transverse flow motion, as indicated by the short arrow lengths. In this region, the flow is primarily driven by the flame draft and directed into the plane, as suggested by the red color representing positive U_x. Simultaneously, a weak transverse flow component in the Y-direction impinges on the flame front, contributing to the observed directional asymmetry in reaction behavior between the Y and Z axes for the center flame. In contrast, the outer tubes are subjected to stronger transverse flow motions, resulting from both wall-induced confinement effects and interactions between adjacent jet streams. In some cases, where fuel stratification is non-uniform, these tubes also exhibit additional flow motions driven by hydrodynamic instabilities associated with the stratification itself, as well as by asymmetric flame dynamics. These induced motions, in turn, further influence the flame behavior, leading to strong fluid-chemistry interactions.

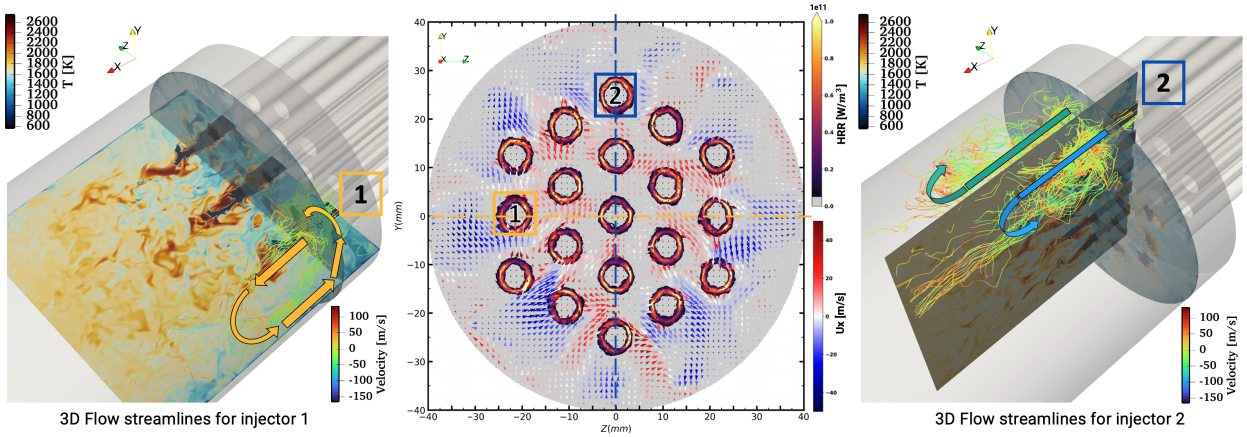


Figure 4.8: Instantaneous three-dimensional analysis of streamlines and recirculation zones for Case B. The left image shows the streamlines around flame structure for tube 2, and the right image depicts for tube 1; Image in the middle shows time-averaged quiver plot for X slice at 5 mm indicating recirculation and reaction zones.

However, not all outer tubes behave in the same manner, as discussed in Section 4.3.2. The flame of element number 4, located in the mid-section Y plane, displays a relatively short and narrow flame structure despite having a comparatively uniform fuel stratification. This

anomaly is attributed to the presence of transverse flow oriented perpendicular to the flame front, combined with a strong streamwise velocity component—evident from the dark red regions in the velocity field. This flow configuration imposes strain on the flame, contributing to the observed unsteady and dynamic flame behavior. For the flame of element number 5 in the mid-section Y plane, the flame is influenced by a recirculation zone directed out of the plane, which induces lateral flame motion. This results in the widest flame among all branches and causes the flame to incline toward the wall, as described in Section 4.3.2.

To confirm the flow motions observed in the quiver plot, 3D streamlines—colored by streamwise velocity—are examined next around the two representative tubes—labeled 1 and 2. Around tube 1, the streamlines display a relatively organized pattern (yellow arrows): flow exits the tube downstream along the main stream, recirculates upstream within the same XY plane, and re-engages with the main flow before wrapping around the tube. In contrast, the streamlines near tube 2 exhibit chaotic, unstructured movement throughout the 3D domain, lacking a consistent recirculation pattern. This disordered behavior likely arises from the more compact spacing and weaker confinement by adjacent tubes in that region. Additionally, localized vortical structures further modulate the flame's position and shape. These observations align with the patterns identified in the temporally averaged quiver plot that influenced tubes 1 and 2.

4.4 Summary

Before summarizing the physical results, it is important to restate the numerical regime of this chapter. The MTM simulations are implicit LES calculations with detailed chemistry and AMR. They resolve the dominant flame branches, recirculation zones, shear layers, and wall-adjacent flow structures that determine stabilization, but unresolved motions below the local grid filter are not modeled with an explicit subgrid closure. The stability conclusions should therefore be interpreted as resolved branch-scale design indicators.

This chapter examined flame behavior in a pressurized 19-element multi-tube micromixer using high-fidelity simulations validated against time-averaged 100 kHz OH-PLIF measurements. The simulated conditions correspond to approximately 11 bar chamber pressure, global equivalence ratios $\phi = 0.524$–0.530, crossflow velocities of 159–162 m/s, crossflow temperatures of 758–762 K, and fuel-jet velocities of 213–303 m/s. Validation was based on flame morphology and attachment trends rather than absolute OH intensity because the experimental PLIF data are normalized and are subject to fluorescence and optical uncertainties. Within that validation scope, the simulations captured the major experimental trend: the hydrogen-only case exhibits weaker attachment and a more lifted downstream

reaction structure than the hydrogen/methane case.

The central conclusion is that the combustor cannot be interpreted as a simple array of nominally identical premixed flame elements. The center and outer branches occupy different local stabilization environments even though the global geometry is regular. The center flame has the longest reaction zone and a more symmetric structure, while its reaction-zone width is approximately 30% smaller in the closer-spaced transverse direction than in the wider-spaced direction. Several outer branches exhibit weak attachment at specific transverse locations, including $Y = \pm 3.1$, -9.18, and 22.5 mm in the mid-section Y plane and $Z = \pm 18.5$ mm in the mid-section Z plane. These values show that branch-to-branch variability is spatially organized, not random.

The current operating points are stable with respect to upstream flame penetration into the tube elements. The reason is not only that the mean tube velocity is high, but that the heat-release distribution is unfavorable for flashback. The dominant HRR remains in the shear-layer reaction zones surrounding the tube-exit streams, whereas HRR in the low-speed recirculation-dominated regions is approximately one order of magnitude smaller. Thus the recirculation zones perturb flame shape and promote local branch asymmetry, but they do not become strong upstream heat-release kernels. This observation links the detailed simulation to a practical gas-turbine design rule: a low-speed recirculation zone is not automatically a flashback source unless it also contains sufficient heat release, radicals, and residence time to overcome the downstream convective flux through the tube.

The local flame dynamics reinforce this interpretation. Over a 40 μs sequence, the flame does not remain as a stationary surface; it forms wrinkled fronts, reaction pockets, and fuel filaments that convect and are consumed downstream. The strain-HRR joint PDFs show that different branches occupy different strain-response regimes. Some locations remain reactive at strain rates near or beyond the representative counterflow extinction band, while others fragment and weaken by $x = 15$–20 mm downstream of the tube exit. This branch-dependent strain response explains why a single representative tube element is not sufficient for evaluating stability margins in a multi-tube combustor.

For design use, these results motivate a simulation-based stability map for distributed hydrogen injection. The global map coordinates should include ϕ, pressure, hydrogen content, tube diameter, tube spacing, crossflow velocity, fuel-jet velocity, and jet-to-crossflow momentum ratio. The local map coordinates should include flame penetration distance relative to the tube exit, R_L/D_e, R_W/D_e, recirculation-zone-to-shear-layer HRR ratio, principal extensive strain rate relative to extinction, mixture-fraction displacement from the jet centerline, and pressure/velocity fluctuation amplitude. The present Case B occupies a stable region of this map: the flame branches remain downstream of the tube exits, the recirculation-zone

HRR is about 0.1 of the dominant shear-layer HRR, and the observed vortical structures redistribute the flame laterally rather than driving it upstream into the tube bundle.

More broadly, this chapter provides a physical framework for understanding flame stabilization in complex distributed-injection combustors. Its main contribution is not only to document that neighboring flame branches differ but also to explain why they differ and what that implies for combustor-level behavior. By showing how nominally regular injector arrays generate locally distinct stabilization pathways, the analysis connects global combustor performance to the underlying local fluid-chemistry interactions. The same coupled mechanisms–nonuniform mixing, confinement-induced flow redistribution, branch interaction, and local strain sensitivity–are expected to govern flame organization in more complex staged hydrogen combustion systems.

CHAPTER 5

Kinetic Uncertainty in Complex Reacting Systems

5.1 Introduction

The uncertainty analysis in this chapter is built on the same resolution regime used in the detailed-flow chapters. The AMReX fields are treated as implicit-LES/resolved-large-eddy reacting-flow fields: the sampled thermochemical states come from resolved flame fronts, shear layers, recirculation zones, and Lagrangian trajectories, while sub-filter turbulence below the local AMR spacing is not separately propagated through the chemistry-uncertainty model. Consequently, the UQ results quantify kinetic sensitivity of the resolved reacting states and should be interpreted as branch- and state-specific robustness diagnostics, not as a complete uncertainty budget for every unresolved turbulent fluctuation.

The previous chapters examined flame stabilization in complex hydrogen-fueled configurations primarily through flow-field and flame-structure diagnostics, including branch topology, recirculation, scalar dissipation, strain, and residence-time effects. These analyses established the fluid-mechanical structure of the flame, but they also pointed to a broader conclusion: flame stabilization in these systems is sustained only where the local thermochemical state created by mixing and transport remains compatible with finite-rate chemical processes that can maintain heat release against mixing and strain effects. This point is especially important in complex configurations, where the same global flame regime can contain locally different balances among mixing, residence time, heat release, and radical production. Even with detailed finite-rate chemistry, the reaction model retains epistemic uncertainty because its rate parameters are constrained by incomplete and uncertain combustion data; accordingly, this uncertainty can be represented by a posterior covariance matrix in parameter space for each reaction [132; 133]. The implication is that chemistry is not merely a closure embedded within the simulation but is an active part of the flame stabilization mechanism itself. To isolate and interpret that chemical contribution more directly, this chapter adopts an Uncertainty Quantification (UQ) perspective to investigate kinetic uncertainty in a complex

combustion system. This use of perturbations as a diagnostic is consistent with the broader fluid-mechanics tradition of using controlled perturbation analysis to reveal the mechanisms that organize complex flows [134].

From this viewpoint, chemistry UQ is useful not only because it places uncertainty bounds on model predictions but also because it reveals how sensitive local flame behavior is to the underlying kinetic description. Uncertainty in rate parameters propagates into ignition tendency, reaction progress, radical production, and characteristic chemical time scales, thereby providing a measure of the chemical robustness of the flame under different flow conditions. This is particularly valuable in practical reacting systems, where deterministic simulations may reproduce the major flame structure while still obscuring how strongly the local solution depends on uncertain chemical pathways. More broadly, quantifying uncertainty from chemistry models is increasingly recognized as necessary for establishing the credibility of reacting-flow simulations [135; 136; 137; 138; 139]. Although substantial progress has been made in estimating uncertainty in reaction-rate parameters [140; 141; 142], the development of those uncertainties through reacting-flow calculations remains limited because of the computational cost [143; 144; 145; 146].

Prior studies have also explored UQ together with dimensionality-reduction strategies and response-surface approaches [147; 148; 149; 143; 150; 151; 152]. However, when reduced chemistry is used in practical CFD, an additional difficulty arises: uncertainty information is often available only for individual reactions or for a detailed mechanism, not for the reduced mechanism actually used in the simulation. Since mechanism reduction may eliminate pathways, introduce lumped reactions, or rely on steady-state assumptions, there is generally no one-to-one correspondence between the uncertainty model of the detailed mechanism and that of the reduced mechanism. Some previous efforts in this direction have addressed parts of this problem. For example, Oh et al. [153] proposed a hybrid response-surface network for inverse UQ using a neural-network-based treatment of kinetic-rate uncertainty constrained by ignition-delay data, while Su et al. [152] quantified the uncertainty of the kinetic parameters during the reduction of the mechanism by combining sensitivity and active subspace analyses with a PCE surrogate and introducing a transition state to separate the changes due to the truncation of the parameters from the reaction coupling. Notably, however, these prior studies typically assume independent rate-parameter uncertainties, i.e., a diagonal covariance with no cross-correlations. That assumption simplifies the problem, but it does not retain the correlated uncertainty structure available in detailed chemistry models and, therefore, limits transferability across coupled sub-mechanisms.

To address this gap, the first framework used in this dissertation constructs uncertainty information around the reduced-space operating states already produced by a reacting-flow

simulation, rather than relying on repeated ensemble simulations. The procedure proceeds in two steps. First, reduced-manifold simulation states are reconstructed uniquely in the full detailed-composition space by initializing trajectories at the unburnt mixing state and integrating along the reaction mapping until the target progress-variable condition is reached. Second, correlated perturbations drawn from the covariance matrix of the detailed mechanism are propagated along those reconstructed detailed reaction trajectories. In this way, detailed-mechanism uncertainty is transferred to reduced-space operating points, producing spatially resolved variability estimates for chemistry-controlled quantities without requiring prohibitively expensive full-field uncertainty propagation. This framework provides a tractable means of identifying where chemistry-driven uncertainty materially affects a practical flame simulation and where reduced-mechanism predictions may depart from the detailed-mechanism reference.

A second and complementary framework addresses a different but closely related limitation. Even if uncertainty can be propagated from a detailed mechanism to local reacting states, the reduced mechanism used in practical simulations still often lacks a consistent description of its own uncertainty. To overcome this, a covariance-transfer and refinement procedure is introduced to construct an uncertainty model directly for the target reduced mechanism, starting from the correlated covariance matrix available for a detailed mechanism. Reactions shared between the detailed and reduced mechanisms are mapped directly, while effective uncertainty factors are assigned to reduced mechanism reactions that do not have a one-to-one counterpart in the parent mechanism. The resulting reduced covariance is then treated as a prior and refined through variational-inference-based regression using selected targets. The value of this second framework is that it moves the analysis beyond state-conditioned propagation alone and provides a practical uncertainty model for the reduced chemistry employed in reacting-flow calculations.

These two frameworks, therefore, serve different purposes in the present dissertation. In the first approach, hereafter referred to as the state-reconstruction UQ method, detailed species compositions are recovered from reduced thermochemical information by using the local state together with the conserved mixture fraction and reaction progress. After that, correlated kinetic uncertainty is propagated along the reconstructed trajectories. Its role is to evaluate chemistry-controlled trajectory measures, such as the equilibrate timescale, and thereby clarify reaction-path behavior and sensitivity in selected regions of the flow. For the second framework, termed as the covariance-transfer UQ method, a covariance model is first constructed and refined directly for the target chemistry used in the simulation, and that uncertainty description is then used to quantify local variability in reaction-zone quantities, particularly radical-production metrics such as OH production, under the strain–mixing

environments sampled by the flame.

The present chapter examines kinetic uncertainty in complex reacting systems using these two complementary uncertainty methods. The state-reconstruction UQ method is applied to the multi-tube micromixer, where reconstructed detailed states are used to evaluate uncertainty in chemistry-controlled trajectory quantities and to interpret reaction-path sensitivity within the stabilizing flow field. The covariance-transfer UQ method is applied to hydrogen transverse jets in crossflow, where a covariance-transfer and refinement procedure is used to construct an uncertainty description for the reduced mechanism employed in the simulation, enabling a local analysis of uncertainty in reaction-zone quantities.

5.2 State-reconstruction UQ method

The state-reconstruction UQ approach is based on a mapping between the reduced and detailed thermochemical spaces. To quantify uncertainty in the reduced space while using rate uncertainty from the detailed mechanism, a two-step procedure is used here: (i) reconstruction—map reduced-manifold states into the full composition space; (ii) sampling—integrate detailed reaction trajectories with perturbed rate coefficients drawn from the detailed mechanism's covariance matrices. This propagates parametric uncertainties and evaluates their impact on key trajectory targets in the reduced space. Reconstruction follows the attracting-manifold assumption (cf. ICE-PIC [154]); however, unlike ICE–PIC, here the trajectories are anchored at an unburnt mixing state defined by a conserved mixture fraction and are integrated forward along the reaction mapping until the progress variable reaches the target state, ensuring a unique mapping. This eliminates intermediate search steps, improving efficiency while preserving elemental conservation and manifold invariance (see Fig. 5.1).

This study assumes a gas-phase mixture (ϕ_g) of n_s chemical species composed of n_e elements ($\mathbf{E}$ is the elemental matrix) in a closed, homogeneous, and ideal gas reacting system. The thermochemical state of the mixture (at any time) is completely characterized by the pressure p, the temperature T, and the n_s-vector χ of the specific moles of the species, $\phi_g = (p, T, \chi)$. If p and T are held constant, the state is given by χ. Due to chemical reactions, the composition $\chi(t)$ evolves in time t according to the set of ordinary differential equations (ODEs) as $\frac{d}{dt}\chi(t) = \mathbf{S}_\Psi(\chi(t))$ (1), where $\mathbf{S}_\Psi \in \mathbb{R}^{n_s}$ is the vector of chemical production rates of the detailed mechanism (Ψ). A similar equation can be written using the production rate vector of the reduced mechanism (ξ), $\mathbf{S}_\xi \in \mathbb{R}^{n_r}$. The production rate vector $\mathbf{S}$ satisfies: (1) *Elemental conservation*: $\mathbf{E}^\top \mathbf{S} = \mathbf{0}$, ensuring that atomic elements are conserved throughout the reaction; (2) *Reactivity*: The mixture remains reactive except at chemical equilibrium, i.e., $\|\mathbf{S}\| > 0$ for all $\boldsymbol{\chi} \neq \boldsymbol{\chi}^{eq}$; (3) *Thermodynamic consistency*:

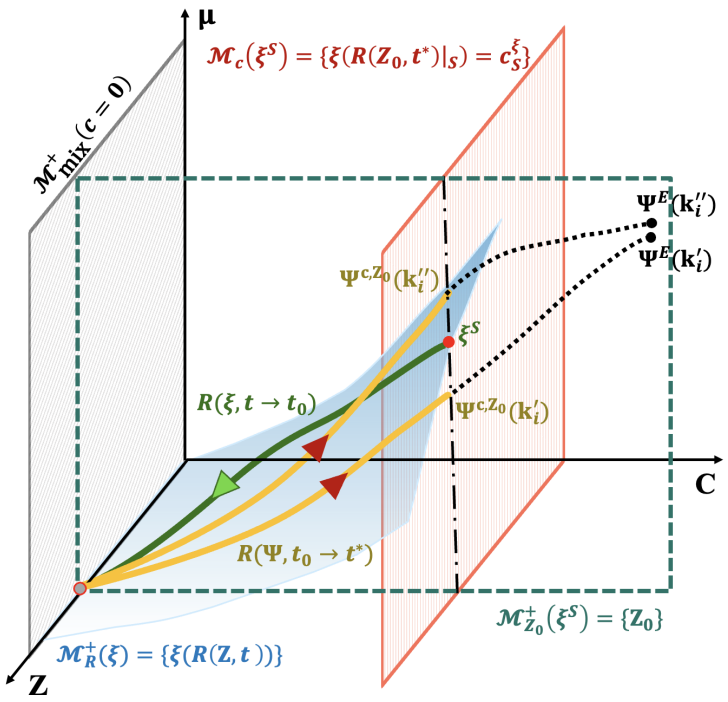


Figure 5.1: Conceptual sketch of the proposed trajectory mapping in composition space. The composition space is spanned by Z, c, and an unconstrained species μ (not frozen during reaction evolution). The blue-shaded surface $\mathcal{M}_R^+(\xi)$: Reduced-mechanism reaction manifold. Red-shaded plane $\mathcal{M}_c(\xi^S)$: iso-c manifold at state S for ξ. Green trajectory $R(\xi, t \to t_0)$: reconstruction from a given state S of ξ. Yellow trajectories $R(\Psi, t_0 \to t^*)$: forward integration of Ψ from Z_0 with perturbed reaction rate coefficients k_i towards $\mathcal{M}_c(\Psi^E)$, and reach the target composition $\phi^{\Psi^c}(k_i)$. Dashed black lines: relaxation of different reaction trajectories toward equilibrium (E).

The Gibbs free energy $G(\boldsymbol{\chi})$ is a strictly decreasing function along any reaction trajectory, $S^T \frac{dG}{dt} < 0$ for $\boldsymbol{\chi} \neq \boldsymbol{\chi}^{eq}$, with $\chi \to \chi^{eq}$ as $t \to \infty$; and (4) *Realizability*: Consistent with the law of mass action, the evolution of species concentrations is restricted to the realizable region of the composition space, i.e., $\chi_i(t) \geq 0,\ \forall i, t$. These properties have been discussed in detail in [155].

The two mechanisms ($\boldsymbol{\xi}$ and $\boldsymbol{\Psi}$) are subject to the following assumptions: $\boldsymbol{\xi} \subset \boldsymbol{\Psi}$, $\mathbf{S}_\xi = \mathbf{P}\,\mathbf{S}_\Psi$, and $\boldsymbol{\xi}, \boldsymbol{\Psi}$ contain the same set of elemental types, where $\mathbf{P}$ is a projection that ensures individual reaction rates remain consistent (values may vary) in both mechanisms. The term $\mathbf{R}(\chi, t)$ represents the reaction mapping, which is the solution to equation (1) at time t, starting from the initial condition χ. Given an unburned state $\phi_u^\xi = (p, T, \chi_u^\xi)$, the mixture fraction Z^ξ can be calculated as outlined in [111]. This state is then advanced along the $\boldsymbol{\xi}$ trajectory, and at time τ^ξ, a progress variable (c_g^ξ) is defined as a linear combination of selected species compositions. The initial state for $\boldsymbol{\Psi}$ can be defined as $\phi_u^\Psi = (p, T, \chi_u^\Psi(Z^\xi))$, where $\chi_u^\Psi(Z^\xi) = B\chi_u^\xi(Z^\xi)$ with $B \in \mathbb{R}^{n_s \times n_r}$ serves as the constant species map to reconstruct

the detailed species composition from $\chi^{(\xi)}(Z) \xrightarrow{B} \chi^{(\Psi)}(Z)$. The system $\boldsymbol{\Psi}$ is initialized on the corresponding unburnt mixing edge $\boldsymbol{\Psi}_0 = \boldsymbol{\Psi}_u(p, T\chi_u^{\Psi})$ and advanced along the detailed trajectory $t \mapsto \mathbf{R}(\boldsymbol{\Psi}_0, t)$ until the progress variable reaches the prescribed value c_g^{ξ}, i.e., $c_g^{\Psi}(\mathbf{R}(\boldsymbol{\Psi}_0, t^{\star})) = c_g^{\xi}$ (see Fig. 5.1). The resulting detailed composition $\boldsymbol{\Psi}^{\star} = \mathbf{R}(\boldsymbol{\Psi}_0, \tau^{\star})$ satisfies both mixture-fraction and progress-variable consistency, $Z(\boldsymbol{\Psi}^{\star}) = Z^{\xi}$ and $c(\boldsymbol{\Psi}^{\star}) = c_g^{\xi}$, and thus represents the reconstructed detailed state corresponding to the reduced coordinate $\boldsymbol{\phi}_g^{\xi}$. If $\boldsymbol{c}$ evolves monotonically along the trajectory—i.e., if $\mathbf{S}_{\psi}(\mathbf{R}(\boldsymbol{\Psi}_0, t))$ maintains a fixed sign—the root $\tau^{\star}$ is unique [154].

Uncertainty in reaction rates for $\boldsymbol{\Psi}$ is represented by sampling correlated Arrhenius parameters from a multivariate Gaussian distribution with covariance Σ_{Ψ}. For each reaction i, the normalized variables $x_{A,i} = \ln(A_i/A_{0,i})/\ln f_i$ and $x_{B,i} = (B_i - B_{0,i})/(T_{\mathrm{ref}} \ln f_i)$ describe perturbations in the pre-exponential factor and activation energy. The corresponding logarithmic rate variation is $x_i(T) = x_{A,i} - (T_{\mathrm{ref}}/T)x_{B,i}$, yielding $k_i(T) = k_{0,i}(T)\, f_i^{\,x_i(T)}$, with $\boldsymbol{x}_i = [x_{A,i}, x_{B,i}]^{\top}$. The joint parameter vector $\mathbf{X} = [\boldsymbol{x}_1^{\top}, \ldots, \boldsymbol{x}_I^{\top}]^{\top}$ follows $\mathbf{X} \sim \mathcal{N}(\boldsymbol{\mu}_{\boldsymbol{m}}, \boldsymbol{\Sigma}_{\boldsymbol{\Psi}})$, where $\boldsymbol{\Sigma}_{\boldsymbol{\Psi}}$ encodes correlations between A_i and B_i. Samples are drawn by $\mathbf{X}^{(s)} = \boldsymbol{\mu}_{\boldsymbol{m}} + \mathbf{L}\mathbf{z}^{(s)}$ with $\mathbf{L}\mathbf{L}^{\top} = \boldsymbol{\Sigma}_{\boldsymbol{\Psi}}$ and $\mathbf{z}^{(s)} \sim \mathcal{N}(0, \mathbf{I})$. Repeated sampling and integration of the kinetic model generate an ensemble of trajectories whose dispersion defines an uncertainty band (see Fig. 5.1). The covariance matrix must be symmetric and positive definite.

5.3 Covariance-transfer UQ method

The covariance-transfer UQ method is used in this dissertation to construct an uncertainty model for a reduced reaction mechanism starting from a detailed mechanism for which correlated kinetic-parameter covariance information is available. The main motivation is practical. In reacting-flow simulations, the chemistry model used in CFD or post-processing is often reduced for computational efficiency, while the most complete uncertainty information is typically available only for a larger parent mechanism. Because mechanism reduction can remove reactions, lump pathways, and modify the representation of coupled chemistry, the covariance information of the detailed mechanism cannot be applied directly to the reduced mechanism without additional modeling. The present method addresses this difficulty in two stages. First, covariance information is transferred from the detailed mechanism to the reduced mechanism to define a prior uncertainty model. Second, that prior is refined through Bayesian regression using ignition-delay time targets.

Let θ denote the uncertain kinetic parameters of the target reduced mechanism, and let y denote the observational quantity used for calibration, here taken as the ignition-delay time. The posterior probability density of the parameters, conditioned on the observations,

is given by Bayes' theorem.

$$p(\theta \mid y) = \frac{p(y \mid \theta)\, p(\theta)}{p(y)}. \tag{5.1}$$

In this expression, $p(\theta)$ is the prior distribution, which represents uncertainty in the kinetic parameters before using the calibration data; $p(y \mid \theta)$ is the likelihood, which measures how well a given parameter set reproduces the observed ignition delays; and $p(\theta \mid y)$ is the posterior distribution, which represents the updated uncertainty after conditioning on the data. For the nonlinear chemistry model considered here, direct evaluation of the posterior is not tractable because each likelihood evaluation requires a reactive simulation. For this reason, the posterior is approximated using variational inference. In this approach, a tractable trial distribution $q(\theta; \lambda)$ is introduced, and its parameters λ are selected so that q is as close as possible to the true posterior.

$$\lambda^* = \arg\min_{\lambda} D_{KL}\left(q(\theta;\lambda) \,\|\, p(\theta \mid y)\right), \tag{5.2}$$

which states that the variational approximation is chosen to minimize the Kullback–Leibler divergence from the true posterior. This minimization is equivalent to maximizing the Evidence Lower Bound (ELBO),

$$\lambda^* = \arg\max_{\lambda} \Big[E_q\Big[\log p(y \mid \theta)\Big] + E_q\Big[\log p(\theta)\Big] - E_q\Big[\log q(\theta;\lambda)\Big]\Big]. \tag{5.3}$$

The first term in Eq. (5.3) rewards parameter distributions that reproduce the calibration targets well; the second term keeps the inferred parameters consistent with the prior information, and the third term accounts for the entropy of the variational approximation. In the present work, the variational distribution is taken to be Gaussian,

$$q(\theta;\lambda) = \mathcal{N}(\mu, \Sigma), \tag{5.4}$$

so that the approximate posterior is represented by a mean vector μ and a covariance matrix Σ. This Gaussian form is particularly useful because it allows the parameter correlations to be retained while keeping the optimization tractable.

The starting point for the method is a detailed parent mechanism for which a correlated parameter covariance matrix is available. The covariance-transfer step constructs a prior uncertainty model for the target mechanism from the detailed-mechanism covariance information. This is carried out at the reaction level. Reactions are first identified that both possess uncertainty information in the parent mechanism and appear explicitly in the target mechanism. For these shared reactions, the corresponding uncertainty information is trans-

ferred directly. For target-mechanism reactions that do not have a one-to-one counterpart in the parent mechanism, such as lumped reactions or reactions absent from the detailed mechanism, an effective uncertainty factor is assigned on the basis of the most closely related reactions in the parent mechanism. The resulting reduced covariance matrix is then taken as the prior covariance for the target mechanism, so that $p(\theta) = \mathcal{N}(\mu_{\mathrm{pr}}, \Sigma_{\mathrm{pr}})$, where μ_{pr} is centered at the nominal parameter values of the target mechanism and Σ_{pr} is the covariance matrix obtained from the covariance-transfer procedure. This prior supplies the initial uncertainty description used in the subsequent regression step.

Once the prior has been constructed, it is refined through nonlinear Bayesian regression. The calibration targets are ignition-delay times generated with the detailed mechanism over a broad range of thermochemical conditions,

$$T \in [900, 2100]\ \mathrm{K}, \qquad P \in [1, 15]\ \mathrm{atm}, \qquad \phi \in [0.1, 2.0]. \tag{5.5}$$

These data serve as the observation vector y in the Bayesian formulation. The forward model for the regression is written as

$$y = g(\theta) + \varepsilon, \tag{5.6}$$

where $g(\theta)$ denotes the ignition-delay predictions obtained by evaluating the target mechanism in Cantera for a given parameter vector θ, y is the selected target or observations, and ε represents the noise or error term. In practice, each evaluation of $g(\theta)$ requires a full Cantera ignition-delay simulation over the prescribed set of conditions. The additive error or noise term in the regression model is introduced to define a probabilistic likelihood and to account for the residual mismatch between the reduced-mechanism prediction and the calibration targets, including numerical error and model-form discrepancy arising from mechanism reduction. Following the source study, the likelihood is defined in log space using a relative-error model,

$$\log p(y \mid \theta) \propto -\frac{1}{2\sigma_{\mathrm{rel}}^2} \sum_i \left[\log y_i - \log \hat{y}_i(\theta)\right]^2, \tag{5.7}$$

where $\hat{y}_i(\theta)$ is the predicted ignition delay for the ith condition, and σ_{rel} is the prescribed relative noise level. The use of log space is important because ignition-delay times span a wide dynamic range, and a logarithmic formulation, therefore, emphasizes relative agreement rather than absolute error. With the prior and likelihood defined, the ELBO in Eq. (5.3) becomes the objective function used to infer the posterior Gaussian parameters μ and Σ.

After convergence, the refined posterior approximation is written as

$$\theta' \sim \mathcal{N}(\mu', \Sigma'). \tag{5.8}$$

The posterior mean μ' represents the updated central estimate of the reduced-mechanism parameters, while the posterior covariance Σ' represents the updated uncertainty and parameter-correlation structure after conditioning on the ignition-delay targets.

A practical difficulty in this regression is that the forward model $g(\theta)$ is evaluated through a black-box Cantera simulation, so the ELBO does not have a convenient analytic gradient with respect to the variational parameters. An obvious initial option is finite-difference gradient evaluation, in which the variational parameters are perturbed, and the corresponding change in the objective is used to approximate the gradient. However, in the present problem, this approach is not sufficiently robust. Because ignition-delay prediction requires stiff ODE integration, finite-difference gradients can be sensitive to numerical noise and subtraction cancellation, especially when the perturbation magnitude is small. In addition, the cost grows rapidly with parameter dimension because multiple objective evaluations are required for each gradient estimate. These difficulties motivate the use of simultaneous-perturbation stochastic approximation (SPSA) for gradient estimation [156; 157].

Let x denote the vector of variational parameters and define $F(x) = -\text{ELBO}(x)$. The optimization is then recast as a minimization of $F(x)$. At iteration k, SPSA perturbs all components of x simultaneously using a random direction vector Δ_k and evaluates the objective at two symmetrically perturbed points.

$$y_k^+ = F(x_k + c_k\Delta_k), \qquad y_k^- = F(x_k - c_k\Delta_k), \tag{5.9}$$

where c_k is the perturbation scale. From only these two evaluations, the gradient estimator is formed as

$$\hat{g}_{k,i} = \frac{y_k^+ - y_k^-}{2c_k\Delta_{k,i}}. \tag{5.10}$$

The key advantage is that the cost of the gradient estimate does not increase in the same way as coordinate wise finite differences, making SPSA more suitable for a noisy, high-dimensional black-box objective. To further reduce estimator variance, the gradient can be averaged over multiple independent perturbations.

$$\hat{g}_k^{(M)} = \frac{1}{M}\sum_{m=1}^{M} \hat{g}_k^{(m)}. \tag{5.11}$$

The resulting averaged SPSA gradient is then supplied to the optimizer to update the varia-

tional parameters iteratively until the ELBO converges. In this way, the regression proceeds by repeatedly sampling from the current Gaussian approximation, evaluating the corresponding ignition-delay predictions through Cantera, estimating the ELBO and its gradient, and updating the mean and covariance of the variational posterior. Additional implementation details and convergence behavior of the variational optimization are provided in Appendix C.

After regression, the posterior covariance Σ' provides a refined uncertainty description for the target reduced mechanism. This posterior covariance can then be used to generate parameter samples and propagate uncertainty through the reduced chemistry model in subsequent reacting-flow analyzes. In the present dissertation, this method is applied to the hydrogen jet-in-crossflow configuration, where the refined reduced-mechanism uncertainty model is used to examine local uncertainty in chemistry-sensitive flame quantities.

5.4 State-reconstruction UQ for Multi-tube Combustor

In this section, the first proposed two-step procedure is further evaluated by the Multi-tube Combustor. Partially premixed combustion and complex fluid strain effects from geometric influences on chemical timescales and reaction pathways are investigated through this UQ analysis. Here, the FFCM-2 mechanism, along with its covariance matrix [132; 133], will be used as the basis for the UQ methods described in Section 5.2.

The numerical simulation models a multi-tube combustor with a subsonic reacting flow, where a flame, potentially under a partially-premixed combustion mode, is anchored at the exit region of a tubular bundle [158]. This simulation has been validated against experimental data, and details of the computational domain are provided in Chapter 4. Case B, corresponding to the pure hydrogen fuel configuration, is selected for the present UQ analysis. Two primary wall injectors, angled at 90° introduce hydrogen fuel within each tube element, upstream of the combustion chamber. Vitiated air at 758 K and 162 m/s enters the tubular bundle following the experimental setup. Here, the chamber region of the numerical results is extracted only along the mid-section plane B (Fig. 5.2). Upstream fuel injection induces mixture stratification that, along with evolving recirculation zones, modulates the flame front. This coupling promotes periodic detachment of localized reaction pockets and drives oscillatory flame dynamics, making this region a key focus for further investigation. The simulations are performed using a fully compressible Navier-Stokes solver [72], employing an H_2-Air mechanism with 9 species and 21 reactions [11]. In this study, cells with $T >$ 900 K are termed chemically "active cells" and are considered in the analysis; however, if the cell has a fuel concentration near zero, it is discarded.

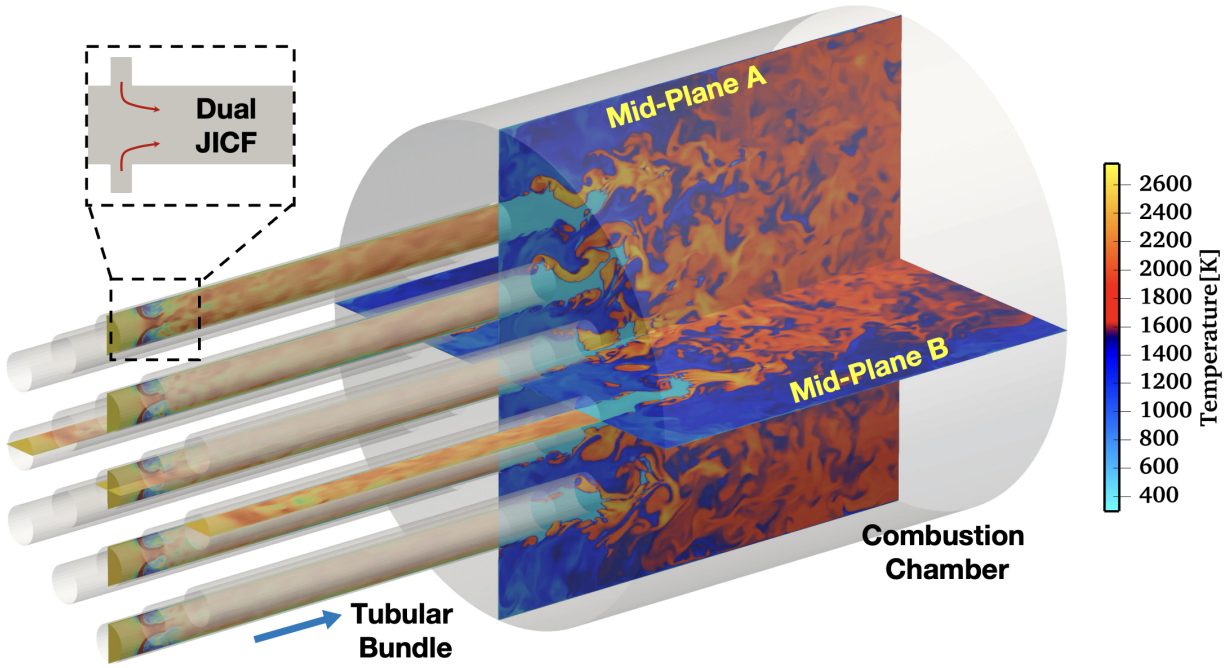


Figure 5.2: Instantaneous snapshot on the combustor mid-plane showing temperature. Blue arrows indicate the flow direction of the oxidizer stream. Red arrows depict fuel stream issuing perpendicular into the oxidizer stream (inset).

5.4.1 Trajectories with FFCM-2 for H_2 fuel

In current and later sections, the FFCM-2 mechanism, along with its covariance matrix [132], will be used as a basis to study the H_2 fuel reactions. Since this is a nontrivial task, first, to verify the applicability of FFCM-2 to hydrogen-fueled conditions, additional details are provided in Appendix B. Further, to verify that the transferred uncertainty does not introduce spurious variability, we compare it against direct uncertainty propagation with the original FFCM-2 mechanism and covariance matrix in a representative counterflow flame; the results are presented in Appendix B.1. To understand the species reconstruction method and the generation of different reaction trajectories, one cell from the numerical simulation is analyzed here. First, following Section 5.2, an unburnt mixing state is reconstructed. Next, reaction trajectories were computed with perturbed kinetics defined by a scalar multiplier $s = f^{x_k}$, where x_k are components of the joint parameter vector $\mathbf{X} \sim \mathcal{N}(0, \mathbf{\Sigma_\Psi})$ [132]. Using Cantera [123], perturbations uniformly rescale reaction rates for $\mathbf{\Psi}$: pressure-independent reactions set $k \to s\,k$; falloff reactions use $A_0 \to sA_0$ and $A_\infty \to sA_\infty$, preserving the reduced pressure and the falloff shape; The PLOG type applies the same s to every node's A_m. Third-body efficiencies were modified as $[M]_{\text{eff}} = \sum_s \eta_s[s]$, shifting the pressure dependence (and the low-pressure branch) without altering the high-pressure limit. The ensemble of 500 different

sampled reaction trajectories for a representative cell is shown in Fig. 5.3. To map the results to the simulation manifold $\boldsymbol{\xi}$, the reaction process was evaluated using the progress variable $C = \mathrm{Y_{OH}} + \mathrm{Y_{H_2O}}$, which is defined based on the original cell state. The unconstrained coordinate (representing species that are not frozen during reaction evolution) is defined as the mass fraction of the intermediate species. The intermediate species OH begins with a low radical concentration and shows a flat increase at low reaction progress levels. As the reaction progresses, the path remains on a long, gently curved low-$\mathrm{Y_{OH}}$ branch for most of its extent. Near the high-C end, the trajectory turns sharply and rises almost vertically, indicating a rapid increase in $\mathrm{Y_{OH}}$ with comparatively small changes in C and Z. At the same time, the trajectory for H_2O_2 begins with an almost vertical rise at relatively low C, indicating a rapid build-up of H_2O_2 while C changes only weakly; as C increases into an intermediate range, the path reaches a peak (or near-plateau) with $\mathrm{Y_{H_2O_2}} \approx Y_{\max}$, after which it transitions smoothly into a long declining tail in which $\mathrm{Y_{H_2O_2}}$ decreases gradually as C continues to increase. In contrast to $\mathrm{Y_{OH}}$, which tends to exhibit a delayed and abrupt jump, the evolution of $\mathrm{Y_{H_2O_2}}$ is more progressive and continuous, following a build-up $\rightarrow$ peak $\rightarrow$ decay pattern. The thermochemical states at the intersection point of each reaction trajectory with the plane $C = c^{\xi}$ are used for the next analysis.

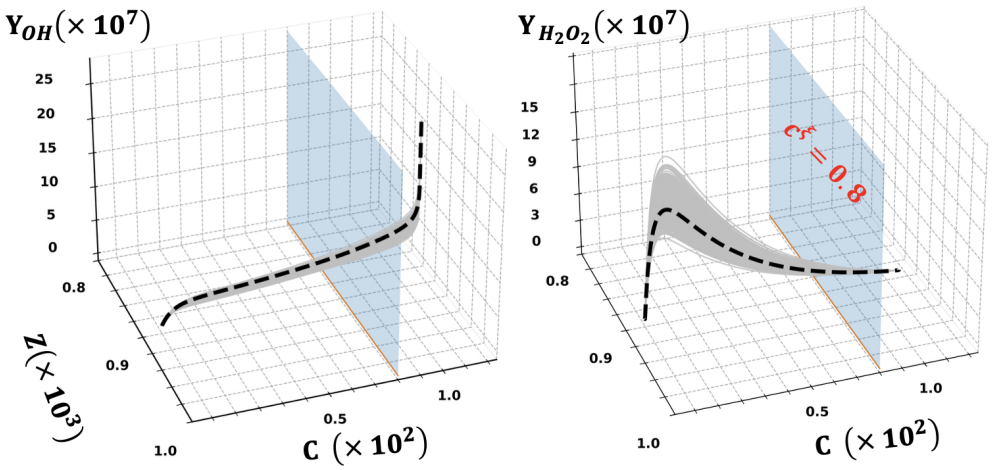


Figure 5.3: Ensemble of one-cell reaction trajectories in C, Z, μ space, and two different un-constrained coordinate definition. Gray curves span different sample of reaction kinetics; one typical trajectory is emphasized with a thick black dashed line. The blue plane marks $C^{\xi} = 0.8$ constraint.

5.4.2 Local Chemical Timescales and Reaction Pathways

In order to assess the UQ framework, we utilize the following performance metric: we define a time $\boldsymbol{\tau_C}$, which is the time taken by a local unburnt fuel-air mixture (based on the mixture

fraction) to reach the local thermodynamic state characterized by the progress variable. The initial conditions are reconstructed using Z^{ξ} from each computational cell in the domain, and the integration is carried out in a constant-volume reactor for $\mathbf{\Psi}$, similar to the analyses presented above for the mapping procedure. A total of 100 samples are generated for each of the 90000+ cells. Fig. 5.4 shows this mean chemical timescale ($\widetilde{\tau_C}$) on the combustor mid-plane B. Interactions between the discrete jet flames (entering the combustion chamber) and the recirculation flow generate order-of-magnitude variations in $\widetilde{\tau_C}$, reflecting ongoing mixing between mixtures of different local compositions. Along the flame front, the chemical timescale exhibits pronounced spatial variability. Regions characterized by near-stoichiometric conditions display short chemical timescales on the order of 10^{-6} s, indicative of rapid reaction kinetics, consistent with the behavior observed for the non-premixed diffusion flame front discussed later in the current section. In contrast, portions of the flame front just downstream of the tube exit are associated with substantially longer chemical timescales, reaching $\mathcal{O}(10^{-2})$ s, which can be attributed to fuel stratification within the main flow. This wide range of chemical timescales along the flame front underscores the partially premixed nature of the combustion process, wherein both kinetically fast, diffusion-controlled reactions and slower, mixing-limited reactions coexist. Further downstream, the characteristic chemical timescale $\widetilde{\tau_C}$ decreases to approximately 10^{-7} s, consistent with a flow region dominated by fully reacted, post-flame products and rapid radical recombination kinetics occurring under relatively low local strain rates. In contrast, within the inter-jet recirculation zone in the near vicinity of the tube exit, interactions between the jet and the recirculating flow generate strong spatial variations in strain rate and enhance local fuel stratification, leading to elevated chemical timescales and a significantly broader distribution. In this region, the chemical timescale spans several orders of magnitude, ranging from ~ 0.2 s to 10^{-4} s, reflecting the combined effects of strain-rate-induced residence-time reduction and mixing-limited chemistry.

We extend the UQ analysis to the time-to-equilibrium. Each cell is assumed to relax via a constant-UV (internal energy and volume) equilibration process. We note that other systems may require different equilibration assumptions (e.g., UV vs. HP). For every cell, we integrate a constant-volume reactor with perturbed reaction rates and record the time at which T=T_{UV}, repeating this for 100 samples. Figures 5.5 and 5.6 show the local temperature T as a function of mixture fraction Z, with marker color denoting the normalized variability of the local timescale $\widehat{\tau}_E = \sigma_{\tau_E}/\widetilde{\tau}_E$. The two panels correspond to different regions—the flame front and the recirculation zone—and exhibit distinct thermochemical coverage and scatter. The flame-front samples span a broad range of mixture fractions (extending to substantially higher Z) and reach higher temperatures (up to ~ 2500 K), indicating strong heat release and

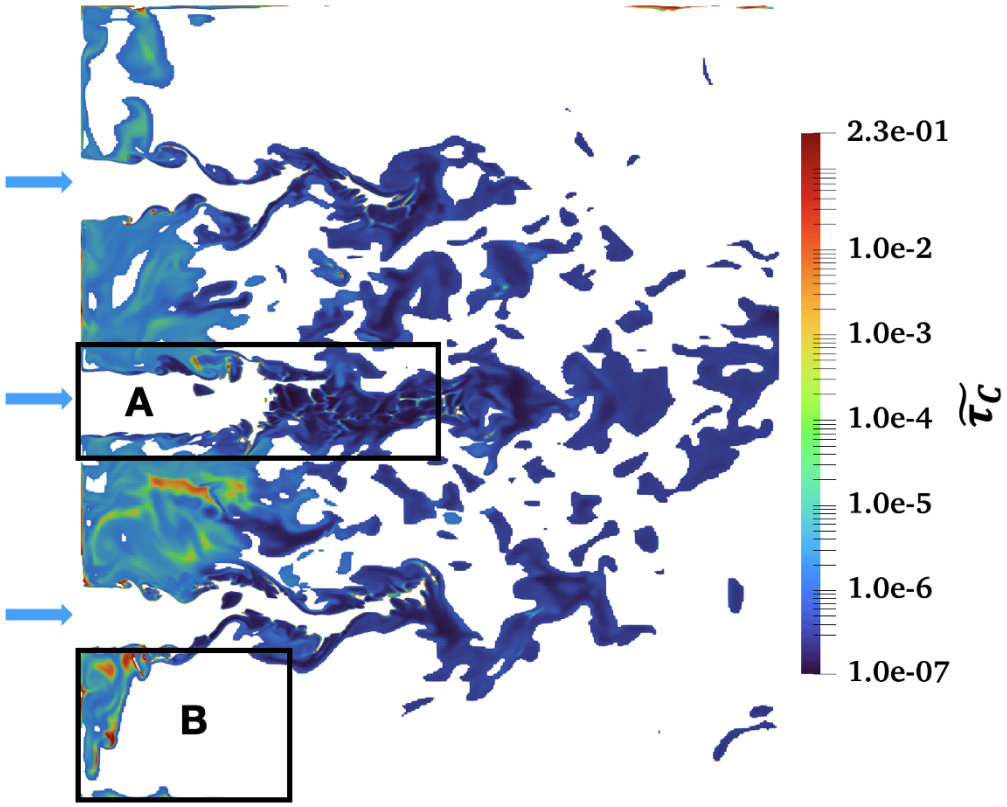


Figure 5.4: Instantaneous snapshot on the combustor mid-plane B showing time scale $\widetilde{\tau_C}$ in log-scale computed from Ψ. Blue arrows indicate the flow direction of the partially premixed stream. Region A represents the flame front, while region B represents the recirculation zone.

intermittent exposure to richer and near-stoichiometric pockets. Correspondingly, this plot shows substantial spread in T at fixed Z and a wider distribution of $\widehat{\tau}_E$, reflecting stronger local stratification and more intense, unsteady reaction. By comparison, the recirculation-zone samples are confined to leaner conditions (lower Z) and a narrower temperature range (peaking near ~ 2100 K). The points cluster more tightly along a mixing/ignition trajectory, consistent with enhanced dilution by recirculated products, milder reaction, and reduced thermochemical intermittency relative to the flame front.

Both on the flame front and in the recirculation zone, $\widehat{\tau}_E$ varies by approximately 2%–18%, with the largest dispersion occurring in the low-to-intermediate temperature regime corresponding to induction and the onset of heat release. In this regime, we found that two chain-propagation reactions, $\mathrm{H} + \mathrm{O_2}, (+\mathrm{M}) \rightleftharpoons \mathrm{HO_2}, (+\mathrm{M})$ (R1) and $\mathrm{H_2} + \mathrm{OH} \rightleftharpoons \mathrm{H} + \mathrm{H_2O}$ (R2), together with the chain-branching reaction $\mathrm{H} + \mathrm{O_2} \rightleftharpoons \mathrm{O} + \mathrm{OH}$ (R3), govern the approach to equilibrium.

Consistent with findings in [159], under fuel-lean conditions, the chemical state is particularly sensitive to R2. Moreover, as shown in [160], the IDT exhibits strong sensitivity to R1

in the low-temperature regime near 1000 K. In addition, as discussed in [161], the R1 pathway is strongly pressure dependent and is enhanced at elevated pressures, thus isolating H atoms into HO_2 and reducing their availability for the chain-branching pathway R3, which in turn effectively modulates the overall branching propensity. In the intermediate-temperature range, the branching reaction R3 is frequently identified as one of the most sensitive elementary steps [162]. Collectively, these findings suggest that the elevated variability in $\widehat{\tau}_E$ in the low-to-intermediate temperature regime is attributable to the initiation and competition of branching-related chemistry and its pressure-modulated coupling to propagation pathways.

A key inference that may be drawn from the analysis is that pronounced deviation in the low-to-intermediate temperature regime is expected to influence ignition-kernel evolution in the presence of relatively cooler and stratified reactant streams. This is important for studies focused on kernel growth or even auto-ignition behavior, as this may alter early transient flame development. During the initial phase of the simulation, when mixing and thermochemical perturbations are small but consequential, modest fluctuations in local composition and temperature can therefore yield disproportionately large changes in the effective chemical timescale. At elevated temperatures, the hydrogen chemistry considered here exhibits comparatively similar pathway evolution, even in hot states; consequently, $\widehat{\tau}_E$ remains bounded (typically $\lesssim 0.1$).

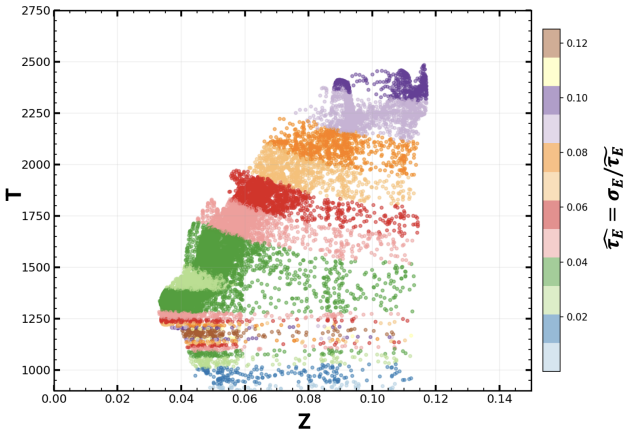


Figure 5.5: Scatter plot of T versus Z colored by $\widehat{\tau}_E$ on the flame front (Region A in Fig. 5.4).

When comparing these results along low and high T regime, the variation in the chemical timescale at low temperatures is dictated by R1, where radical removal tends to control the formation/consumption of HO_x and therefore uncertainties in temperature/pressure can strongly amplify the deviation in timescales [163]. However, as T increases, the dominant flux shifts toward the chain-branching step $H + O_2 \rightleftharpoons O + OH$ (R3) as tested in Cantera [123]; indeed, Li et al. [164] reported that above $\sim$ 2000 K, the competing association channel

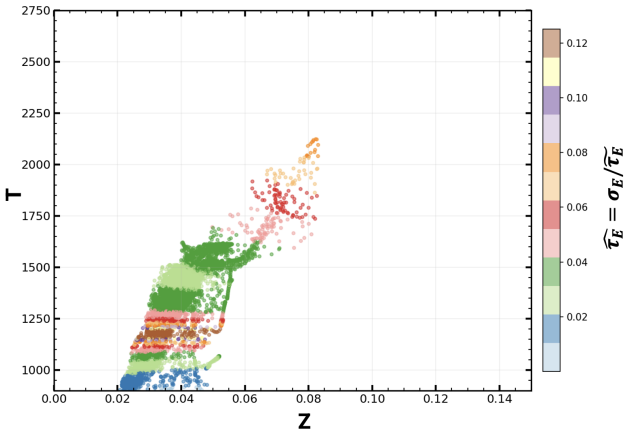


Figure 5.6: Scatter plot of T versus Z colored by $\widehat{\tau}_E$ inside recirculation zone (Region B in Fig. 5.4).

becomes insignificant relative to this branching reaction. However, predictions of hydrogen oxidation (e.g., ignition delay and flame propagation) can still exhibit appreciable sensitivity to the remaining high-T controlling reactions and their rate parameters (most notably $H + O_2 \rightarrow O + OH$ and coupled HO_x pathways) [163]. Therefore, the smaller variation observed at high T should be interpreted primarily as an artifact of the current uncertainty model (i.e., the assumed FFCM-2 covariance matrix $\mathbf{\Sigma}$ and its correlations/weights, which can decrease variance propagation when high-T branching-rate parameters are treated as strongly correlated), rather than as a physical statement that hydrogen kinetics are "not sensitive" at high temperatures.

5.5 Flame Stabilization and Dynamics for Hydrogen Enriched Jet Flames

Before introducing UQ, the hydrogen-enriched jet-in-crossflow flames were first analyzed deterministically over a range of jet momentum ratios and hydrogen contents by volume (as listed in Table 3.1) to establish the baseline flame-stabilization behavior and unsteady flame dynamics of the system. The purpose of this analysis is to determine how the global flame structure, branch topology, local strain environment, and temporal response change with operating conditions, thereby distinguishing the effects of the flow field from those associated with fuel composition. This deterministic characterization provides the physical foundation for the subsequent UQ study, since the role of kinetic uncertainty can only be interpreted clearly after the baseline stabilization mechanisms and flame dynamics have been identified.

5.5.1 Global Flame Structure

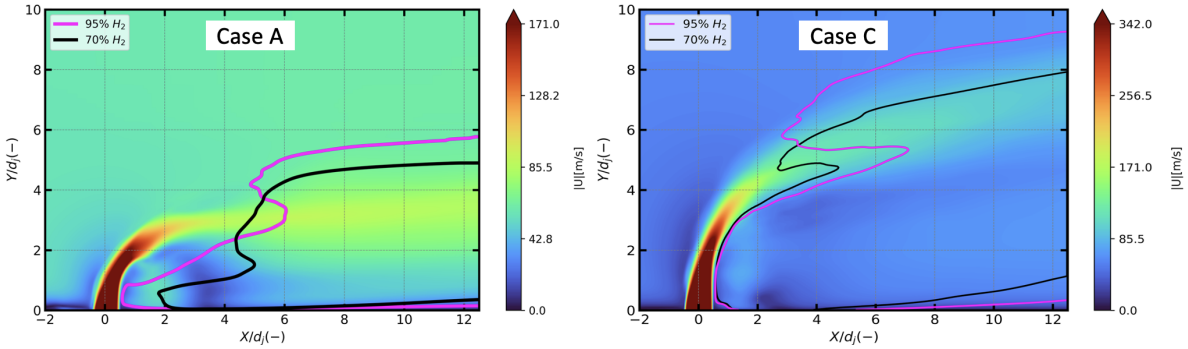


Figure 5.7: Temporally averaged velocity magnitude for the different cases, with the isoline of Y_{OH} for the 70% and 95% H_2 by volume cases indicating the flame shape.

In a previous study[165; 166], the 70% H_2 by volume cases were validated against experimental results. This study focuses on the comparison of flame shapes as the hydrogen content by volume changes, as shown in Fig 5.7. When the hydrogen content by volume was increased to 95%, the fuel density decreased significantly. To ensure comparable jet characteristics across different fuel compositions, the jet momentum ratio (J) was held constant, necessitating an increase in jet velocity for the lower-density hydrogen-rich mixture. Under this constraint, the jet trajectory remained consistent across the different hydrogen-by-volume cases. However, the lower density in the 95% hydrogen-by-volume case led to greater fluctuations in the fuel stream. This instability contributed to a broader flame spread, driven by the increased volumetric heat release associated with the higher hydrogen content. Notably, the flame continued to exhibit a dual-branch structure, similar to that in the 70% hydrogen-by-volume case. While the flame front shifted slightly upstream, the location where the two branches connected exhibited both upstream and downstream movement. To further investigate the dynamic behavior of the flame under these conditions, a time-resolved visualization of the flame branches is presented in the following sections.

5.5.2 Strained Flame Front

To visualize the coupled roles of mixing, strain, and chemistry, Fig. 5.8 overlays the flame front on the field of normalized scalar dissipation rate and additionally includes the stoichiometric mixture-fraction contour, $Z = Z_{\mathrm{st}}$ (black line). This combined view clarifies (i) where the flame can persist relative to local quenching/under-mixing limits and (ii) how closely the reacting layer follows the nominal diffusion-flame stoichiometric surface.

The colormap shows the normalized scalar dissipation rate, $\hat{\chi}$, defined as:

$$\hat{\chi} \;=\; \frac{\chi}{\chi_{\mathrm{st}}^{\mathrm{ext}}}, \tag{5.12}$$

where $\chi_{\mathrm{st}}^{\mathrm{ext}}$ is the stoichiometric scalar dissipation rate at extinction obtained from a one-dimensional counterflow calculation in Cantera [123]. This normalization provides a physically meaningful chemical reference: values $\hat{\chi} \sim \mathcal{O}(1)$ correspond to local mixing/strain intensities comparable to the laminar extinction limit, enabling direct comparisons across cases.

Across all cases, the flame front does not coincide with the maximum-$\hat{\chi}$ regions. Instead, the flame front consistently resides on the immediate low-$\hat{\chi}$ side of the high-$\hat{\chi}$ layer that forms along the primary shear/mixing interface. This indicates stabilization where mixing remains sufficiently strong to bring the mixture toward reactive compositions, yet the local scalar dissipation has relaxed enough for chemical reaction to compete with strain. In the regions of very large $\hat{\chi}$ (orange–magenta), no flame is observed, consistent with conditions approaching or exceeding the extinction reference. Conversely, regions of very small $\hat{\chi}$ (blue–gray) are also largely flame-free; although strain is weak there, scalar gradients (and thus interdiffusion toward reactive compositions) are minimal, so the mixture remains close to the unmixed streams. The flame front therefore occupies an intermediate range of χ, bounded by over-strained (high-$\hat{\chi}$) and under-mixed (low-$\hat{\chi}$) zones.

The Z_{st} contour further shows that the lifted branch behaves predominantly as a diffusion flame: the flame front closely follows the stoichiometric surface as it threads along the mixing layer, and the high-$\hat{\chi}$ band intersects the Z_{st} contour in the upstream stabilization region. Notably, the flame front typically appears slightly displaced from the peak-$\hat{\chi}$ ridge and from the Z_{st} line, reflecting finite-rate effects and the fact that the instantaneous reaction zone is set by the local balance between strain effects and chemistry rather than by mixture fraction alone.

The momentum-flux ratio J sets the dominant changes in flame topology. Comparing $J = 1.96$ (Cases A7 and A9) with $J = 8.41$ (Cases C7 and C9) shows that higher J produces a broader and more contorted high-$\hat{\chi}$ layer and a more pronounced lifted/arched structure, consistent with stronger shear and enhanced turbulent mixing. In contrast, the lower-J cases remain more compact and closer to the lee-stabilized configuration, with a comparatively weaker and lower-lying high-$\hat{\chi}$ ridge. Despite these structural differences, the alignment of the lifted reaction zone with the stoichiometric surface remains robust: the lifted flame front tracks the Z_{st} contour and resides on the low-$\hat{\chi}$ side of the strongest dissipation.

An important exception is observed for the lee-stabilized branch in Case A9, where seg-

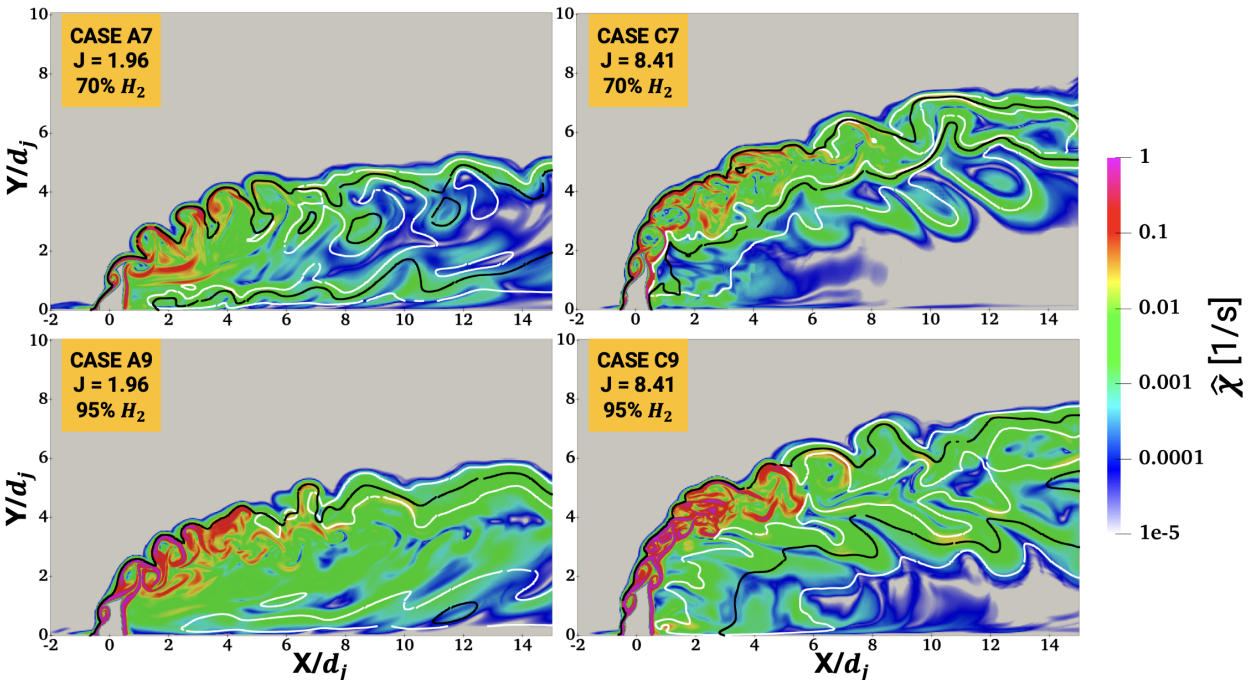


Figure 5.8: Instantaneous fields of normalized scalar dissipation rate $\hat{\chi} = \chi/\chi_{\mathrm{st}}^{\mathrm{ext}}$ (log scale) for different cases. The flame front is marked by an iso-contour of Y_{OH} at 10% of its peak value (white line), and the black line indicates the stoichiometric mixture-fraction contour $Z = Z_{\mathrm{st}}$ (black line).

ments of the flame front do not coincide with the nominal Z_{st} contour yet remain burning. This behavior is consistent with differential-diffusion effects in hydrogen flames. As a result, the reacting layer can appear on the fuel rich side of the nominal Z_{st} line while still attaining locally favorable conditions for reaction (i.e., an effectively closer-to-stoichiometric radical/enthalpy balance at the flame front). This is most evident in the near-wall/recirculation region, where residence time and differential diffusion can enrich the local fuel content and shift the apparent stoichiometric surface away from the inlet-based Z_{st}.

Overall, using $\hat{\chi}$ normalized by $\chi_{\mathrm{st}}^{\mathrm{ext}}$ together with the Z_{st} contour enables a more rigorous interpretation of stabilization: the flame persists where the flow provides sufficient mixing to reach reactive compositions (often near Z_{st}) while remaining below extinction-level scalar dissipation so that chemistry can overcome local strain.

5.5.3 Flame Edge Analysis

Figure 5.9 presents a comparative analysis of the flame front in chemical space using the Z and Y_{OH}. Scatter plot points, sampled at different times and a single location for each subplot, are compared against strained and unstrained flame solutions from Cantera [123]

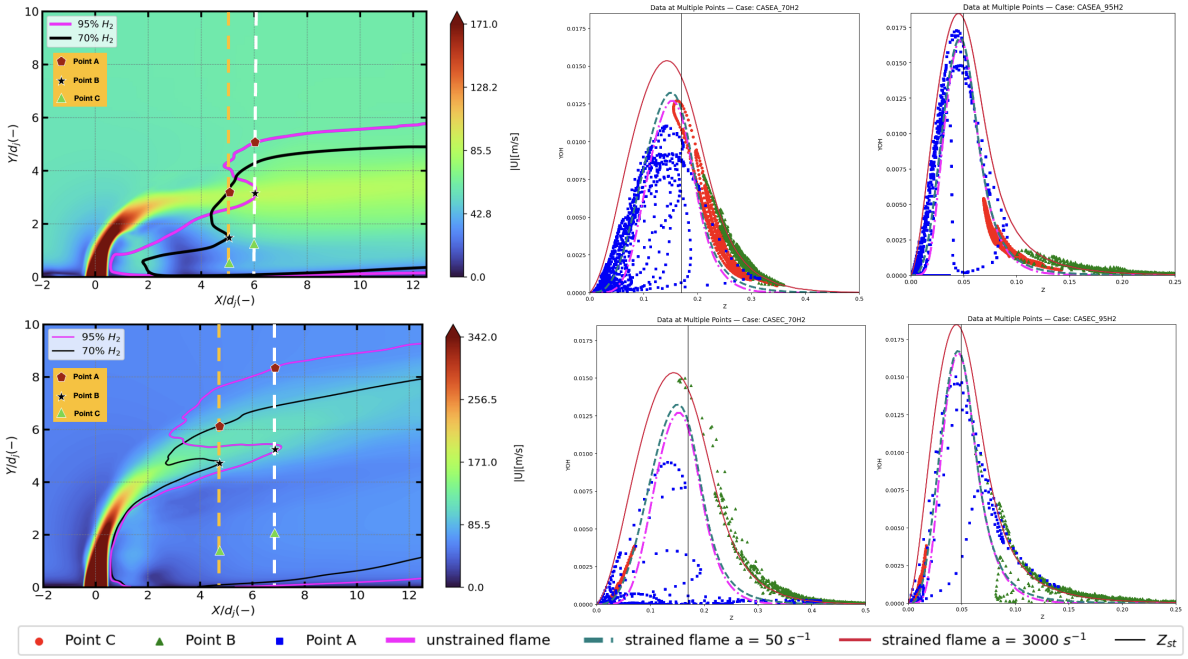


Figure 5.9: Scatter plot of YOH versus mixture fraction at flame front location of different cases

at varying strain rates. It should be noted that in the unstrained flame, Y_{OH} is lower than the strained values; however, the temperature (not shown here) of the unstrained flame is higher, as expected. Similarly, the peak temperature aligns with the stoichiometric condition, whereas the maximum Y_{OH} values occur under slightly leaner conditions.

At point A, located at the top edge of the lifted flame branch, for 70 % cases, the scatter plot exhibits an ignition-extinction cycle, characterized by an elliptical spread on the lean side near the stoichiometric Z value (Z_{st}). This behavior highlights the presence of intermediate reaction states as fresh gasses mix with combustion products, where ignition and extinction are equally probable. The points of 95 % cases follow the theoretical curve more closely and spread on both the lean and rich sides, indicating much better mixing. At point B, located at the concave region where the lifted and lee-stabilized flame branches connect, the scatter plot shows a trend similar to that at point A. The scatter points mostly stay on the rich side and closely follow the highly strained theoretical curve, indicating the unsteady strain effects from the fuel stream. 70 % case points stayed on the 3000 s^{-1} strained line, while 95 % cases shifted between different strains, indicating more unsteadiness in the 95 % cases. At point C, located inside the lee-stabilized flame branch, results from all cases follow the curve of unstrained or low strained flame due to the low strain effects in this zone. The majority of the points are concentrated in a narrow region of Z values, indicating a premixed reaction in this region. However, for case Cs, the scatter points stayed on the lean side, while case As

stayed on the rich side, indicating stronger differential diffusion effects in the lee-stabilized branch side.

5.6 Covariance-transfer UQ for Hydrogen Jet Flames

The results and analysis in Section 5.5 showed that flame structure and stabilization are controlled primarily by the jet momentum ratio, J, while changes in hydrogen content by volume do not significantly alter the global stabilization mode. In all cases, the flame remains in the same two-branch stable configuration, with lee-stabilized and lifted branches set by the local strain–chemistry balance. Against this common global structure, the present section turns to the more subtle differences in chemical state that appear when kinetic-parameter uncertainty is applied to the chemistry model. The FFCM-2 mechanism, along with its covariance matrix [132; 133], was used as a basis to transfer to the target H_2-Air mechanism [11] by the UQ method in Section 5.2.

5.6.1 Eulerian Chemical State Dynamics

Figure 5.10 isolates the lifted branch and visualizes how kinetic uncertainty manifests in the local thermo-chemical state. The scatter points are extracted from a time-averaged mid-plane slice and filtered by (i) spatial location (lifted branch region) and (ii) mixture fraction, selecting points in a narrow band around the stoichiometric value, $|Z - Z_{\mathrm{st}}| < 0.05 Z_{\mathrm{st}}$, so that the statistics represent the diffusion-flame front associated with the lifted branch. Each point is plotted in (χ, T) space and colored by the relative variation (coefficient of variation) of the OH production rate inferred from UQ,

$$\beta_{\dot{\omega}_{\mathrm{OH}}} = \frac{\sigma(\dot{\omega}_{\mathrm{OH}})}{|\mu(\dot{\omega}_{\mathrm{OH}})|}, \tag{5.13}$$

where $\mu(\cdot)$ and $\sigma(\cdot)$ are the mean and standard deviation over the ensemble of kinetic-parameter perturbations generated from the transferred covariance (Sec. 5.3). This diagnostic is used because $\dot{\omega}_{\mathrm{OH}}$ is a sensitive marker of H_2–air reaction-zone intensity and directly reflects shifts among chain-branching/termination pathways.

The lifted-branch points collapse onto a flamelet-like manifold: higher T occurs at lower χ, while increasing χ corresponds to progressively cooler states approaching local quenching, consistent with the SDR-flame front alignment discussed in the previous section. The dominant separation in Fig. 5.10 is composition-driven: the 70% H_2 cases populate a substantially higher χ-range than the 95% H_2 cases. This shift can be interpreted through the

stoichiometric mixture fraction Z_{st}, which sets where the diffusion flame front can reside relative to the jet shear layer and its vortical structures. Nair et al. [167] emphasize that for small Z_{st} (e.g. H_2–air), the diffusion flame can sit well outside the fuel jet and, hence, outside the shear layer in oxygen-rich environments; correspondingly, modest changes in Z_{st} can move the diffusion flame front toward or away from the shear layer or vortex zone. In the present cases, the lower-hydrogen blend (70% H_2) shifts the stoichiometric surface such that the lifted diffusion-flame front samples more strongly strained/mixed regions associated with the shear-layer dynamics, yielding higher χ. The higher-hydrogen cases (95% H_2) place the lifted diffusion-flame front farther from these regions on average, and the flame therefore samples a lower χ-range.

The UQ-based coloring reveals a clear composition dependence in reaction sensitivity. The 70% H_2-by-volume cases (A7, C7) exhibit markedly larger $\beta_{\dot{\omega}_{\mathrm{OH}}}$ over much of the lifted-branch manifold, especially at intermediate T and moderate-to-high χ, whereas the 95% H_2-by-volume cases (A9, C9) remain predominantly low-variation. This difference is consistent with the higher-χ, more strain-affected thermo-chemical states sampled by the 70% by-volume lifted branch, where the flame more frequently resides in intermediate chemical states with a weaker and less robust radical pool. Based on the reaction contribution ranking obtained from Cantera at representative states along the lifted-flame branch, we hypothesize that, under these conditions, OH production in the 70% cases is more sensitive to the three-body recombination pathway $\mathrm{H} + \mathrm{O} + \mathrm{M} \rightleftharpoons \mathrm{OH} + \mathrm{M}$. This pathway is uniquely important only in the 70% cases; rather, its relative contribution to local OH production appears to become larger in the 70% lifted branch, where the radical pool is less fully developed and recombination pathways may play a more important role in sustaining OH. Under this interpretation, perturbations to this reaction rate would be expected to produce larger changes in $\dot{\omega}_{\mathrm{OH}}$, consistent with the elevated $\beta_{\dot{\omega}_{\mathrm{OH}}}$ observed in the 70% cases. By contrast, the 95% H_2 lifted branch samples lower χ and appears to remain in a more chemically robust state, so OH production may be less dependent on this recombination-mediated pathway and may therefore exhibit smaller variability. To confirm these findings, a more rigorous analysis will be conducted in the future to establish the attribution of the observed variability to specific reaction pathways.

5.6.2 Lagrangian Particles

To complement Eulerian field analysis and to capture three-dimensional transport pathways and time-history effects, this study also employs Lagrangian tracer particles injected from the fuel jet. Lagrangian tracking has precedent in JICF research for relating mixing and

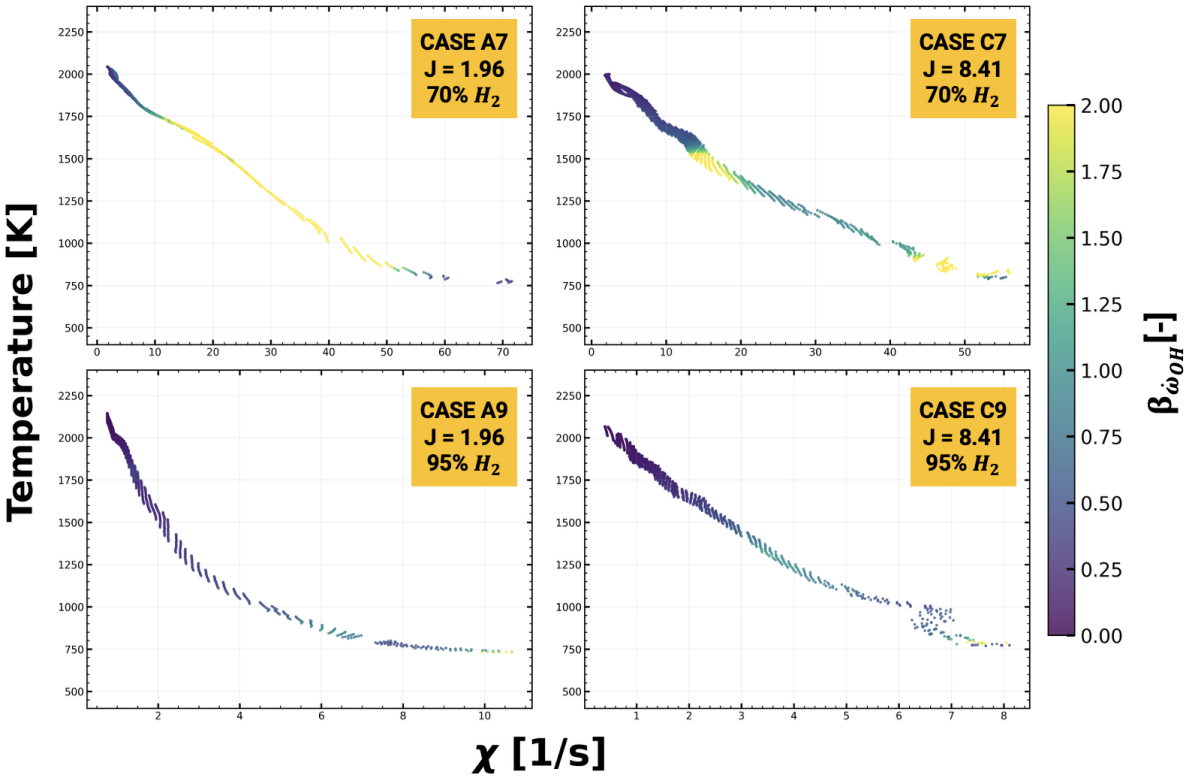


Figure 5.10: Lifted-branch diffusion-flame-front state space: scatter of temperature T versus scalar dissipation rate χ for four cases (one per panel), extracted from a time-averaged mid-plane slice and filtered by location and $|Z - Z_{\mathrm{st}}| < \Delta Z$. Marker color indicates the OH production-rate variability $\beta_{\dot{\omega}_{\mathrm{OH}}} = \sigma(\dot{\omega}_{\mathrm{OH}})/|\mu(\dot{\omega}_{\mathrm{OH}})|$ from UQ.

dispersion to coherent structures and for quantifying scalar evolution along fluid pathlines; for example, Campolo et al. [168] analyzed dispersion mechanisms in a jet in crossflow using particle tracking, and Esmaeili et al. [169] coupled LES with a stochastic Lagrangian formulation to study scalar mixing in (non-isothermal) JICF. Here, trajectories are conditioned by location and by a narrow band around the stoichiometric mixture fraction to isolate particles traversing the lifted diffusion-flame branch, enabling trajectory-conditioned statistics (e.g., PDFs of scalar dissipation and UQ-derived variability measures) that directly connect flame branch behavior to strain–mixing histories.

Lagrangian particles are continuously injected during the Eulerian simulation to track fluid properties in both time and space. These particles are defined as massless and exhibit perfectly elastic collisions with walls. Particle trajectories evolve based on velocities interpolated from the background gas flow, and their positions are updated at each simulation time step. As particles move from their injection points to the domain exit, they record the history of gas-phase properties directly from the Eulerian cells they encounter. As such, the

trajectories of these particles effectively represent pathlines of the Eulerian flow field. These properties are taken directly from the underlying Eulerian cells with no interpolation method used, so the accuracy of the recorded data is inherently tied to the resolution of the Eulerian mesh [170]. For current simulations, the particles were initialized at both D_j below the wall inside the injector and at the crossflow upstream in order to capture both the focusing of the flame behavior and to visualize the vortical structures inside the whole JICF system.

5.6.3 Lagrangian Chemical State Dynamics

The Eulerian state-space analysis in Section 5.6.2 provides a compact view of lifted-branch chemical sensitivity, but it does not capture the inherently three-dimensional transport pathways and the time history by which fluid elements reach, interact with, and traverse the lifted diffusion flame front. To address this, Lagrangian tracer particles were injected from the jet stream and tracked over time. Particles passing through the lifted branch were identified and selected using the same physical conditioning used for Fig. 5.10, namely spatial filtering in the lifted branch region together with a narrow band around the stoichiometric mixture fraction.

Before examining the trajectory-conditioned statistics, it is useful to consider the particle motion itself. Figure 5.11 shows representative lifted-branch trajectories for Case C7, colored by temperature. The trajectories indicate that fluid elements do not follow a single monotonic route toward the lifted flame front. Instead, several transport pathways are observed, including direct convection into the lifted branch, lateral spreading within the shear layer, and recirculation-driven looping near the lee side of the jet. In particular, the side view and three-dimensional view show that some particles enter the recirculation zone, undergo partial reaction there, and are subsequently re-entrained into the colder fuel stream. This process can return heat, radicals, and partially reacted species to the low-temperature jet fluid before it reaches the lifted branch. Such recirculation-mediated radical feedback is observed in all cases, although its extent depends on the flow conditions. These trajectories, therefore, show that the lifted diffusion flame front is shaped not only by the instantaneous local state but also by the prior thermo-chemical history of the fluid elements feeding it.

Motivated by these distinct transport histories, trajectory-conditioned probability density functions (PDF) were constructed using the instantaneous scalar dissipation rate $\chi(t)$ and the OH production-rate variability $\beta_{\dot{\omega}_{\mathrm{OH}}}(t) = \frac{\sigma(\dot{\omega}_{\mathrm{OH}})}{|\mu(\dot{\omega}_{\mathrm{OH}})|}$. For both figures, the PDF bin widths were determined using Knuth's rule, which provides a Bayesian, data-driven criterion for selecting the optimal histogram binning [171; 172]. Figure 5.12 shows the lifted-branch PDFs of $\beta_{\dot{\omega}_{\mathrm{OH}}}$. The 70% H_2-by-volume cases (A7, C7) exhibit broad distributions with

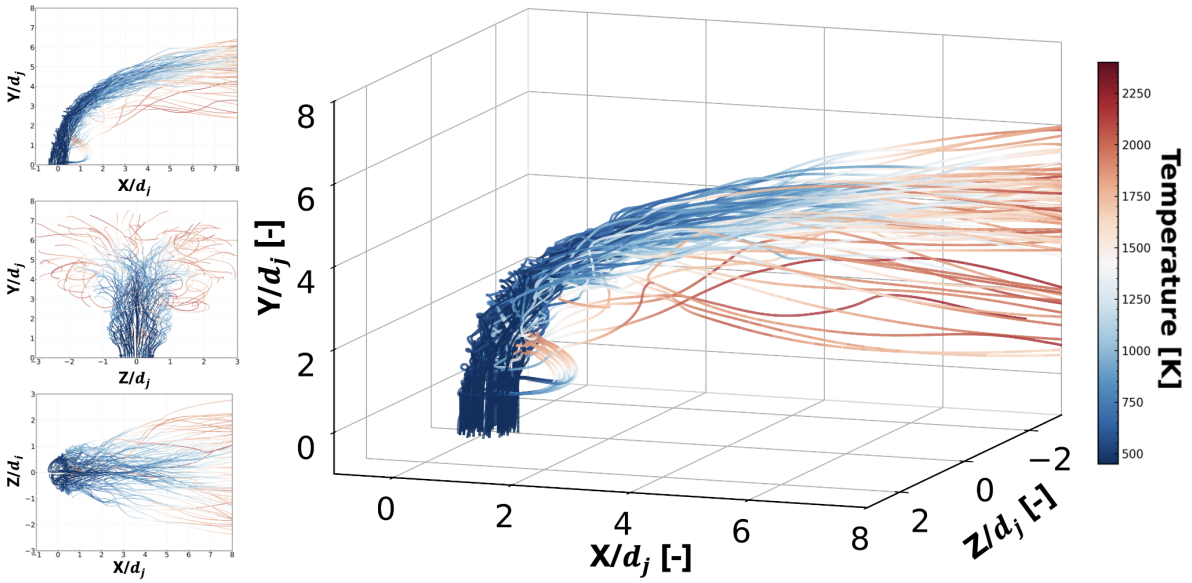


Figure 5.11: Representative lifted-branch tracer-particle trajectories for CASE C7, shown in multiple views and colored by temperature.

substantial probability extending to large $\beta_{\dot{\omega}_{\mathrm{OH}}}$, demonstrating that OH production along lifted-branch trajectories is strongly influenced by kinetic-parameter uncertainty over a wide range of sampled conditions. In contrast, the 95% H_2-by-volume cases (A9, C9) collapse to narrow peaks at relatively small $\beta_{\dot{\omega}_{\mathrm{OH}}}$ with only weak high-β tails, providing trajectory-based confirmation that the lifted diffusion flame front is markedly less sensitive to kinetic uncertainty at a higher hydrogen content by volume.

An additional feature of Fig. 5.12 is that the higher-J cases (C7 and C9) exhibit a bimodal or shoulder-like distribution in $\beta_{\dot{\omega}_{\mathrm{OH}}}$, whereas the lower-$J$ cases (A7 and A9) remain predominantly unimodal. This likely reflects the broader range of trajectory histories sampled by the lifted branch at high J. In the C-cases, stronger shear-layer dynamics and greater three-dimensional intermittency allow particles reaching the lifted branch to separate into two characteristic groups: one that passes through more strongly strained, partially reacted states with larger OH-production variability, and another that reaches the branch after experiencing more relaxed mixing histories with lower variability. The A-cases, by contrast, exhibit a more compact lifted branch and a narrower range of strain–mixing histories, so the selected particles populate a single dominant thermo-chemical state and produce only one main peak in $\beta_{\dot{\omega}_{\mathrm{OH}}}$.

Figure 5.13 reports the corresponding lifted-branch PDFs of the scalar dissipation rate χ. In direct agreement with Fig. 5.10 and the flame–SDR alignment discussed previously, the 95% H_2-by-volume cases (A9, C9) are strongly concentrated at low χ, indicating that

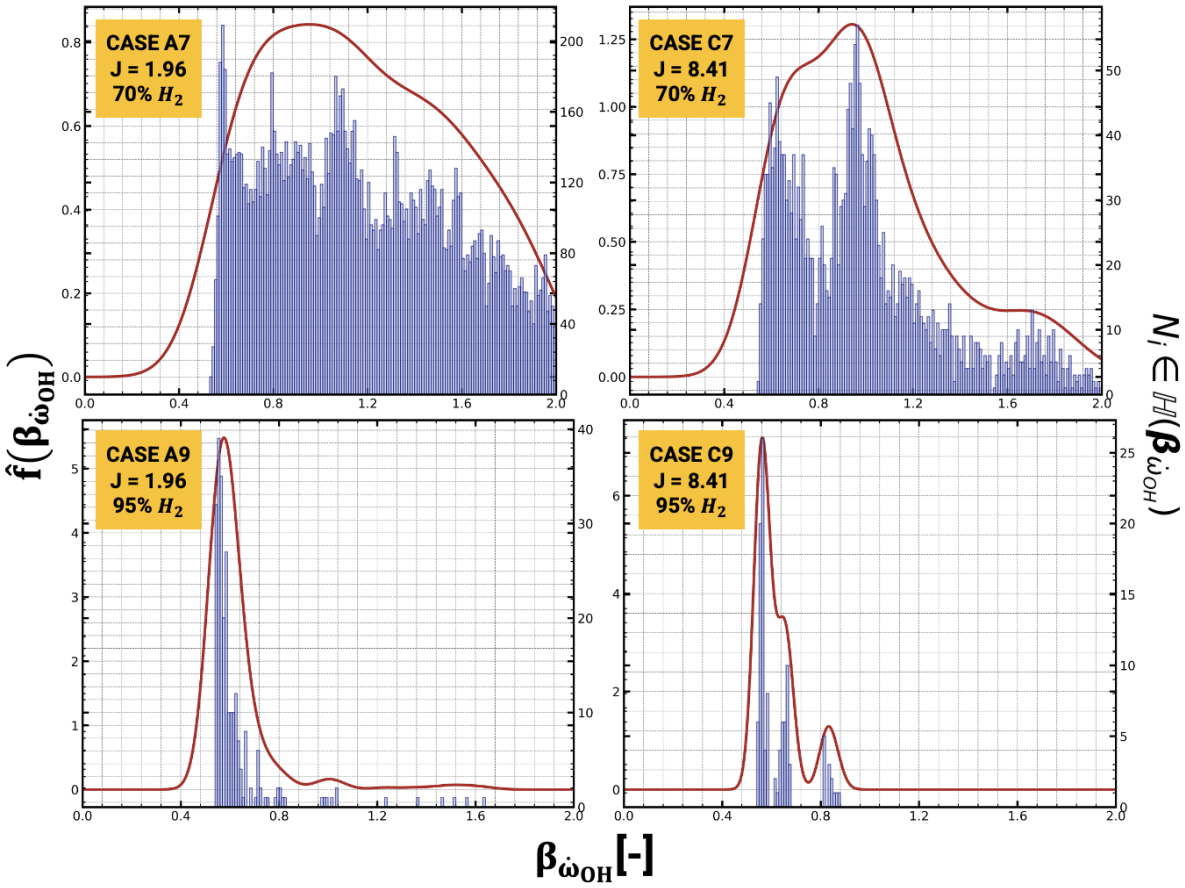


Figure 5.12: Lifted-branch diffusion-flame-front PDFs of OH production-rate variability, $\beta_{\dot{\omega}_{\mathrm{OH}}} = \sigma(\dot{\omega}_{\mathrm{OH}})/|\mu(\dot{\omega}_{\mathrm{OH}})|$. Red curve: estimated PDF $\hat{f}_{\beta_{\dot{\omega}_{\mathrm{OH}}}}(x)$ (left axis). Blue bars: sample counts N_i in each histogram bin $H(\beta_{\dot{\omega}_{\mathrm{OH}}})$ (right axis).

fluid elements reaching the lifted diffusion flame front predominantly experience weaker scalar-gradient dissipation along their histories. The 70% H_2-by-volume cases (A7, C7), by comparison, populate a substantially higher χ-range and exhibit broader distributions with pronounced high-χ tails, showing that the lifted diffusion flame front at lower hydrogen contents by volume more frequently resides in, or is fed by, strongly strained/mixed environments. This behavior is consistent with the stoichiometric-surface positioning argument noted by Nair et al. [167]: changes in Z_{st} can shift the diffusion flame front relative to the jet shear layer and associated vortical structures, thereby changing the χ levels sampled by the lifted branch. While J modulates the detailed PDF shapes through three-dimensional mixing and shear-layer intermittency, the dominant separation between the 70% and 95% H_2-by-volume cases remains the shift of probability mass toward higher χ for the 70% by-volume cases.

The trajectory visualization and the Eulerian/Lagrangian statistics establish a consistent

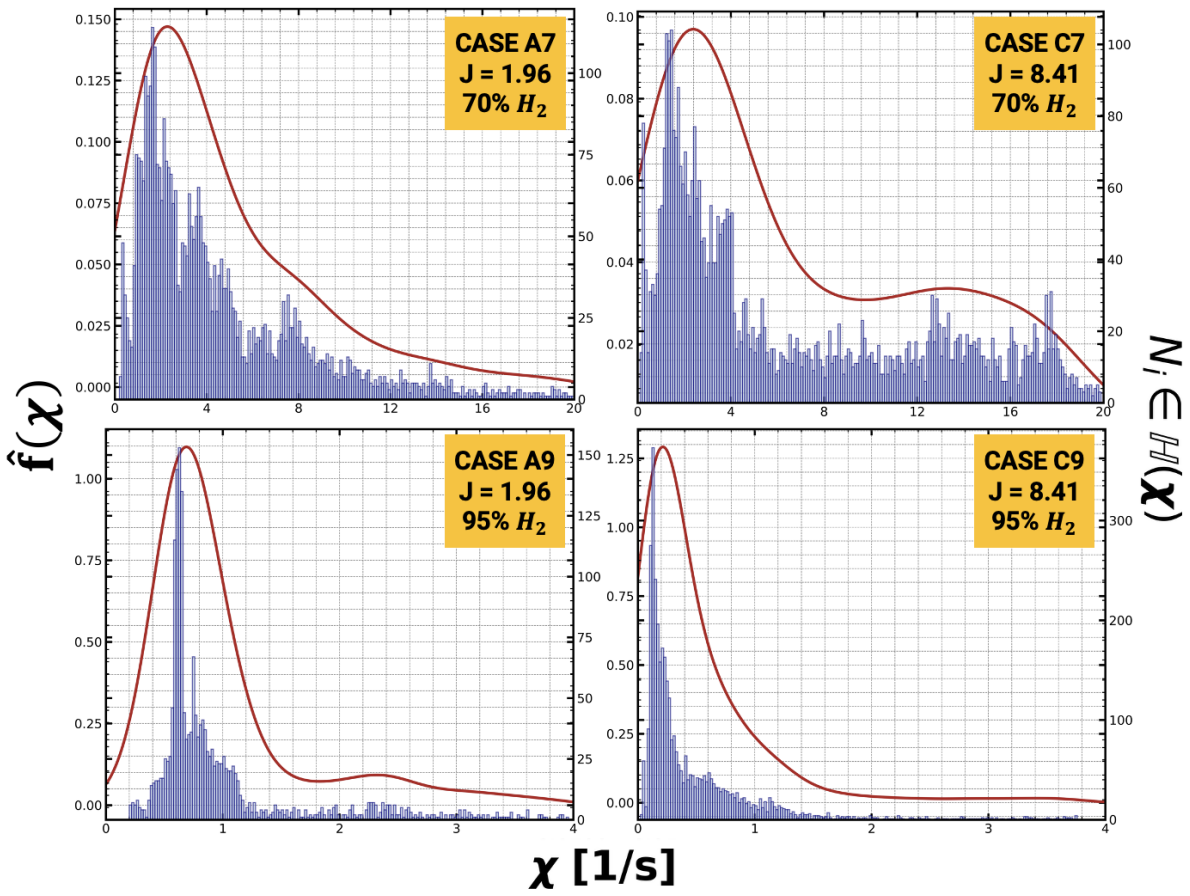


Figure 5.13: Lifted-branch diffusion-flame-front PDFs of scalar dissipation rate χ (s^{-1}). Red curve: estimated PDF $\hat{f}_\chi(x)$ (left axis). Blue bars: sample counts N_i in each histogram bin $H(\chi)$ (right axis).

picture: although J controls the macroscopic stabilization and flame topology, hydrogen content by volume systematically modulates (i) the scalar-dissipation environment sampled by the lifted diffusion flame front and (ii) the sensitivity of radical-production chemistry to kinetic-parameter uncertainty. The lower sensitivity and lower χ exposure in the 95% H_2-by-volume cases imply greater chemical robustness and improved predictive reliability of OH-based reaction-zone metrics, whereas the 70% H_2-by-volume cases operate more frequently in higher-χ conditions and exhibit amplified kinetic sensitivity. The observed recirculation-mediated return of partially reacted fluid to the cold jet further emphasizes that the lifted branch is sustained by both local strain–chemistry balance and nonlocal trajectory history, motivating uncertainty-aware interpretation for lower-H_2 blends.

5.7 Summary

The interpretation of these UQ results is resolution-aware. The identified sensitive regions are sensitive within the resolved implicit-LES thermochemical state space, especially where scalar dissipation, partial reaction, and transport history place the flame near marginal chemical states. Additional uncertainty associated with sub-filter turbulent intermittency would require either finer AMR, explicit subgrid modeling, or targeted canonical experiments.

This chapter examined kinetic uncertainty in complex reacting systems and showed that chemistry UQ can be used not only to quantify predictive variability but also to clarify how finite-rate chemistry contributes to flame stabilization. The analysis in the previous chapters established that stabilization in these hydrogen-fueled configurations is governed by coupled mixing, strain, and transport effects. The present chapter extends that picture by showing that the local chemical response to uncertain kinetics is also spatially non-uniform and strongly dependent on the thermochemical state sampled by the flow. Therefore, chemistry uncertainty can also provide a means of identifying where the flame is chemically robust and where it is more sensitive to perturbations in the kinetic description, gaining new perspectives on flame stabilization and dynamics.

Two complementary uncertainty treatments were developed and applied. The state-reconstruction UQ method was used for the multi-tube micromixer to reconstruct detailed chemical states from reduced thermochemical information and propagate correlated uncertainty from the detailed mechanism along the corresponding reaction trajectories. This framework enabled local chemistry-controlled trajectory quantities, including the chemical time to the sampled state and the equilibration time, to be evaluated throughout the combustor. The results showed that these timescales vary strongly across the multi-flame environment, with the largest variability occurring in low-to-intermediate temperature regimes and in regions influenced by recirculation, stratification, and incomplete reaction progress. These findings indicate that the chemical sensitivity of the MTM is concentrated not in the fully reacted regions but in the partially reacted states where induction, branching, and propagation pathways compete.

The covariance-transfer UQ method was then used for hydrogen transverse jets in cross-flow to construct and refine an uncertainty model directly for the reduced mechanism employed in the reacting-flow analysis. In this configuration, the deterministic flame structure remained governed primarily by the jet momentum ratio, with all cases preserving the same two-branch stabilization mode. The uncertainty analysis, however, revealed more subtle composition-dependent differences in local chemical robustness. In particular, lower-hydrogen cases sampled higher scalar-dissipation environments and exhibited significantly

larger variability in OH-production-related quantities, while the higher-hydrogen cases remained comparatively less sensitive to kinetic uncertainty. The Eulerian results showed that this enhanced sensitivity is concentrated in intermediate thermo-chemical states along the lifted diffusion flame branch, and the Lagrangian analysis further demonstrated that these differences are tied not only to the local state itself but also to the trajectory history by which fluid parcels reach the reaction zone.

The results of this chapter provide a broader interpretation of flame stabilization in complex hydrogen combustion systems. The global flame topology is set by the mixing and strain effects, but the local robustness of the flame depends on how uncertain chemistry interacts with the strained and mixed states sampled by that flow. The chapter, therefore, establishes that uncertainty-aware analysis can reveal physically important distinctions that are not apparent from deterministic fields alone, particularly in partially reacted, highly strained, or recirculation-influenced regions. More generally, these findings support the view that predictive analysis of hydrogen-fueled combustors should account not only for mean flame structure and transport processes but also for the state-dependent sensitivity of the underlying chemistry.

CHAPTER 6

Summary, Conclusions, and Future Directions

6.1 Summary

This dissertation examined flame stabilization and unsteady dynamics in hydrogen-fueled reacting flows relevant to staged and distributed gas-turbine combustors. The work was motivated by the fact that hydrogen combustors cannot be assessed reliably from global flame shape alone. Hydrogen flames are sensitive to local strain, scalar dissipation, differential diffusion, recirculation, wall proximity, finite-rate chemistry, and turbulent transport. In practical combustor geometries, these quantities vary substantially from one flame branch to another. As a result, the relevant stability problem is not only whether a flame exists globally, but also where it anchors, how each branch responds to its local flow environment, and whether any local pathway can support extinction, reignition, upstream propagation, or instability.

The simulations were performed with an AMReX-based compressible reacting-flow framework designed for high-subsonic hydrogen combustion in complex geometries. The solver combines adaptive mesh refinement, embedded boundaries, detailed finite-rate chemistry, mixture-averaged differential diffusion, and GPU-oriented chemistry acceleration. The full combustor calculations are interpreted as implicit large-eddy simulations, or resolved-large-eddy calculations, rather than full-device direct numerical simulations. No explicit subgrid turbulence model is used; the effective filter is set by the local AMR spacing and finite-volume dissipation. This approach resolves the dominant flame branches, shear layers, recirculation topology, wall-adjacent flow, differential-diffusion effects, and finite-rate chemistry at the targeted grid scale while sub-filter turbulent motion remains below the effective numerical filter.

The first configuration was a hydrogen jet in crossflow, which provided a canonical transverse-injection problem for examining branch-dependent stabilization and reduced-model limitations. The cases covered hydrogen contents of 70–95% by volume, momentum-

flux ratios $J = 1.96$–8.41, jet velocities $U_j = 100$–342 m/s, jet Reynolds numbers $Re_j = 2600$–6000, and a crossflow Reynolds number $Re_c = 4.4 \times 10^4$. The configuration isolated the coupled effects of jet penetration, wake recirculation, shear-layer reaction, lifted flame dynamics, finite-rate chemistry, and differential diffusion. The results showed that the flame is organized into distinct lee-side and lifted branches rather than a single stabilized structure. These branches occupy different regions of thermochemical state space, experience different scalar-dissipation histories, and respond differently to reduced flamelet descriptions. Reduced flamelet-based modeling captures important mean flame-topology features, but finite-rate chemistry and differential diffusion remain important for branch connection, radical-production excursions, and lifted-edge extinction/reignition behavior.

The second configuration was a pressurized 19-element multi-tube micromixer representative of distributed hydrogen injection in a gas-turbine-relevant combustor. The analyzed cases were near 11 bar, with global equivalence ratio $\phi = 0.524$–0.530, crossflow velocity $U_c = 159$–162 m/s, crossflow temperature $T_c = 758$–762 K, and fuel jet velocity $U_j = 213$–303 m/s. This configuration introduced geometric confinement, multi-jet interaction, wall-adjacent recirculation, and branch-to-branch coupling that are absent from isolated canonical flames. The simulations reproduced the experimentally observed downstream flame organization and showed that the stable operating points studied here did not produce upstream flame propagation into the tube elements. The stability of these cases was not explained by a bulk velocity argument alone. Instead, it was tied to the way heat release was distributed: the dominant reaction remained in the jet shear layers downstream of the tube exits, while the heat release associated with low-speed recirculation regions remained approximately one order of magnitude smaller.

The chemistry and uncertainty analyzes provided a complementary view of flame robustness. Finite-rate chemistry was used not only to compute source terms but also to diagnose the local sensitivity of reacting states. The state-reconstruction and covariance-transfer methods mapped kinetic sensitivity onto the resolved combustor states without requiring a full three-dimensional ensemble of perturbed simulations. In the lifted JICF branch, the OH-production variability $\beta_{\dot{\omega}_{\mathrm{OH}}} = \sigma(\dot{\omega}_{\mathrm{OH}})/|\mu(\dot{\omega}_{\mathrm{OH}})|$ depended strongly on hydrogen fraction and scalar-dissipation history. For the 70% H_2 cases, $\beta_{\dot{\omega}_{\mathrm{OH}}}$ extended over approximately 0.6–2.0, whereas the 95% H_2 cases were concentrated mainly around $\beta_{\dot{\omega}_{\mathrm{OH}}} \approx 0.55$–$0.7$. The scalar-dissipation distributions showed a similar separation, with the 70% H_2 lifted branches sampling values up to approximately 20 s^{-1}, while the 95% H_2 cases were concentrated mainly below about 1 s^{-1}. These results show that kinetic uncertainty is most useful when interpreted locally, especially in partially reacted, high-scalar-dissipation, lifted-edge, or otherwise marginal states where transport history and reaction pathways determine whether the

flame strengthens or weakens.

6.2 Scientific conclusions

The results of this dissertation support a branch-resolved view of hydrogen flame stabilization. In both the canonical JICF and the multi-tube combustor, the flame is not governed by one global stabilization mechanism. Stabilization emerges from the local balance among residence time, turbulent mixing, strain, scalar dissipation, heat release, and finite-rate chemistry. This point is clear in the JICF cases, where the lee-side and lifted branches occupy different flow environments and respond differently to the same nominal operating condition. At $J = 1.96$ and $U_j = 100$ m/s, the lee-side flame anchors approximately $2d$ downstream of the injector, or about 4 mm for the 2 mm jet. At $J = 8.41$ and $U_j = 200$ m/s, the flame reorganizes into a higher-penetration structure in which the lifted/lee connection appears near $y/d = 5$ in the detailed simulation, compared with approximately $y/d = 4$ in the reduced LES and experiment. This difference of roughly one injector diameter occurs in the region where wake burning, shear-layer reaction, and lifted-edge chemistry interact, and therefore represents a physical difference in the predicted branch-transition environment rather than a minor visual discrepancy.

The lifted JICF branch illustrates why local state-space behavior is more informative than mean flame images alone. Detailed-chemistry trajectories near the flame edge sample mixture-fraction excursions of approximately $\Delta Z \sim 0.4$ during ignition/extinction motion. At Point A, the mixture-fraction distribution has a mean $\widetilde{Z} \approx 0.18$, close to $Z_{st} \approx 0.17$, with a variance $\widetilde{Z''^2} \approx 0.03$. The flame edge therefore does not remain attached to a single stoichiometric surface; it repeatedly samples lean, near-stoichiometric, and rich states as turbulent transport moves material through the reaction zone. This trajectory dependence produces large differences in radical response. Two trajectories passing through the same general flame-edge region can differ by approximately a factor of five in Y_{OH}. The reduced S-FGM description captures the lower-intensity radical trajectory but misses the stronger radical-production excursion, indicating that reduced models can reproduce mean topology while still under representing finite-rate chemistry events that matter for local extinction and reignition.

Hydrogen enrichment also changes stabilization through both chemistry and transport. At fixed $J = 8.41$, increasing the hydrogen volume fraction from 70% to 95% requires the jet velocity to increase from 200 to 342 m/s. The momentum-flux ratio maintains comparable gross jet penetration, but the local flame response changes because density, differential diffusion, scalar dissipation, and chemical timescales are altered simultaneously.

In the 95% H_2 case, the lifted-edge state near Z_{st} undergoes an ignition/extinction loop with temperatures spanning approximately $T = 550$–2100 K. This wide temperature excursion shows that higher hydrogen content does not simply shift the flame toward a uniformly more stable state. It can strengthen chemical reactivity while also modifying the transport environment that controls lifted-edge intermittency. For combustor design, this distinction matters because hydrogen addition changes the structure of the stability problem, not only the laminar burning velocity.

The MTM combustor extends these same ideas into a realistic multi-injector geometry. The 19 flame branches do not behave as independent copies of one representative element. The center flame is the most symmetric and longest branch, but even this branch reflects the geometric anisotropy of the tube bundle: its reaction-zone width is approximately 30% smaller in the closer-spaced transverse direction than in the wider-spaced direction. The outer branches are more strongly affected by wall confinement, neighboring-jet interaction, and transverse recirculation. Weak attachment appears at repeatable locations, including $Y = \pm 3.1$, -9.18, and 22.5 mm in the mid-section Y plane and $Z = \pm 18.5$ mm in the mid-section Z plane. These locations reflect the organization imposed by tube spacing, local equivalence ratio, transverse shear, and confinement. The combustor therefore cannot be reduced to a single representative flame when the design objective is flashback margin, local extinction resistance, branch-to-branch uniformity, or heat-release distribution.

The stable MTM operating points provide a useful physical picture of flashback resistance in the simulated configuration. No flame branch propagates upstream into the tube elements for the cases analyzed. This outcome is associated with the separation between the regions that provide residence time and the regions that provide strong heat release. The low-speed recirculation zones influence flame shape, hot-product redistribution, and branch asymmetry, but their characteristic heat release remains approximately a factor of 10 lower than the dominant shear-layer heat release. The shear layers downstream of the tube exits, therefore, remain the primary burning zones. The recirculation regions are dynamically important because they affect local mixing and unsteady motion, but they do not form a strong upstream heat-release pathway. In the simulated stable cases, the flow contains low-speed structures that could influence flashback propensity, but these structures do not coincide with sufficiently intense heat release to drive sustained upstream propagation into the tubes.

The HRR-strain statistics sharpen this interpretation. The joint PDFs of principal extensive strain rate and $\log_{10}(\mathrm{HRR})$ show that each branch occupies a different strain-response environment. The center branch retains a more coherent population of reacting states over the sampled axial locations and maintains non-negligible HRR at strain rates near, and in portions of the distribution beyond, the representative counterflow extinction band. The

outer branches show more fragmented HRR distributions and stronger downstream weakening, particularly by $x = 15$–20 mm downstream of the tube exit. This behavior indicates that the center flame is more strain-tolerant and more coherently stabilized, while the outer flames are more sensitive to confinement and transverse interaction. The same statistics also explain why recirculation does not imply flashback in these cases: the strongest heat-release populations remain associated with shear-layer burning rather than with the low-speed recirculation cores. A recirculation zone becomes flashback-relevant only if it also supports sufficiently strong heat release and upstream transport. In the present operating regime, that combination does not occur.

This finding connects directly to gas-turbine combustor design. For a distributed hydrogen injector, the stability margin is not determined solely by comparing bulk velocity with laminar flame speed. The relevant design question is whether a local branch can combine heat release, residence time, and upstream transport in a way that overcomes the downstream flow through the tube. The present MTM cases occupy a stable part of that local stability space: the flame remains downstream of the tube exits, $\mathrm{HRR}_{\mathrm{recirc}}/\mathrm{HRR}_{\mathrm{shear}}$ is approximately 0.1, and the resolved vortical motion does not organize into a coherent upstream-propagating burning path. This interpretation does not imply that the same injector would remain stable under all fuel splits, wall temperatures, pressures, acoustic forcing levels, or hydrogen fractions. It does show which resolved quantities are most relevant to design: flame penetration distance relative to the tube exit, recirculation-zone-to-shear-layer HRR ratio, strain relative to extinction, scalar dissipation, mixture-fraction stratification, and pressure/velocity fluctuation amplitude.

Finite-rate chemistry is also part of the stabilization mechanism rather than an auxiliary modeling detail. The same global flame image can contain regions with very different chemical histories. A fluid element that reaches the reaction zone through a low-strain wake does not experience the same radical-pool evolution as one entering through a strained lifted edge or a partially premixed recirculation path. In the JICF flame, this distinction appears as trajectory-dependent radical production, broad mixture-fraction excursions, and ignition/extinction loops. In the MTM flame, it appears as the separation between strong shear-layer burning and weaker recirculation-zone reaction. These observations show that local chemistry helps determine whether perturbations decay, persist intermittently, or become relevant to extinction, flashback, or instability.

The uncertainty results make this chemistry sensitivity more concrete. In the lifted JICF branch, the 70% H_2 cases show broad OH-production variability, with $\beta_{\dot{\omega}_{\mathrm{OH}}} \approx 0.6$–$2.0$, while the 95% H_2 cases remain concentrated mainly around 0.55–0.7. At the same time, the 70% H_2 lifted branches sample scalar-dissipation values extending to approximately

20 s^{-1}, whereas the 95% H_2 branches are concentrated mainly below about 1 s^{-1}. The chemically fragile states are therefore not simply the hottest products or the regions of largest mean heat release. They are partially reacted, high-scalar-dissipation, induction-stage, or marginal states where transport history and competing reaction pathways determine the local outcome. The state-reconstruction and covariance-transfer methods turn kinetic uncertainty into a spatially resolved diagnostic: they identify where a prediction is chemically robust and where it depends strongly on uncertain reaction rates. This is especially important for hydrogen combustors because a single operating point can contain both robust branches and intermittent, chemically sensitive branches.

The reduced-model assessment follows naturally from this result. Flamelet-based descriptions remain valuable because they reduce costs and can reproduce the main mean topology when the flame samples states close to the assumed manifold. The present results support that use, but they also show where the approach becomes insufficient. The lifted JICF branch samples broad mixture-fraction excursions, high strain, differential diffusion, and radical-production histories that are not fully represented by the tabulated manifold. The branch-connection difference between $y/d \approx 5$ in the detailed simulation and $y/d \approx 4$ in the reduced/experimental comparison, together with the approximately fivefold spread in possible Y_{OH} responses along nearby trajectories, shows that local radical production and extinction/reignition dynamics are more demanding targets than the mean flame location. Reduced models used for hydrogen combustor design, therefore, need diagnostics that indicate when the flame leaves the assumed manifold, especially in lifted, strained, or marginally burning regions.

The broader outcome of the dissertation is a branch-scale framework for interpreting hydrogen combustor stability. In the JICF problem, the important coordinates include J, Re_j, Re_c, lift-off height, branch-connection height, ΔZ, mixture-fraction variance, scalar dissipation, Y_{OH} trajectory spread, temperature excursion, and OH-production uncertainty. In the MTM problem, the corresponding coordinates include pressure, ϕ, tube spacing, flame penetration distance, reaction-zone length and width, HRR_{recirc}/HRR_{shear}, HRR-strain population structure, recirculation residence time, wall-adjacent velocity, and branch-to-branch variation. These are not only post-processing quantities. They are the quantities that determine whether a design is likely to remain stable as hydrogen fraction, fuel split, pressure, or transient forcing changes. A useful hydrogen combustor stability map should therefore identify which branch is closest to flashback, extinction, re-ignition, or acoustic coupling, rather than classifying the entire combustor only as stable or unstable.

6.3 Future directions

The immediate extension of this work is to convert the branch-resolved diagnostics into simulation-based stability maps. For the JICF configuration, the parameter space should include J, Re_j, Re_c, crossflow temperature, hydrogen volume fraction, density ratio, and confinement. The response variables should include branch lift-off distance, branch-connection height, mixture-fraction variance, progress-variable excursion amplitude, scalar dissipation, extinction/re-ignition frequency, radical-production variability, and uncertainty-weighted chemical sensitivity. For the MTM combustor, the corresponding parameter space should include tube spacing, tube diameter, fuel split, global equivalence ratio, hydrogen fraction, pressure, inlet velocity, wall temperature, and acoustic forcing. The response variables should include flame penetration distance relative to the tube exit, $\mathrm{HRR}_{\mathrm{recirc}}/\mathrm{HRR}_{\mathrm{shear}}$, HRR-strain population structure, pressure fluctuation amplitude, recirculation residence time, local strain/extinction proximity, and branch-to-branch heat-release variation. The present MTM cases suggest that $\mathrm{HRR}_{\mathrm{recirc}}/\mathrm{HRR}_{\mathrm{shear}}$ is a useful flashback-relevant coordinate because it separates a flame-shaping recirculation zone from a stronger upstream-propagating heat-release pathway.

Targeted canonical experiments would be valuable for isolating the mechanisms observed in the full simulations. A single optically accessible tube element with controlled transverse fuel injection, adjustable wall temperature, and independent control of inlet velocity and equivalence ratio would isolate the competition among shear-layer burning, tube-exit flashback resistance, and recirculation-zone heat release. A three- or five-tube linear array with variable spacing and sidewall distance would isolate branch-to-branch interaction and wall-induced recirculation without the full complexity of a 19-element bundle. A forced reacting jet-in-crossflow experiment with controlled acoustic or inlet-mixture perturbations would test whether the branch-wise indicators identified in this dissertation predict intermittent upstream propagation, lifted-edge extinction, or local re-ignition. Future experimental validation should also move beyond mean flame images. Normalized OH-PLIF is useful for comparing flame shape and branch location, but it does not provide absolute radical concentration or heat-release rate. Future measurements should combine OH-PLIF with PIV, pressure measurements, and mixture-fraction or temperature diagnostics where possible. Such experiments would make it possible to compare directly with the stability-map quantities identified here rather than relying only on global flame appearance.

The modeling direction is to embed the branch-resolved diagnostics into lower-cost combustor tools. Full AMR-based implicit LES with detailed chemistry is too expensive for broad design optimization, but the present work identifies what reduced models need to

retain: strain-sensitive progress-variable evolution, differential diffusion in hydrogen-rich regions, scalar-dissipation effects near lifted edges, recirculation-zone heat release, HRR-strain response, and a probabilistic indicator of chemical fragility. A reduced model that predicts only mean flame shape is not sufficient for flashback or operability assessment. A useful design model should identify whether a local branch approaches a high-risk region of the stability map.

Finally, the same framework should be extended from statistically stable operating points to transient operation. Load changes, hydrogen-fraction ramps, staging transients, wall-temperature changes, and acoustic disturbances can move a flame through regions where chemistry, transport, and recirculation are more strongly coupled than in the mean state. Applying state-reconstruction and covariance-transfer methods to transient simulations would show whether an operating trajectory passes through chemically fragile states before large-scale flashback or instability appears. This would extend the present dissertation from an analysis of resolved stable cases toward a predictive assessment of hydrogen gas-turbine operability margins.

APPENDIX A

Grid Convergence

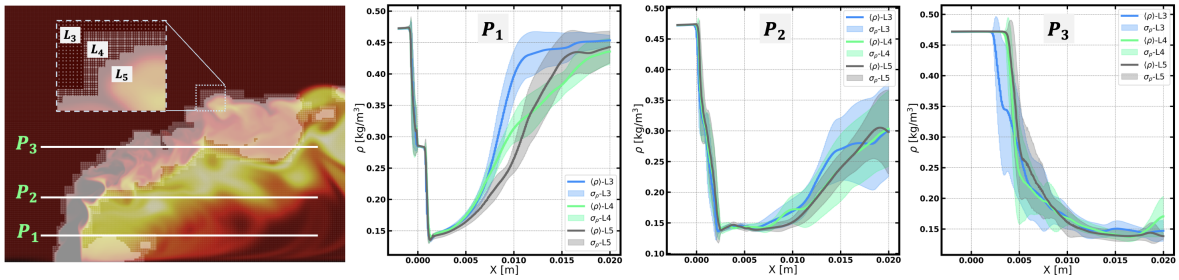


Figure A.1: Plot of temporally averaged density values with standard deviation along three lines shown in the mid-section contour plot of the simulation for three independent grid levels (shown in inset). Level 3 results are shown in blue, level 4 results in green, and level 5 results in gray.

A key aspect of the adaptive mesh refinement strategy is the ability to resolve the flame front and the near-wall flow field with sufficient fidelity while avoiding the cost of a uniformly fine resolution throughout the domain. The wall resolution can be characterized through viscous scaling.

$$y^+ = \frac{u_\tau \Delta}{\nu}, \tag{A.1}$$

where $u_\tau = \sqrt{\tau_w/\rho}$ is the friction velocity and $\tau_w = \rho\nu \left(d\tilde{U}/dy\right)_{y=0}$ is the wall shear stress estimated from the Favre-averaged velocity gradient at the wall [130]. For the present grid, the finest near-wall spacing gives $y^+ \approx 0.66$, indicating that the boundary layer is well resolved.

The flame resolution can be estimated by comparison with a one-dimensional premixed flame of similar composition. Using this approximation, the characteristic flame thickness is about 550 μm. At the finest spacing of $\Delta = 19.5$ μm, the flame front is therefore resolved with approximately 28 cells across its thickness. Although this estimate suggests adequate

spatial resolution of the flame surface, additional refinement studies are needed to determine whether the principal flow and thermochemical features have converged.

To assess this, three independent simulations were performed using refinement levels 3, 4, and 5. The temporally averaged density and its standard deviation along representative sampling lines are shown in Fig. A.1. The agreement among the three levels indicates that the bulk flame structure and mean density distribution are only weakly sensitive to further refinement beyond level 4. Some localized features become sharper as the resolution increases, but the overall system behavior and the principal stabilization characteristics remain unchanged. On this basis, level 4 is taken to provide sufficient resolution for the quantities of interest considered here, while level 5 is used when additional detail near the flame surface is desired.

An additional estimate of the turbulent resolution can be obtained from the Kolmogorov length scale,

$$\eta_k = \left(\frac{\nu^3}{\epsilon}\right)^{1/4}, \tag{A.2}$$

where the dissipation rate is estimated from the Favre-averaged fluctuating strain-rate tensor as

$$\epsilon = 2\nu\widetilde{S'_{ij}S'_{ij}}. \tag{A.3}$$

Using the minimum value obtained over several microseconds after the flow reaches statistical stationarity yields $\eta_k = 18.9$ μm. The resulting ratio of flame thickness to the Kolmogorov scale is consistent with the criterion discussed by Pope [130], and both the level-4 and level-5 meshes satisfy this requirement. These estimates support the conclusion that the present refinement strategy is sufficient to resolve the principal flame and turbulence scales relevant to the analysis.

APPENDIX B

FFCM-2 for Hydrogen Fuel

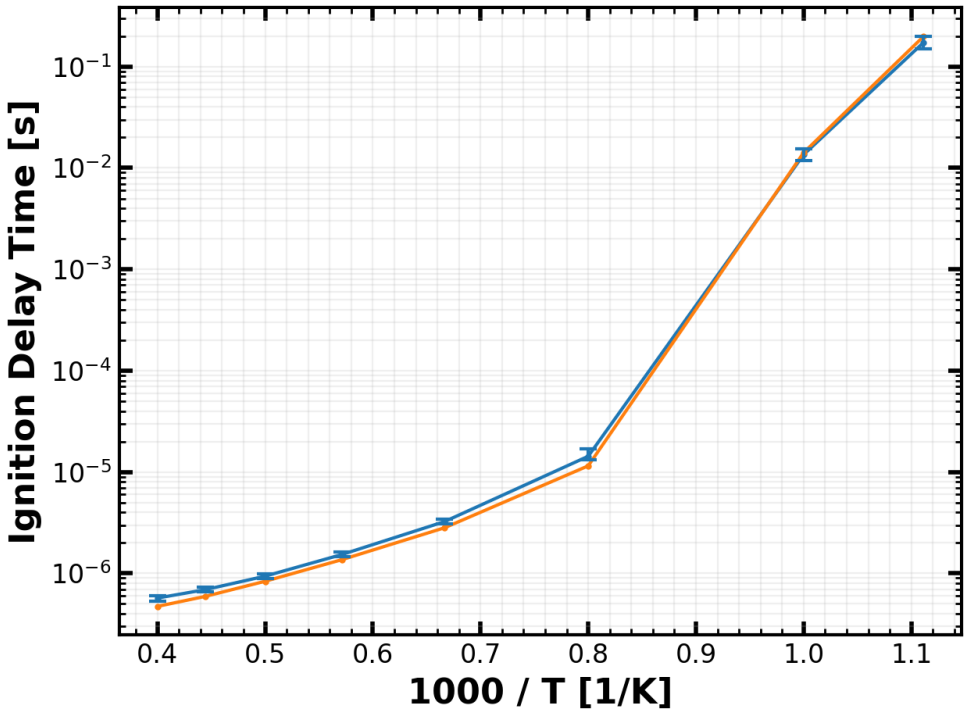


Figure B.1: Ignition delay time (log-scale) comparison for H_2 at P = 10 atm and $\phi = 0.5$ as a function of inverse temperature (1000/T), Predictions from the FFCM-2 mechanism (━color=mplblue) are compared against the H_2 mechanism [11](━color=mplorange); Bars indicate the FFCM-2 uncertainty band.

Here, the FFCM-2 mechanism, along with its covariance matrix, will be used to study the H_2 fuel reactions. Since this is a nontrivial task, validation is first conducted by computing the ignition delay time (IDT) for FFCM-2 using only hydrogen as the fuel species. Figure B.1 compares the IDT for H_2 fuel with FFCM-2 and the H_2 mechanism [11] under the simulation conditions obtained using the $\frac{dT}{dt}|_{max}$ ignition criterion. Across the full temperature range considered, the IDT trends predicted by FFCM-2 closely match those from

the H_2 mechanism, with differences that are small relative to the overall variation in IDT (spanning several orders of magnitude with temperature). In addition, the FFCM-2 predictions remain consistent with its reported uncertainty band (0.001–0.999 quantiles), and the alternative mechanism largely falls within this range. The strong agreement indicates that using the FFCM-2 mechanism for H_2 fuel reactions under these conditions is appropriate, as it reproduces comparable ignition delay behavior to the reference mechanism without introducing meaningful bias in the IDT predictions.

B.1 Validation of the uncertainty-transfer procedure against direct FFCM-2 propagation

To assess whether the variability predicted by the transferred-UQ framework could arise from the mapping/reduction procedure itself, we performed an additional canonical validation using a steady 1D counterflow flame at fuel composition and strain-rate conditions relevant to the present JICF study. In this case, uncertainty was propagated directly with the detailed FFCM-2 mechanism and its associated covariance matrix [132], without applying the transfer procedure. This comparison serves a specific purpose. The covariance information is available only for FFCM-2, whereas the reacting-flow simulations in the main study employ the reduced H_2–air mechanism of Mueller et al. [11]. As discussed in the main text, the uncertainty-transfer methodology allows the chemistry uncertainty encoded in FFCM-2 to be mapped onto reduced-manifold CFD states in a mechanism-consistent way; see Ref. [173] for details. The present counterflow calculation provides a direct reference case using the original detailed chemistry and, therefore, serves as a validation check on whether the transferred-UQ framework produces variability consistent with the parent mechanism.

Figures B.2 and B.3 show the uncertainty envelopes obtained from the direct FFCM-2 propagation for temperature and $\dot{\omega}_{\mathrm{OH}}$, respectively, plotted against Bilger mixture fraction Z. In both cases, the baseline solution lies very close to the central tendency of the ensemble, and the uncertainty bands remain relatively modest across the flame structure, including in the vicinity of the stoichiometric mixture fraction. These results indicate that the chemistry uncertainty encoded by the original FFCM-2 covariance does not generate anomalous variability in this canonical flame configuration.

To further examine whether large OH-production variability can emerge under extinction-sensitive conditions, we also performed additional steady counterflow calculations in which the strain rate was increased toward the corresponding extinction limit for the relevant fuel cases. In these near-extinction counterflow flames, the direct FFCM-2 ensemble exhibits substantially amplified variability in $\dot{\omega}_{\mathrm{OH}}$, particularly in the vicinity of the stoichiometric

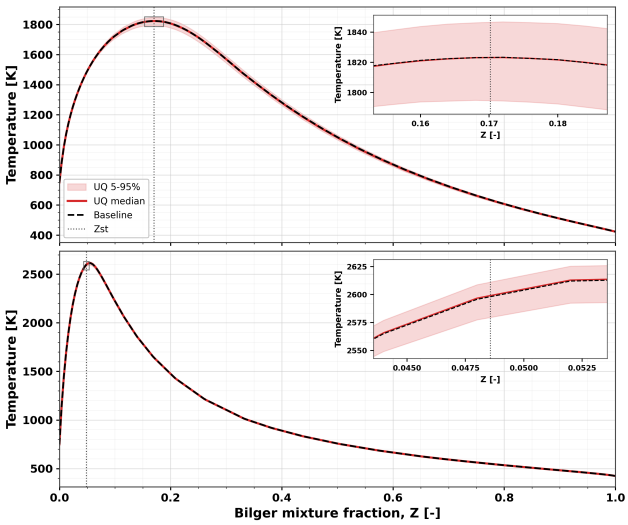


Figure B.2: Direct uncertainty propagation using the original FFCM-2 mechanism and covariance matrix for a representative counterflow flame at JICF-relevant conditions. Temperature is shown as a function of Bilger mixture fraction Z. The shaded region denotes the 5–95% interval, the red solid line denotes the ensemble median, and the black dashed line denotes the baseline solution. Insets highlight the uncertainty level near the stoichiometric mixture fraction.

mixture fraction. As shown in Fig. B.4, the uncertainty envelope broadens markedly as the flame approaches extinction, with relative variation becoming order-unity in some regions. This provides a qualitative indication that the large variability observed in OH production under the lifted-flame conditions is physically plausible near extinction and is not solely a consequence of the uncertainty-transfer procedure.

This validation supports the conclusion that the larger variability observed in the lifted-flame analysis, particularly in $\beta_{\dot{\omega}_{\mathrm{OH}}}$ for the 70% H_2 cases, is not an artifact of the uncertainty-transfer procedure itself. At the same time, the limitations of the canonical configuration should be kept in mind. A steady counterflow flame does not reproduce the unsteady recirculation, lifted-branch motion, or intermittent near-extinction behavior present in the JICF configuration. In addition, for a given steady counterflow configuration, extinction is approached through a single threshold in strain rate, whereas the lifted branch in the full reacting-flow simulation samples a broader unsteady state space. Therefore, while the counterflow results validate the mechanism-consistency of the UQ framework and provide a useful near-extinction reference, they do not fully represent the dynamical flame-state sensitivity sampled along the lifted branch in the full reacting-flow simulations.

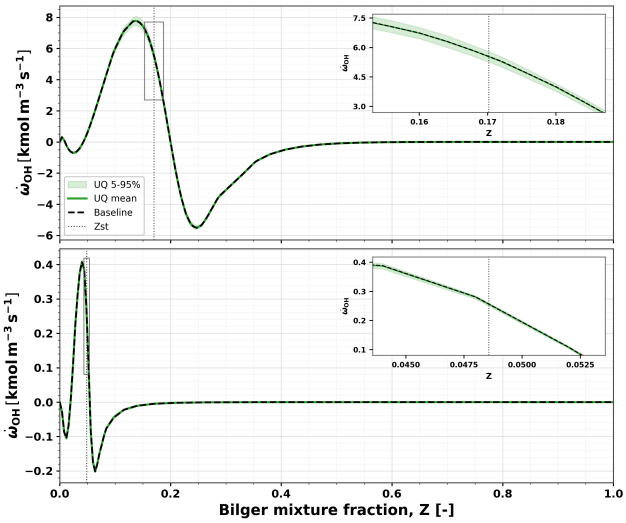


Figure B.3: Direct uncertainty propagation using the original FFCM-2 mechanism and covariance matrix for the same representative counterflow flame as in Fig. B.2. The OH production rate $\dot{\omega}_{\mathrm{OH}}$ is shown as a function of Bilger mixture fraction Z. The shaded region denotes the 5–95% interval, the green solid line denotes the ensemble mean, and the black dashed line denotes the baseline solution. Insets highlight the uncertainty level near the stoichiometric mixture fraction.

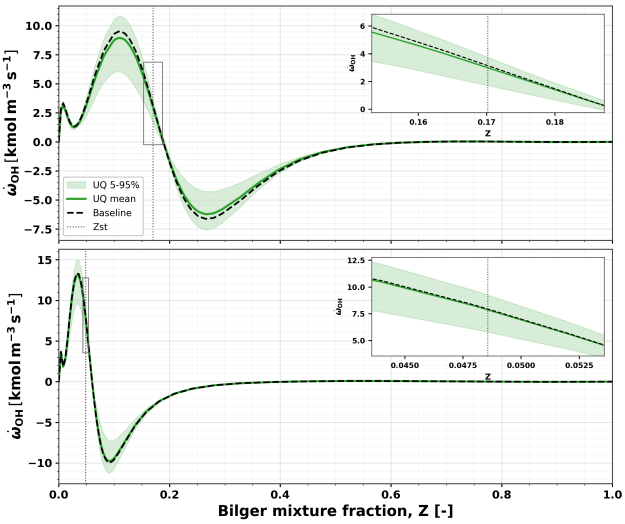


Figure B.4: Direct uncertainty propagation using the original FFCM-2 mechanism and covariance matrix for a counterflow flame at strain rates approaching the steady extinction limit. The OH production rate $\dot{\omega}_{\mathrm{OH}}$ is plotted as a function of Bilger mixture fraction Z. The shaded region denotes the 5–95% interval, the green solid line denotes the ensemble mean, and the black dashed line denotes the baseline solution. Insets highlight the uncertainty level near the stoichiometric mixture fraction. The broadening of the uncertainty band demonstrates that OH-production variability increases substantially as the steady flame approaches extinction.

APPENDIX C

Variational Inference Convergence

Figure C.1 shows the convergence history of the normalized objective $\tilde{\mathcal{L}}(N)$ and indicates a consistent two-stage optimization process across all runs. In addition to the baseline case initialized from the transferred covariance model (*Prior*), five additional runs were performed using randomized covariance matrices as the initial prior covariance. These additional runs were used to test whether the variational regression depends strongly on the exact initial covariance specification.

The lower panel of Fig. C.1 shows that all six cases follow nearly the same overall evolution. In the initial stage, $\tilde{\mathcal{L}}(N)$ decreases rapidly from approximately 1 to about 0.14–0.16 within the first ~ 200 iterations, indicating a major improvement in the posterior fit to the ignition-delay targets $\mathbf{y}$. After this sharp initial descent, the optimization enters a slower adjustment stage, and a weaker secondary decrease is visible around $N \approx 600$–700. Beyond this point, all trajectories approach a nearly stationary level near 0.11–0.12. The inset in Fig. C.1 highlights this late-stage regime. Although small differences remain among the individual runs, the objective values remain confined to a narrow band, and no trajectory shows a continued systematic decrease relative to the others. Instead, the curves fluctuate weakly about nearly constant values. This behavior is consistent with the practical convergence of the variational optimization.

The upper panel provides a complementary measure of convergence through the normalized increment

$$\frac{\Delta\mathcal{L}(N)}{\max(1, |\mathcal{L}(N-1)|)}.$$

During the early stage, this quantity becomes strongly negative, consistent with the rapid drop in $\tilde{\mathcal{L}}(N)$. Around the transition near $N \approx 180$–200, the magnitude of the negative change reaches its largest value, marking the end of the main descent phase. Afterward, $\Delta\mathcal{L}(N)$ fluctuates around zero with relatively small amplitude and without sustained drift. This is an important indication that the optimizer has entered a stationary regime: the

remaining variation reflects stochastic fluctuations in the estimated objective rather than continued systematic improvement.

An important result of Fig. C.1 is that the five randomized-start cases converge to nearly the same final objective level as the run initialized from the covariance-transfer prior. Although the early trajectories differ slightly, especially during the first few hundred iterations, the late-stage values are highly consistent. This indicates that the variational regression is not strongly sensitive to the exact initial covariance matrix. In other words, the regression remains stable even when the prior covariance used at initialization is not exact. This is a useful practical result for the covariance-transfer UQ framework because it shows that the inferred posterior is determined primarily by the combination of prior regularization and ignition-delay information rather than by a single finely tuned starting covariance.

In the implementation, the objective function is

$$\mathcal{L}(N) = -(1-\alpha_w)\,\mathbb{E}_q[\log p(\mathbf{y} \mid \theta)] + \alpha_w\, w_{\mathrm{KL}}(N)\,\mathrm{KL}(q(\theta) \,\|\, p(\theta))\,,$$

with fixed $\alpha_w = 0.5$ and a linear KL warmup,

$$w_{\mathrm{KL}}(N) = \min\!\left(1, \frac{N - N_{\mathrm{start}}}{N_{\mathrm{warm}}}\right), \qquad N_{\mathrm{warm}} = 50, \qquad w_{\mathrm{KL}}^{\max} = 1.$$

Accordingly, relative to the current starting step, the effective KL coefficient increases linearly from 0 to 0.5 over the first 50 iterations, while the likelihood term remains weighted by 0.5 throughout. The likelihood is defined in log space using a relative noise level $\sigma_{\mathrm{rel}} = 0.05$,

$$\log p(\mathbf{y} \mid \theta) \propto -\frac{1}{2\sigma_{\mathrm{rel}}^2} \sum_i \left(\log y_i - \log \hat{y}_i(\theta)\right)^2 .$$

Optimization uses an adaptive learning rate and is performed using Rprop with `lr`$= 10^{-3}$, `etas`$(0.2, 1.02)$, and `step_sizes`$(10^{-6}, 1.0)$. Gradients are estimated using SPSA with $M = 64$ and finite-difference scale `fd_h`$= 0.1$, and the ELBO is averaged with `N_elbo_samples`$= 512$. In addition, a scheduler with factor 0.1, patience 10, threshold 10^{-4}, and minimum learning rate 10^{-8} further dampens the updates once progress stalls. The weak residual oscillations visible in both the inset and the $\Delta\mathcal{L}(N)$ history are therefore expected and reflect the combined effects of stochastic gradient estimation and adaptive step-size reduction in the converged stage of the optimization.

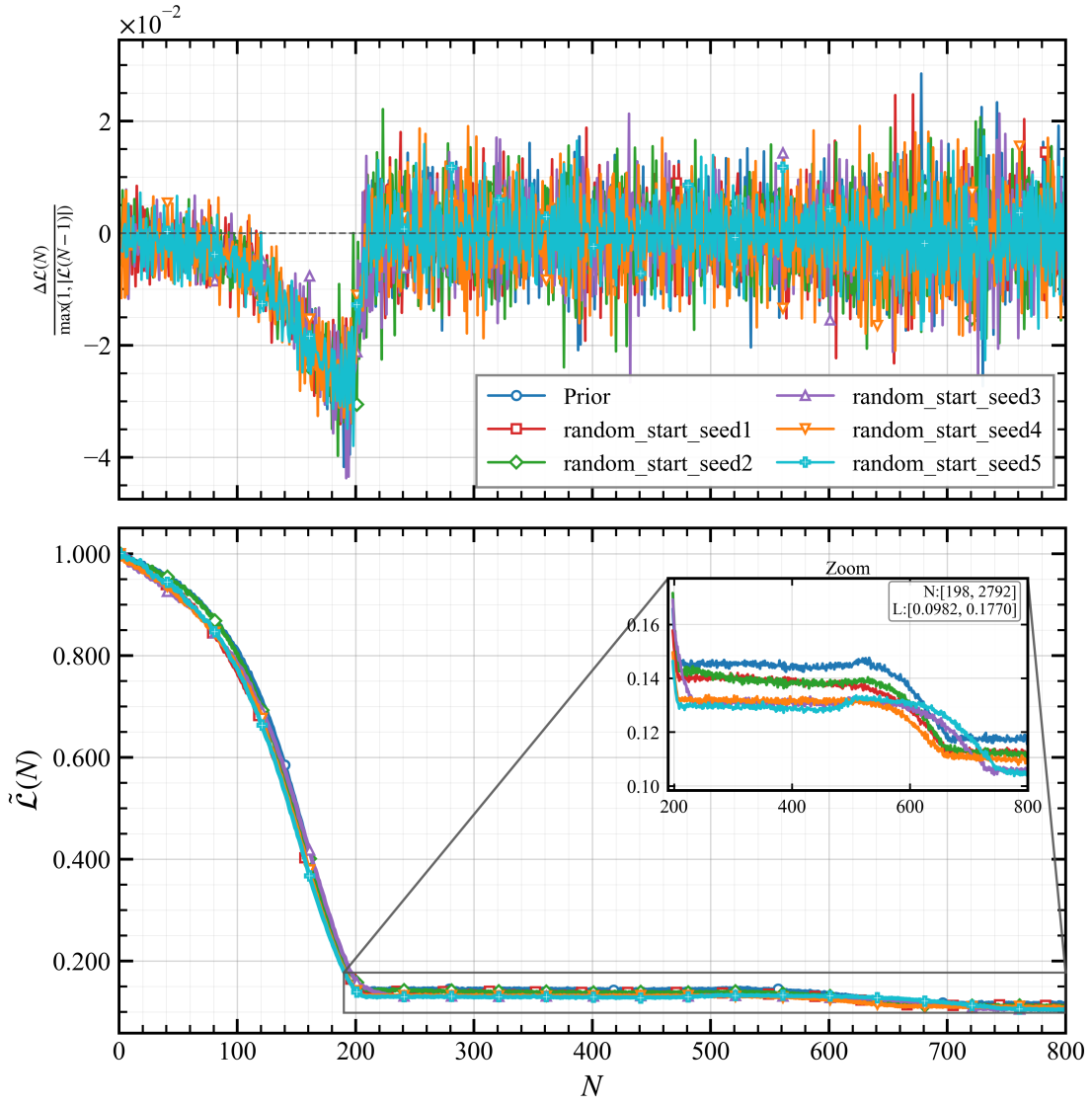


Figure C.1: Convergence history of the variational-inference optimization for the covariance-transfer prior (*Prior*) and five additional runs initialized from randomized covariance matrices. The lower panel shows the normalized objective $\tilde{\mathcal{L}}(N)$ as a function of iteration N, and the upper panel shows the normalized iteration-to-iteration change, $\Delta\mathcal{L}(N)/\max(1, |\mathcal{L}(N-1)|)$. The inset gives a magnified view of the late-stage regime.

BIBLIOGRAPHY

[1] California Independent System Operator. What the duck curve tells us about managing a green grid, 2016. Fast Facts report, accessed 2026-03-16.

[2] International Energy Agency. Energy and ai, 2025. IEA report, Paris, CC BY 4.0, accessed 2026-03-16.

[3] Wells Fargo Investment Institute. Artificial intelligence, 2026. Research topic page, accessed 2026-03-16.

[4] Siemens Energy. Hydrogen power plants, 2025. Product and project overview page, accessed 2026-03-16.

[5] European Commission CORDIS. HYdrogen as a FLEXible Energy Storage for a Fully Renewable Energy Ecosystem (HYFLEXPOWER), 2025. Project information page, accessed 2026-03-16.

[6] Michael Hughes, Jonathan Berry, and Joseph Weber. Advanced multi-tube mixer combustion for 65% efficiency (final report). Technical report, U.S. Department of Energy, 2021. Available at https://www.osti.gov/biblio/1810775.

[7] National Energy Technology Laboratory and GE Power. Advanced multi-tube mixer combustion for 65% efficiency, 2015. UTSR project presentation, accessed 2026-03-16.

[8] Shivank Sharma, Ral Bielawski, Oliver Gibson, Shuzhi Zhang, Vansh Sharma, Andreas H. Rauch, Jagmohan Singh, Sebastian Abisleiman, Michael Ullman, Shivam Barwey, and Venkat Raman. An AMReX-based compressible reacting flow solver for high-speed reacting flows relevant to hypersonic propulsion. arXiv preprint arXiv:2412.00900, 2024.

[9] Anthony Carreon, Jagmohan Singh, Shivank Sharma, Shuzhi Zhang, and Venkat Raman. A gpu-based compressible combustion solver for applications exhibiting disparate space and time scales. The International Journal of High Performance Computing Applications, 2026. Draft/submitted version used in this dissertation draft.

[10] Vansh Sharma, Yihao Tang, and Venkatramanan Raman. Stabilization of hydrogen-enriched jet flames in a crossflow. In AIAA SCITECH 2024 Forum, page 0393, 2024.

[11] Mark A. Mueller, Tae J. Kim, Richard A. Yetter, and Frederick L. Dryer. Flow reactor studies and kinetic modeling of the H_2/O_2 reaction. International Journal of Chemical Kinetics, 31(2):113–125, 1999.

[12] Adam M. Steinberg, Rajesh Sadanandan, Claudiu Dem, Peter Kutne, and Wolfgang Meier. Structure and stabilization of hydrogen jet flames in cross-flows. Proceedings of the Combustion Institute, 34(1):1499–1507, 2013.

[13] Tristan T. Shahin, Alexander J. Hodge, Benjamin K. Murdock, Thomas N. McLean, Keaton C. Koenig, Rohan M. Gejji, Robert P. Lucht, and Carson D. Slabaugh. Dynamics of hydrogen–ammonia–natural gas lean-premixed high-pressure flames. Fuel, 385:134016, 2025.

[14] Alexander J. Hodge, Tristan T. Shahin, Rohan Gejji, Robert P. Lucht, and Carson D. Slabaugh. 100 khz oh plif of high-pressure h2/nh3 and h2/ch4 flames. In AIAA SCITECH 2025 Forum, page 2310, 2025.

[15] Stephanie Searle. E-fuels won't save the internal combustion engine. International Council on Clean Transportation blog, June 2020. URL https://theicct.org/blog/staff/e-fuels-will-not-save-ice. Accessed from user-provided PDF copy.

[16] Gary J. Stiegel and National Energy Technology Laboratory. Gasification – versatile solutions: Doe's gasification program overview. Technical report, U.S. Department of Energy, National Energy Technology Laboratory, August 2008. User-provided PDF: DOEGasificationProgramOverview2008-08-11v1.pdf.

[17] U.S. Department of Energy, Office of Fossil Energy and Federal Energy Technology Center. Vision 21: Clean energy for the 21st century. Technical report, U.S. Department of Energy, November 1998. User-provided PDF: vision21.pdf.

[18] Savvas Gkantonas, Midhat Talibi, Ramanarayanan Balachandran, and Epaminondas Mastorakos. Hydrogen combustion in gas turbines. In Hydrogen for Future Thermal Engines, Green Energy and Technology, pages 407–428. Springer, Cham, 2023. doi: 10.1007/978-3-031-28412-0_10. Review chapter.

[19] K. S. Pugach, L. A. Bulysova, and V. D. Vasiliev. Hydrogen-rich fuel combustion in power gas turbine plants. Power Technology and Engineering, 58:87–94, 2024. doi: 10.1007/s10749-024-01780-4.

[20] Donato Cecere, Eugenio Giacomazzi, Antonio Di Nardo, and Giorgio Calchetti. Gas turbine combustion technologies for hydrogen blends. Energies, 16(19):6829, 2023. doi: 10.3390/en16196829.

[21] Haiqin Zhou, Jiye Xue, Haobu Gao, and Nan Ma. Hydrogen-fueled gas turbines in future energy system. International Journal of Hydrogen Energy, 64:569–582, 2024. doi: 10.1016/j.ijhydene.2024.03.327.

[22] GE Vernova. For 7f gas turbines: Axial fuel staging (afs) fact sheet, 2025. Technology fact sheet, accessed 2026-03-16.

[23] GE Vernova. 7f axial fuel staging (afs) turbine upgrade, 2025. Web page, accessed 2026-03-16.

[24] Siemens Energy. White paper: Hydrogen capable gas turbines, 2025. White paper, accessed 2026-03-16.

[25] Gas Turbine World. Ansaldo tests 100% hydrogen fuel using sequential combustion, 2024. Reporting on Ansaldo Energia sequential-combustion development, accessed 2026-03-16.

[26] National Energy Technology Laboratory and GE Power. Advanced multi-tube mixer combustion for 65% efficiency, 2019. UTSR project presentation, accessed 2026-03-16.

[27] Daniel Mason et al. Performance and flexibility of the dln 2.6e combustion system on the 7ha.03 gas turbine. In Proceedings of ASME Turbo Expo 2024, 2024. ASME Digital Collection, paper V03BT04A031.

[28] Heinz Pitsch. The transition to sustainable combustion: Hydrogen- and carbon-based future fuels and methods for dealing with their challenges. Proceedings of the Combustion Institute, 40(1–4):105638, 2024. doi: 10.1016/j.proci.2024.105638.

[29] Hemanth Kolla, Ray Grout, Andrea Gruber, and Jacqueline H. Chen. Mechanisms of flame stabilization and blowout in a reacting turbulent hydrogen jet in cross-flow. Combustion and Flame, 159(8):2755–2766, 2012.

[30] Mirko Gamba, Victor A. Miller, and M. Godfrey Mungal. The reacting transverse jet in supersonic crossflow: Physics and properties. In 19th AIAA International Space Planes and Hypersonic Systems and Technologies Conference. American Institute of Aeronautics and Astronautics, 2014. doi: 10.2514/6.2014-3107.

[31] Mirko Gamba and M. Godfrey Mungal. Ignition, flame structure and near-wall burning in transverse hydrogen jets in supersonic crossflow. Journal of Fluid Mechanics, 780: 226–273, 2015. doi: 10.1017/jfm.2015.454.

[32] Xudong Jiang, Yihao Tang, Zhaohui Liu, and Venkat Raman. Computational modeling of boundary layer flashback in a swirling stratified flame using a les-based non-adiabatic tabulated chemistry approach. Entropy, 23(5):567, 2021.

[33] Pratikash Panda, S. P. R. Muppala, S. R. Chakravarthy, B. Sekar, and N. K. S. Rajan. Flame stabilization mechanism in reacting jets in swirling vitiated crossflow. Experimental Thermal and Fluid Science, 107:30–44, 2019. doi: 10.1016/j.exptherm flusci.2019.04.012.

[34] M. Awad, P. Rajendram Soundararajan, S. Gkantonas, and E. Mastorakos. Flame stabilisation mechanism for single and multiple jets in cross flow. Flow, Turbulence and Combustion, 2025. doi: 10.1007/s10494-025-00703-1.

[35] T. L. Howarth, M. A. Picciani, E. S. Richardson, M. S. Day, and A. J. Aspden. Direct numerical simulation of a high-pressure hydrogen micromix combustor: Flame structure and stabilisation mechanism. Combustion and Flame, 265:113504, 2024. doi: 10.1016/j.combustflame.2024.113504.

[36] Gaurav Singh, B. Deneys J. Schreiner, Xiaoxiao Sun, and Vishal Sethi. A review of hydrogen micromix combustion technologies for gas turbine applications. International Journal of Hydrogen Energy, 2025. doi: 10.1016/j.ijhydene.2025.04.007.

[37] Vineeth Nair, Gireeshkumar Thampi, and R. I. Sujith. Intermittency route to thermoacoustic instability in turbulent combustors. Journal of Fluid Mechanics, 756:470–487, 2014. doi: 10.1017/jfm.2014.468.

[38] Nitin Babu George, Manikandan Raghunathan, Vishnu R. Unni, R. I. Sujith, Jürgen Kurths, and Elena Surovyatkina. Preventing a global transition to thermoacoustic instability by targeting local dynamics. Scientific Reports, 12:9305, 2022. doi: 10.1038/s41598-022-12951-6.

[39] Amitesh Roy, Samarjeet Singh, Asalatha Nair, Swetaprovo Chaudhuri, and R. I. Sujith. Flame dynamics during intermittency and secondary bifurcation to longitudinal thermoacoustic instability in a swirl-stabilized annular combustor. Proceedings of the Combustion Institute, 38(4):6221–6230, 2021. doi: 10.1016/j.proci.2020.08.053.

[40] Samarjeet Singh, Amitesh Roy, K. V. Reeja, Asalatha Nair, Swetaprovo Chaudhuri, and R. I. Sujith. Intermittency, secondary bifurcation and mixed-mode oscillations in a swirl-stabilized annular combustor: Experiments and modeling. Journal of Engineering for Gas Turbines and Power, 143(5):051028, 2021. doi: 10.1115/1.4049407.

[41] Christopher E. Schneider and Adam M. Steinberg. Statistics and dynamics of intermittent boundary layer flashback in swirl flames. Journal of Propulsion and Power, 36:940–949, 2020. doi: 10.2514/1.B37815.

[42] G. Willems. Unraveling flashback phenomena of turbulent premixed hydrogen-natural gas-air flames. Master's thesis, Delft University of Technology, 2022.

[43] Mihnea Floris, Tadikonda Shiva Sai, Dibyajyoti Nayak, Ivan Langella, Konduri Aditya, and Nguyen Anh Khoa Doan. Data-driven identification of precursors of flashback in a lean hydrogen reheat combustor. Proceedings of the Combustion Institute, 40(1-4): 105524, 2024. doi: 10.1016/j.proci.2024.105524.

[44] Shiming Zhang, Zhen Lu, and Yue Yang. Synergy of turbulence and thermo-diffusive effects on the intermittent boundary-layer flashback of swirling flames. Combustion and Flame, 281:114458, 2025. doi: 10.1016/j.combustflame.2025.114458.

[45] Soufien Taamallah, Zachary A. LaBry, Santosh J. Shanbhogue, and Ahmed F. Ghoniem. Thermo-acoustic instabilities in lean premixed swirl-stabilized combustion and their link to acoustically coupled and decoupled flame macrostructures. Proceedings of the Combustion Institute, 35(3):3273–3282, 2015. doi: 10.1016/j.proci.2014.07.002.

[46] S. J. Shanbhogue, Y. S. Sanusi, S. Taamallah, M. A. Habib, E. M. A. Mokheimer, and A. F. Ghoniem. Flame macrostructures, combustion instability and extinction strain scaling in swirl-stabilized premixed ch_4/h_2 combustion. Combustion and Flame, 163: 494–507, 2016. doi: 10.1016/j.combustflame.2015.10.026.

[47] Michael Stöhr, Zhiyao Yin, and Wolfgang Meier. Interaction between velocity fluctuations and equivalence ratio fluctuations during thermoacoustic oscillations in a partially premixed swirl combustor. Proceedings of the Combustion Institute, 36(3):3907–3915, 2017. doi: 10.1016/j.proci.2016.06.084.

[48] Yongseok Choi and Kyu Tae Kim. Mode shape-dependent thermoacoustic interactions between a lean-premixed primary flame and an axially-staged transverse reacting jet. Combustion and Flame, 255:112884, 2023. doi: 10.1016/j.combustflame.2023.112884.

[49] Yu Guan, Yongseok Choi, Peijin Liu, and Kyu Tae Kim. Mutual synchronization and flame dynamics in an axially fuel-staged lean-premixed combustion system. Proceedings of the Combustion Institute, 40(1-4):105197, 2024. doi: 10.1016/j.proci.2024.105197.

[50] D. W. Davis, P. L. Therkelsen, D. Littlejohn, and R. K. Cheng. Effects of hydrogen on the thermo-acoustics coupling mechanisms of low-swirl injector flames in a model gas turbine combustor. Proceedings of the Combustion Institute, 34(2):3135–3143, 2013. doi: 10.1016/j.proci.2012.05.050.

[51] Ianko Chterev and Isaac Boxx. Effect of hydrogen enrichment on the dynamics of a lean technically premixed elevated pressure flame. Combustion and Flame, 225:149–159, 2021. doi: 10.1016/j.combustflame.2020.10.033.

[52] Jadeed Beita, Midhat Talibi, Suresh Sadasivuni, and Ramanarayanan Balachandran. Thermoacoustic instability considerations for high hydrogen combustion in lean premixed gas turbine combustors: A review. Hydrogen, 2(1):33–57, 2021. doi: 10.3390/hydrogen2010003.

[53] Ankit D. Kumar, James C. Massey, Isaac Boxx, and Nedunchezhian Swaminathan. Effects of hydrogen enrichment on thermoacoustic and helical instabilities in swirl stabilised partially premixed flames. Flow, Turbulence and Combustion, 112:689–727, 2024. doi: 10.1007/s10494-023-00504-4.

[54] Yee Chee See and Matthias Ihme. Effects of finite-rate chemistry and detailed transport on the instability of jet diffusion flames. Journal of Fluid Mechanics, 745:647–681, 2014. doi: 10.1017/jfm.2014.95.

[55] Martin de La Torre, Sergio Maldonado, Sarzina Hossain, Norman Love, and Ahsan Choudhuri. Flame stability of premixed syngas-air flames emitted from a multi-tube fuel injector. In Turbo Expo: Power for Land, Sea, and Air, volume 56697, page V04BT04A046. American Society of Mechanical Engineers, 2015.

[56] H. Kang, T. Lee, U. Jin, and K. T. Kim. Experimental investigation of combustion instabilities of a mesoscale multi-nozzle array in a lean-premixed combustor. Proceedings of the Combustion Institute, 38(4):6035–6042, 2021.

[57] T. Lee and K. T. Kim. Combustion dynamics of lean fully-premixed hydrogen-air flames in a mesoscale multinozzle array. Combustion and Flame, 218:234–246, 2020. doi: 10.1016/j.combustflame.2020.04.024.

[58] Alexander Jaeschke, Bernhard Ćosić, Dominik Wassmer, and Christian Oliver Paschereit. Experimental investigation of a multi tube burner for premixed hydrogen and natural gas low emission combustion. Journal of Engineering for Gas Turbines and Power, 145(12), 2023.

[59] Johannes Berger. Scaling of an aviation hydrogen micromix injector design for industrial gt combustion applications. Aerotecnica Missili & Spazio, 100:239–251, 2021. doi: 10.1007/s42496-021-00091-5.

[60] Hemanth Kolla, Ray W. Grout, Andrea Gruber, and Jacqueline H. Chen. Mechanisms of flame stabilization and blowout in a reacting turbulent hydrogen jet in cross-flow. Combustion and Flame, 159(8):2755–2766, 2012.

[61] Lukas Berger, Antonio Attili, Michael Gauding, and Heinz Pitsch. Les combustion model for premixed turbulent hydrogen flames with thermodiffusive instabilities: A priori and a posteriori analysis. Journal of Fluid Mechanics, 1003:A33, 2025. doi: 10.1017/jfm.2024.1201.

[62] Thierry J. Poinsot and Sanjiva K. Lele. Boundary conditions for direct simulations of compressible viscous flows. Journal of Computational Physics, 101(1):104–129, 1992. doi: 10.1016/0021-9991(92)90046-2.

[63] Weiqun Zhang, Ann Almgren, Vince Beckner, John Bell, Johannes Blaschke, Cy Chan, Marcus Day, Brian Friesen, Kevin Gott, Daniel Graves, Max Katz, Andrew Myers, Tan Nguyen, Andrew Nonaka, Michele Rosso, Samuel Williams, and Michael Zingale. Amrex: A framework for block-structured adaptive mesh refinement. Journal of Open Source Software, 4(37):1370, 2019. doi: 10.21105/joss.01370.

[64] Marc T. Henry de Frahan, Jon S. Rood, Marc S. Day, Hariswaran Sitaraman, Shashank Yellapantula, Bruce A. Perry, Ray W. Grout, Ann Almgren, Weiqun Zhang, John B. Bell, and Jacqueline H. Chen. Pelec: An adaptive mesh refinement solver for compressible reacting flows. The International Journal of High Performance Computing Applications, 37(2):115–131, 2023. doi: 10.1177/10943420221121151.

[65] Shivam Barwey and Venkat Raman. A neural network-inspired matrix formulation of chemical kinetics for acceleration on gpus. Energies, 14(9):2710, 2021.

[66] David G. Goodwin, Harry K. Moffat, and Raymond L. Speth. Cantera: An object-oriented software toolkit for chemical kinetics, thermodynamics, and transport processes. version 2.3.0. Zenodo, 2017.

[67] Claudio Bruno, Vaidyanathan Sankaran, Hemanth Kolla, and Jacqueline H. Chen. Impact of multi-component diffusion in turbulent combustion using direct numerical simulations. Combustion and Flame, 162(11):4313–4330, 2015.

[68] Robert J Kee, Michael E Coltrin, and Peter Glarborg. Chemically reacting flow: theory and practice. John Wiley & Sons, Hoboken, New Jersey, 2005.

[69] Shev MacNamara and Gilbert Strang. Operator splitting. Splitting Methods in Communication, Imaging, Science, and Engineering, pages 95–114, 2016.

[70] Gilbert Strang. On the construction and comparison of difference schemes. SIAM Journal on Numerical Analysis, 5(3):506–517, 1968.

[71] Robert J. Kee, Michael E. Coltrin, and Peter Glarborg. Chemically Reacting Flow: Theory and Practice. Wiley, 2003. ISBN 9780471261797.

[72] Shivank Sharma, Ral Bielawski, Oliver Gibson, Shuzhi Zhang, Vansh Sharma, Andreas H. Rauch, Jagmohan Singh, Sebastian Abisleiman, Michael Ullman, Shivam Barwey, and Venkat Raman. An amrex-based compressible reacting flow solver for high-speed reacting flows relevant to hypersonic propulsion. arXiv preprint arXiv:2412.00900, 2024.

[73] M. Berger. Cut cells: Meshes and solvers. In Handbook of Numerical Analysis, volume 18, pages 1–22. Elsevier, 2017.

[74] Richard B. Pember, John B. Bell, Phillip Colella, William Y. Curtchfield, and Michael L. Welcome. An adaptive cartesian grid method for unsteady compressible flow in irregular regions. Journal of Computational Physics, 120(2):278–304, 1995. doi: 10.1006/jcph.1995.1165.

[75] Phillip Colella, Daniel T. Graves, Benjamin J. Keen, and David Modiano. A cartesian grid embedded boundary method for hyperbolic conservation laws. Journal of Computational Physics, 211(1):347–366, 2006. doi: 10.1016/j.jcp.2005.05.026.

[76] Marsha Berger and Andrew Giuliani. A state redistribution algorithm for finite volume schemes on cut cell meshes. Journal of Computational Physics, 428:109820, 2021. doi: 10.1016/j.jcp.2020.109820.

[77] Andrew Giuliani, Ann S. Almgren, John B. Bell, Marsha J. Berger, M. T. Henry de Frahan, and Deepak Rangarajan. A weighted state redistribution algorithm for embedded boundary grids. Journal of Computational Physics, 464:111305, 2022. doi: 10.1016/j.jcp.2022.111305.

[78] Ann S. Almgren. AMReX-Hydro. https://github.com/AMReX-Codes/AMReX-Hydro, 2022. GitHub repository.

[79] Bernard Larrouturou. How to preserve the mass fractions positivity when computing compressible multi-component flows. Journal of Computational Physics, 95(1):59–84, 1991. doi: 10.1016/0021-9991(91)90253-H.

[80] Pramod K. Subbareddy, Anand Kartha, and Graham V. Candler. Scalar conservation and boundedness in simulations of compressible flow. Journal of Computational Physics, 348:827–846, 2017. doi: 10.1016/j.jcp.2017.08.001.

[81] Shuzhi Zhang, Vansh Sharma, Shivank Sharma, Ral Bielawski, and Venkat Raman. Characteristic boundary condition for embedded-boundary method based compressible reacting flow solver. In AIAA Aviation Forum and ASCEND 2024, page 3863, 2024.

[82] Thiérry Poinsot. Boundary conditions for direct simulations of compressible viscous flows. Journal of Computational Physics, 101(1):104–129, 1992. doi: 10.1016/0021-9991(92)90046-2.

[83] Emmanuel Motheau, Ann S. Almgren, and John B. Bell. Navier–stokes characteristic boundary conditions using ghost cells. AIAA Journal, 55(10):3399–3408, 2017. doi: 10.2514/1.J055885.

[84] Chun Sang Yoo, Y. Wang, Arnaud Trouvé, and H. G. Im. Characteristic boundary conditions for direct simulations of turbulent counterflow flames. Combustion Theory and Modelling, 9(4):617–646, 2005. doi: 10.1080/13647830500307378.

[85] Chun Sang Yoo and Hong G. Im. Characteristic boundary conditions for simulations of compressible reacting flows with multi-dimensional, viscous and reaction effects. Combustion Theory and Modelling, 11(2):259–286, 2007. doi: 10.1080/13647830600898995.

[86] Abraham Cohen. An Elementary Treatise on Differential Equations. D. C. Heath & Company, 1906.

[87] Thiérry Poinsot and Denis Veynante. Theoretical and Numerical Combustion. French National Centre for Scientific Research, 2005. Available at https://hal.science/hal-00270731.

[88] Nicolas Odier, Marlène Sanjosé, Laurent Gicquel, Thierry Poinsot, Stéphane Moreau, and Florent Duchaine. A characteristic inlet boundary condition for compressible, turbulent, multispecies turbomachinery flows. Computers & Fluids, 178:41–55, 2019.

[89] Nicolas Guézennec and Thierry Poinsot. Acoustically nonreflecting and reflecting boundary conditions for vorticity injection in compressible solvers. AIAA Journal, 47(7):1709–1722, 2009.

[90] David H. Rudy and John C. Strikwerda. A nonreflecting outflow boundary condition for subsonic navier-stokes calculations. Journal of Computational Physics, 36(1):55–70, 1980. doi: 10.1016/0021-9991(80)90174-6.

[91] Lukas Berger, Antonio Attili, and Heinz Pitsch. Synergistic interactions of thermodiffusive instabilities and turbulence in lean hydrogen flames. Combustion and Flame, 244:112254, 2022.

[92] Norbert Peters. Laminar diffusion flamelet models in non-premixed turbulent combustion. Progress in Energy and Combustion Science, 10(3):319–339, 1984.

[93] J. M. Duclos, D. Veynante, and T. Poinsot. A comparison of flamelet models for premixed turbulent combustion. Combustion and Flame, 95(1–2):101–117, 1993.

[94] Denis Veynante and Luc Vervisch. Turbulent combustion modeling. Progress in Energy and Combustion Science, 28(3):193–266, 2002.

[95] E. Knudsen and H. Pitsch. A general flamelet transformation useful for distinguishing between premixed and non-premixed modes of combustion. Combustion and Flame, 156(3):678–696, 2009.

[96] H. Pitsch and N. Peters. A consistent flamelet formulation for non-premixed combustion considering differential diffusion effects. Combustion and Flame, 114(1–2):26–40, 1998.

[97] Heinz Pitsch. Unsteady flamelet modeling of differential diffusion in turbulent jet diffusion flames. Combustion and Flame, 123(3):358–374, 2000.

[98] R. W. Grout, A. Gruber, Chun Sang Yoo, and J. H. Chen. Direct numerical simulation of flame stabilization downstream of a transverse fuel jet in cross-flow. Proceedings of the Combustion Institute, 33(1):1629–1637, 2011.

[99] Vedanth Nair, Matthew Sirignano, Benjamin L. Emerson, and Timothy C. Lieuwen. Near-field evolution and scaling of shear layer instabilities in a reacting jet in crossflow. Journal of Fluid Mechanics, 960:A13, 2023.

[100] Mirko Gamba, Victor A. Miller, and M. Godfrey Mungal. The reacting transverse jet in supersonic crossflow: Physics and properties (invited). In 19th AIAA International Space Planes and Hypersonic Systems and Technologies Conference. American Institute of Aeronautics and Astronautics, 2014. doi: 10.2514/6.2014-3107.

[101] Yasin M. Abul-Huda and Mirko Gamba. Combustion effects of a staged transverse jet and pulsed detonation in supersonic crossflow. Proceedings of the Combustion Institute, 36(2):2681–2689, 2017. doi: 10.1016/j.proci.2016.08.041.

[102] Ashray Mohit, Jenna Stolzman, Margaret Wooldridge, and Jesse Capecelatro. Impact of turbulence on combustion performance in non-assist waste gas flares. Flow, Turbulence and Combustion, 116(6), 2026. doi: 10.1007/s10494-025-00714-y.

[103] Margaret S. Wooldridge, Jenna Stolzman, Ashray Mohit, and Jesse Capecelatro. So, you want to measure flare emissions? challenges and opportunities for quantifying utility pipe flare performance. Applications in Energy and Combustion Science, 25: 100448, 2026. doi: 10.1016/j.jaecs.2025.100448.

[104] Shivank Sharma, Jagmohan Singh, Lorenzo Angelilli, and Venkat Raman. Interaction of chemical reactions and turbulence in a jet in supersonic crossflow. Proceedings of the Combustion Institute, 40(1–4):105295, 2024.

[105] Vedanth Nair, Matthew Sirignano, Benjamin L. Emerson, and Timothy C. Lieuwen. Combustion and flame position impacts on shear layer dynamics in a reacting jet in cross-flow. Journal of Fluid Mechanics, 942:A41, 2022.

[106] Chao Han, David O. Lignell, Evatt R. Hawkes, Jacqueline H. Chen, and Haifeng Wang. Examination of the effect of differential molecular diffusion in dns of turbulent non-premixed flames. International Journal of Hydrogen Energy, 42(16):11879–11892, 2017.

[107] Wang Han, Arne Scholtissek, Felix Dietzsch, and Christian Hasse. Thermal and chemical effects of differential diffusion in turbulent non-premixed h2 flames. Proceedings of the Combustion Institute, 38(2):2627–2634, 2021.

[108] Hongchao Chu, Lukas Berger, Temistocle Grenga, Zhao Wu, and Heinz Pitsch. Effects of differential diffusion on hydrogen flame kernel development under engine conditions. Proceedings of the Combustion Institute, 39(2):2129–2138, 2023.

[109] Yuki Minamoto, Hemanth Kolla, Ray W. Grout, Andrea Gruber, and Jacqueline H. Chen. Effect of fuel composition and differential diffusion on flame stabilization in reacting syngas jets in turbulent cross-flow. Combustion and Flame, 162(10):3569–3579, 2015.

[110] Hao Tang, Chaobo Yang, Yedhu Krishna, Guoqing Wang, William L. Roberts, Thibault F. Guiberti, and Gaetano Magnotti. Differential diffusion effects in the near field of non-premixed nh3/h2/n2-air jet flames at elevated pressure. Experimental Thermal and Fluid Science, 149:111020, 2023.

[111] Robert W. Bilger, S. H. Stårner, and Robert J. Kee. On reduced mechanisms for methane-air combustion in nonpremixed flames. Combustion and Flame, 80(2):135–149, 1990.

[112] Malik Hassanaly, Heeseok Koo, Christopher F. Lietz, Shao Teng Chong, and Venkat Raman. A minimally-dissipative low-mach number solver for complex reacting flows in openfoam. Computers & Fluids, 162:11–25, 2018. doi: 10.1016/j.compfluid.2017.11.020.

[113] Vansh Sharma, Yihao Tang, and Venkat Raman. A computational study on effects of injector pitch angle on flame stabilization in opposed jets in crossflow. In 12th Mediterranean Combustion Symposium, Luxor, Egypt, page 12, 2023.

[114] J. Li, Z. Zhao, A. Kazakov, and F. L. Dryer. An updated comprehensive kinetic model of hydrogen combustion. International Journal of Chemical Kinetics, 36(10):566–575, 2004. doi: 10.1002/kin.20026.

[115] H. Pitsch. FlameMaster, A C++ Computer Program for 0D Combustion and 1D Laminar Flame Calculations, 2005. Available at https://www.itv.rwth-aachen.de/en/downloads/flamemaster/.

[116] B. Rogg. Response and flamelet structure of stretched premixed methane air flames. Combustion and Flame, 73(1):45–65, 1988.

[117] S. Menon, R. Zhao, J. Jayachandran, and F. N. Egolfopoulos. Evaluating flamelet configurations for simulating stretched laminar flames. In Spring Technical Meeting of the Western States Sections of the Combustion Institute, page 1, 2014. Paper 087LF-0017.

[118] E. Knudsen, H. Kolla, E. R. Hawkes, and H. Pitsch. Les of a premixed jet flame dns using a strained flamelet model. Combustion and Flame, 160(12):2911–2927, 2013.

[119] V. Giovangigli and M. Smooke. Extinction of strained premixed laminar flames with complex chemistry. Combustion Science and Technology, 53(1):23–49, 1987.

[120] D. G. Goodwin, R. L. Speth, H. K. Moffat, and B. W. Weber. Cantera: An object-oriented software toolkit for chemical kinetics, thermodynamics, and transport processes, 2021. Version 2.5.1, available at https://www.cantera.org.

[121] Y. Tang and V. Raman. Large eddy simulation of premixed turbulent combustion using a non-adiabatic, strain-sensitive flamelet approach. Combustion and Flame, 234:111655, 2021.

[122] W. Han, H. Wang, G. Kuenne, E. R. Hawkes, J. H. Chen, J. Janicka, and C. Hasse. Large eddy simulation/dynamic thickened flame modeling of a high karlovitz number turbulent premixed jet flame. Proceedings of the Combustion Institute, 37(2):2555–2563, 2019.

[123] David G. Goodwin, Raymond L. Speth, Harry K. Moffat, and Bryan W. Weber. Cantera: An object-oriented software toolkit for chemical kinetics, thermodynamics, and transport processes. Zenodo, 2018.

[124] J. Janicka and N. Peters. Prediction of turbulent jet diffusion flame lift-off using a pdf transport equation. Symposium (International) on Combustion, 19:367–374, 1982.

[125] Norbert Peters. Turbulent combustion. Measurement Science and Technology, 12(11): 2022–2022, 2001.

[126] Eduardo Javier Pérez-Sánchez, Emiliano Manuel Fortes, and Daniel Mira. Assessment of the flamelet generated manifold method with preferential diffusion modelling for the prediction of partially premixed hydrogen flames. Combustion and Flame, 2025. doi: 10.1016/j.combustflame.2025.114083.

[127] Ehsan Abtahizadeh, Laurentius P. H. de Goey, and Jeroen A. van Oijen. Differential diffusion effects inclusion with flamelet generated manifolds for the analysis of partially premixed flames. Proceedings of the Combustion Institute, 35(3):3463–3471, 2015. doi: 10.1016/j.proci.2014.05.148.

[128] Kazuhiro Kinuta, Reo Kai, Yuta Yada, and Ryoichi Kurose. Fgm modeling considering preferential diffusion, flame stretch, and non-adiabatic effects for hydrogen-air premixed flame wall flashback. Combustion and Flame, 267:113594, 2024. doi: 10.1016/j.combustflame.2024.113594.

[129] Gregory P. Smith, Y. Tao, and H. Wang. Foundational fuel chemistry model version 1.0 (ffcm-1). epub, 26:2018, 2016.

[130] Stephen B. Pope. Turbulent flows. Measurement Science and Technology, 12(11): 2020–2021, 2001.

[131] James F. Driscoll. Turbulent premixed combustion: Flamelet structure and its effect on turbulent burning velocities. Progress in Energy and Combustion Science, 34(1): 91–134, 2008.

[132] Yue Zhang, Wendi Dong, Laurien Vandewalle, Rui Xu, Gregory Smith, and Hai Wang. Foundational Fuel Chemistry Model Version 2.0 (FFCM-2). https://web.stanford.edu/group/haiwanglab/FFCM2, 2023. Website, accessed 2026-03-16.

[133] Yujie Tao and Hai Wang. Joint probability distribution of arrhenius parameters in reaction model optimization and uncertainty minimization. Proceedings of the Combustion Institute, 37(1):817–824, 2019. doi: 10.1016/j.proci.2018.08.052.

[134] Milton Van Dyke. Perturbation Methods in Fluid Mechanics. Parabolic Press, Stanford, CA, 1975.

[135] Venkat Raman and Malik Hassanaly. Emerging trends in numerical simulations of combustion systems. Proceedings of the Combustion Institute, 37(2):2073–2089, 2019.

[136] Michael E. Mueller, Gianluca Iaccarino, and Heinz Pitsch. Chemical kinetic uncertainty quantification for large eddy simulation of turbulent nonpremixed combustion. Proceedings of the Combustion Institute, 34(1):1299–1306, 2013.

[137] Weiqi Ji, Jiaxing Wang, Olivier Zahm, Youssef M. Marzouk, Bin Yang, Zhuyin Ren, and Chung K. Law. Shared low-dimensional subspaces for propagating kinetic uncertainty to multiple outputs. Combustion and Flame, 190:146–157, 2018.

[138] Nana Wang, Tianwei Yang, and Zhuyin Ren. Active subspace variation and modeling uncertainty in a supersonic flame simulation. AIAA Journal, 59(5):1798–1807, 2021.

[139] Feixue Cai, Hua Zhou, Min Yao, and Zhuyin Ren. Exploiting active subspace for modeling uncertainty and optimization in fan-shaped film cooling simulation. In Turbo Expo: Power for Land, Sea, and Air, volume 87998, page V007T12A037. American Society of Mechanical Engineers, 2024.

[140] Hai Wang and David A. Sheen. Combustion kinetic model uncertainty quantification, propagation and minimization. Progress in Energy and Combustion Science, 47:1–31, 2015.

[141] Kalen Braman, Todd A. Oliver, and Venkat Raman. Bayesian analysis of syngas chemistry models. Combustion Theory and Modelling, 17(5):858–887, 2013.

[142] Xiaoqing You, Trent Russi, Andrew Packard, and Michael Frenklach. Optimization of combustion kinetic models on a feasible set. Proceedings of the Combustion Institute, 33(1):509–516, 2011.

[143] Habib N. Najm, Bert J. Debusschere, Youssef M. Marzouk, Steve Widmer, and O. P. Le Maître. Uncertainty quantification in chemical systems. International Journal for Numerical Methods in Engineering, 80(6–7):789–814, 2009.

[144] Nicola E. Owen, Peter Challenor, Prathyush P. Menon, and Samir Bennani. Comparison of surrogate-based uncertainty quantification methods for computationally expensive simulators. SIAM/ASA Journal on Uncertainty Quantification, 5(1):403–435, 2017.

[145] Weiqi Ji, Zhuyin Ren, Youssef Marzouk, and Chung K. Law. Quantifying kinetic uncertainty in turbulent combustion simulations using active subspaces. Proceedings of the Combustion Institute, 37(2):2175–2182, 2019.

[146] Mona M. Dannert, Fynn Bensel, Amelie Fau, Rodolfo M. N. Fleury, and Udo Nackenhorst. Investigations on the restrictions of stochastic collocation methods for high dimensional and nonlinear engineering applications. Probabilistic Engineering Mechanics, 69:103299, 2022.

[147] Sandor Vajda, Peter Valko, and Tamas Turanyi. Principal component analysis of kinetic models. International Journal of Chemical Kinetics, 17(1):55–81, 1985.

[148] Perrine Pepiot-Desjardins and Heinz Pitsch. An efficient error-propagation-based reduction method for large chemical kinetic mechanisms. Combustion and Flame, 154 (1–2):67–81, 2008.

[149] Yuxuan Xin, David A. Sheen, Hai Wang, and Chung K. Law. Skeletal reaction model generation, uncertainty quantification and minimization: Combustion of butane. Combustion and Flame, 161(12):3031–3039, 2014.

[150] Alison S. Tomlin, Edirin Agbro, Václav Nevrlỳ, Jakub Dlabka, and Michal Vašinek. Evaluation of combustion mechanisms using global uncertainty and sensitivity analyses: A case study for low-temperature dimethyl ether oxidation. International Journal of Chemical Kinetics, 46(11):662–682, 2014.

[151] David A. Sheen and Hai Wang. The method of uncertainty quantification and minimization using polynomial chaos expansions. Combustion and Flame, 158(12):2358–2374, 2011.

[152] Xingyu Su, Weiqi Ji, and Zhuyin Ren. Uncertainty analysis in mechanism reduction via active subspace and transition state analyses. Combustion and Flame, 227:135–146, 2021.

[153] Ji-Hun Oh, Paxton Wiersema, Keunsoo Kim, Eric Mayhew, Jacob Temme, Chol-Bum Kweon, and Tonghun Lee. Fast uncertainty reduction of chemical kinetic models with complex spaces using hybrid response-surface networks. Combustion and Flame, 253: 112772, 2023.

[154] Zhuyin Ren and Stephen B. Pope. Species reconstruction using pre-image curves. Proceedings of the Combustion Institute, 30(1):1293–1300, 2005.

[155] Zhuyin Ren, Stephen B. Pope, Alexander Vladimirsky, and John M. Guckenheimer. The invariant constrained equilibrium edge preimage curve method for the dimension reduction of chemical kinetics. The Journal of Chemical Physics, 124(11), 2006.

[156] James C. Spall. Multivariate stochastic approximation using a simultaneous perturbation gradient approximation. IEEE Transactions on Automatic Control, 37(3):332–341, 1992.

[157] James C. Spall. An overview of the simultaneous perturbation method for efficient optimization. Johns Hopkins APL Technical Digest, 19(4):482–492, 1998.

[158] Shuzhi Zhang, Vansh Sharma, Venkat Raman, Tristan T. Shahin, Alexander J. Hodge, Rohan M. Gejji, Robert P. Lucht, and Carson D. Slabaugh. Three-dimensional analysis of hydrogen fuel effects in multi-tube combustor. Proceedings of the Combustion Institute, 41:105790, 2025.

[159] Alan Kéromnès, Wayne K. Metcalfe, Karl A. Heufer, Nicola Donohoe, Apurba K. Das, Chih-Jen Sung, Jürgen Herzler, Clemens Naumann, Peter Griebel, Olivier Mathieu, et al. An experimental and detailed chemical kinetic modeling study of hydrogen and syngas mixture oxidation at elevated pressures. Combustion and Flame, 160(6): 995–1011, 2013.

[160] Marcus Ó Conaire, Henry J. Curran, John M. Simmie, William J. Pitz, and Charles K. Westbrook. A comprehensive modeling study of hydrogen oxidation. International Journal of Chemical Kinetics, 36(11):603–622, 2004.

[161] Alan Keromnes, Nicola Donohoe, Henry Curran, Jürgen Herzler, Clemens Naumann, and Peter Griebel. Ignition delay time measurements and validation of reaction mechanism for hydrogen at gas turbine relevant conditions. In Proceedings, 2010.

[162] Kazuya Shimizu, Atsushi Hibi, Mituso Koshi, Youhi Morii, and Nobuyuki Tsuboi. Updated kinetic mechanism for high-pressure hydrogen combustion. Journal of Propulsion and Power, 27(2):383–395, 2011.

[163] Michael P. Burke, Marcos Chaos, Yiguang Ju, Frederick L. Dryer, and Stephen J. Klippenstein. Comprehensive h2/o2 kinetic model for high-pressure combustion. International Journal of Chemical Kinetics, 44(7):444–474, 2012.

[164] Juan Li, Zhenwei Zhao, Andrei Kazakov, and Frederick L. Dryer. An updated comprehensive kinetic model of hydrogen combustion. International Journal of Chemical Kinetics, 36(10):566–575, 2004.

[165] Shuzhi Zhang, Vansh Sharma, and Venkat Raman. High-fidelity numerical analyses for hydrogen jet-flames in crossflow. In Turbo Expo, volume 88797, page V03BT04A052. American Society of Mechanical Engineers, 2025.

[166] Shuzhi Zhang, Vansh Sharma, and Venkatramanan Raman. Differential diffusion effects on hydrogen-enriched jet flames in a crossflow. In AIAA SCITECH 2025 Forum, page 0154, 2025.

[167] Vedanth Nair, Matthew Sirignano, Benjamin L. Emerson, and Timothy C. Lieuwen. Combustion and flame position impacts on shear layer dynamics in a reacting jet in cross-flow. Journal of Fluid Mechanics, 942:A41, 2022.

[168] Marina Campolo, Maria Vittoria Salvetti, and Alfredo Soldati. Mechanisms for microparticle dispersion in a jet in crossflow. AIChE Journal, 51(1):28–43, 2005. doi: 10.1002/aic.10301.

[169] Mostafa Esmaeili, Asghar Afshari, and Farhad A. Jaberi. Turbulent mixing in non-isothermal jet in crossflow. International Journal of Heat and Mass Transfer, 89: 1239–1257, 2015. doi: 10.1016/j.ijheatmasstransfer.2015.05.055.

[170] Caleb Van Beck and Venkat Raman. Lagrangian-conditioned statistics of detonation propagation in a realistic rotating detonation engine. Proceedings of the Combustion Institute, 40(1–4):105606, 2024.

[171] Kevin H. Knuth. Optimal data-based binning for histograms, 2006. arXiv:physics/0605197.

[172] Astropy Collaboration. astropy.stats.knuth_bin_width: Return the optimal histogram bin width using knuth's rule. https://docs.astropy.org/en/stable/api/astropy.stats.knuth_bin_width.html, 2025. Accessed: 2026-03-13.

[173] Vansh Sharma, Shuzhi Zhang, Rahul Jain, and Venkat Raman. A mapping-based projection of detailed kinetics uncertainty onto reduced manifolds. Proceedings of the Combustion Institute, 2026. Draft/submitted version used in this dissertation draft.